Deployment Dynamics of Origami Sheets and Fluidic Origami Tubular Structures

by

Yutong Xia

A dissertation submitted in partial fulfillment
of the requirements for the degree of
Doctor of Philosophy
(Mechanical Engineering)
in the University of Michigan
2022

Doctoral Committee:

Professor Kon-Well Wang, Co-Chair
Assistant Professor Evgueni Filipov, Co-Chair
Professor Diann Brei
Professor Sridhar Kota

Yutong Xia

yutoxia@umich.edu

ORCID iD: 0000-0001-6747-5252

Acknowledgements

First and foremost, I would like to thank Professor Kon-Well Wang for the constant support, inspiration, and encouragement throughout the years. I must also extend my gratitude to Professor Evgueni Filipov for providing me the opportunity to explore the different ideas. I would like to thank my committee members, Professor Diann Brei and Professor Sridhar Kota for offering their insightful feedback that has improved this dissertation.

I would like to acknowledge the funding support from the Ford-University of Michigan Alliance Framework and the National Science Foundation (NSF) Grant CMMI #1634545. I am also grateful to Janice Tardiff and Chaitanya Nimmagadda from the Ford Motor Company, for many helpful discussions regarding this work.

Throughout my years at Michigan, I have had the fortune to work with a number of people who have profoundly influenced me. To start with, I learned a great deal from both current and past members of the Structural Dynamics and Controls Lab (SDCL) and the Deployable and Reconfigurable Structures Laboratory (DRSL). In particular, I would like to thank Dr. Narayanan Kidambi for his remarkable mentorship that helped me get through difficult times during my journey as a Ph.D. student.

Table of Contents

List of Tables

List of Figures

Abstract

In recent research investigations, Origami has shown great potential for creating reconfigurable structures for achieving various engineering functions. Especially, origami can be designed to fold compactly into very small volumes and then deploy to become large structures, which has led to many deployable system applications. Despite their promising potentials, most origami studies have focused on their static or kinematic features, while the complex and yet important dynamic behaviors of the origami deployment process have remained largely unexplored and unknown. To discover the missing knowledge, this thesis research investigates the dynamics of origami structure deployments, with a focus on Miura origami sheets, fluidic origami tubes, and fluidic multi-tube origami structures as testbeds. We construct a dynamic model for origami structures that captures the combined panel inertial and flexibility effects, which are otherwise ignored in rigid folding kinematic models but are critical in describing the dynamics of origami deployment. Our non-dimensionalized models provide rich new insights on how the deployment dynamic response is influenced by structural properties and other input parameters. This research advances the state of the art with new findings that have not and many times cannot be derived with traditional analyses.

Results from studying the Miura origami sheet show that the structure's deployment path may substantially deviate from a nominal quasi-static unfolding path based on the rigid folding assumptions, especially when the panels are more flexible. Additionally, it is shown that the pattern geometry influences the effective system stiffness, and therefore subtle changes in the

geometric parameters can result in qualitatively very different dynamic behaviors, where the Miura origami sheet may snap into different stable equilibria during the deployment process.

In the investigation of the fluidic origami tube, the ends of the tube are sealed and a space-invariant fluidic pressure field is first applied internally as a step function. The dynamic deployment results reveal that the internal pressure level can influence the structure's transient response and the final tube configuration. Additionally, results indicate that adjusting the fluidic pressure varies the effective stiffness and damping ratio of the system, and thus affects the tube's transient dynamic response during deployment. The multistability landscape of the fluidic tubular origami further enriches the deployment dynamics. By applying the fluidic pressure as a ramp function in time, we show that by controlling the pressurization rate, the tube can possess different transient behaviors and can settle at different stable configurations.

For the fluidic multi-tube origami structure testbed, we build models with different designs of the interface between tube elements. Results show that the multi-tube structure could have more complex behaviors than the single tube structure. The pressurization method and boundary conditions can influence the deployment significantly, where the structure can achieve a different deployment extent and arch in different directions. Furthermore, it is shown that with depending on the interface designs, multi-tube structures can reconfigure among different stable equilibria under dynamic deployment.

Chapter 1 Introduction

1.1 Introduction

Origami is an ancient paper folding art that can transform two-dimensional (2-D) sheets into complex 3-D structures. It has recently emerged as a promising tool for the design of mechanical structures with various functionalities. Because origami principles are scale independent, they have been adopted for the design of systems in a wide range of dimensions, from large space structures[1,2], mesoscale elements[3,4], to micro-scale devices[5-8]. Origami-inspired systems can provide extraordinary mechanical properties, such as auxeticity[10,11], nonlinear stiffness[3,12-21], multi-stability[15,22-31], and geometric reconfiguration[32-37]. By careful design of the origami, the system can also exhibit programmable mechanical properties[38-41]. Moreover, the ability of origami designs to be folded compactly into small volumes[9] and then deployed to large structures has led to a large number of deployable system applications. Because of the enormous interest, there have been immense studies on the kinematics and mechanism of origami structures[42-44], mostly focused on their static or quasi-static behaviors.

Apart from static/quasi-static applications, recent work has explored the suitability of origami designs for dynamics applications such as noise mitigation[45,46], acoustic metamaterials[47], energy absorption[48-52], impact mitigation[53-57], and vibration control[58-63]. Even origami-based structures nominally designed for static applications may be subject to dynamic loads from the environment. Therefore, it is crucial to understand the dynamic characteristics of origami to achieve desired system performance. In the context of deployable origami, the system dynamic characteristics may affect the accuracy, reliability, and efficiency of the deployment process. In

fact, the compliance and the inertia of the system may cause the dynamic deployment process to deviate from an unfolding path predicted by a purely geometric or kinematics treatment of the origami with static/quasi-static unfolding. Additionally, fluidic actuation sometimes used in tubular origami deployments can result in inflation, which cannot be predicted with traditional kinematics analyses.

From the above discussions, it is recognized that understanding the dynamic behavior of the deployment process of origami structures is critical for designing the systems and controlling their performance. In this research, we focus on three types of origami structures as testbeds, namely Miura origami sheets, fluidic origami tubes, and fluidic origami multi-tube structures, given that they are fundamental origami structural elements with many applications. More detailed reviews of these three classes of structures are in Sections 1.2, 1.3, and 1.4.

1.2 Background for Origami Sheet

Origami folding allows for easy fabrication of the deployable 3-D structures, because the process can start with flat sheets, which are often readily available. Thus, origami sheets may be considered as a fundamental building block for origami-based structures, even for advanced and complex 3-D geometries including curved surfaces[35,64-66]. Previous work has shown that origami sheets can be deformed to desired sophisticated shapes[67,68], and if the folding protocol is modified, they can also be refolded into new patterns[69]. Origami sheets are employed in various applications such as origami-based solar arrays[42,70], metamaterials[71-74], and shelters[2], with a focus on their static or kinematics features. Some recent research has explored the dynamic deployment of an origami flasher[75], and focused on the reaction forces inside the joints and panels. While useful and informative, this work is limited in that the deployment process is not fully studied. In this thesis research, we select a Miura origami sheet as our platform. The Miura

pattern[76] is a widely used origami pattern design[77] and can achieve rigid-foldability and flat-foldability, meaning that the origami structure can be folded to flat without panel deformation. Various actuation methods[78-83] have been proposed for the deployment of origami structures, such as pneumatic actuation, stored strain energy, and thermal activation with shape-memory materials. Since the focus of this thesis research is on the deployment dynamics rather than the actuation methods, we select only the strain energy method as the deployment actuation for the Miura origami sheet. We consider a basic deployment concept powered by the stored strain energy of folded creases and controlled with a prescribed rate at the free end.

1.3 Background for Fluidic Origami Tube

It has been recognized that tubular origami design offers promising ideas for inflatable deployable structures[84-89], due to their large internal volume change and expansion ratio when expanded from stowed states. Furthermore, origami tubes are shown to possess reprogrammable geometries, reconfigurable kinematics[90], and high stiffness to weight ratios when stacked together[91]. The recent exploration of fluidic origami tubes demonstrated their great multifunctional potential - pressurized by an internal fluidic field allows for various functionalities such as adaptable shape and stiffness[3], multistability[15], and programmable and recoverable energy absorption[16]. Utilizing fluidics is especially attractive given that they are readily available in many engineering systems and are easy to realize and control[92-94].

As for deployable origami, their system dynamic characteristics would greatly affect the accuracy, reliability, and efficiency of the deployment process. There have been efforts to address the actuation performance and deployment behaviors[79,83,95-97] of origami structures, however these previous works have focused primarily on their quasi-static or static properties. Recently, the dynamics of tubular origami deployment has gained people's attention, such as for

the Kresling origami[63,98] and Miura origami tubes[99], but only the strain energy stored in their originally folded shape is harnessed for deployment actuation, which is in general less reliable and less controllable than fluidic pressure control. On the other hand, while the inflatable fluidic tubular origami with internal pressurization has great potential to enable better deployable structures, their rich deployment dynamics have not been explored or understood.

1.4 Background for Origami Multi-Tube Structure

Building on the origami tubular element discussed in Section 1.3, the assemblage of multiple origami tubes has attracted interests because it allows for easy deployment while restricts motions in unintended modes[100], which can be desirable for some robotic and space boom applications that require very accurate and reliable deployment. In addition, comparing to single tube, they can possess enhanced mechanical properties, geometric versatility, and adaptivity[91]. It is shown that we can achieve programmable kinematics and tunable stiffness by changing the geometry of the cross section and folds[90] of the origami tubes, and the types of connections between tubes. While the static reconfiguration and properties of multi-tube origami structures has been investigated, their actuation performance and deployment dynamics remain unexplored. Moreover, the behavior of coupled origami tubes subjected to different pressures has not been examined in detail.

1.5 Research Goal and Problem Statement

From the above reviews and discussions, the goal of this research is to advance the state of the art and study the deployment dynamics of origami structures, with a focus on three testbeds: origami sheets, fluidic origami tubes, and fluidic origami multi-tube structures. The outcomes of this research will enable a deeper understanding of the physics behind origami

deployment and pave the way for new applications of origami-based deployable structures. In Chapters 2, 3, 4, and 5, we present our studies and results that provide us with insights and help us plan the path forward.

In Chapter 2, the mathematical dynamic models of the elements and systems of the three testbeds are discussed. In Chapter 3, we study the deployment of Miura origami sheets. We perform stiffness parametric study to explore how the panel compliance can influence the dynamic deployment behaviors. A geometric parametric study is performed to understand the influence of pattern geometries on structural properties as well as the multiple stable equilibria landscape of the structure. We also perform the deployment simulations with different control rates to gain more insights.

In Chapter 4, we study the deployment of Miura origami tubes under fluidic actuation. We first perform quasi-static analysis to understand the influence of the internal pressure field on structural properties. Stable equilibria analysis is performed to understand the multiple stable equilibria landscape of the structure with different folding stiffness under different pressure magnitudes. We perform dynamic simulations to gain insights on the snap-through behaviors of the structure under different pressurization magnitudes and rates.

In Chapter 5, we study the Miura origami multi-tube structures under fluidic actuation. We perform quasi-static and dynamic analysis to understand the structural properties and deployment behaviors. We perform a parametric study on the interface stiffness to understand its influence on the configuration and the deployment process. We also explore different interface designs and perform dynamic analysis on the deployment behaviors.

Building upon these efforts and findings, we propose possible future research directions as described in Chapter 6.

Chapter 2 Model Formulation

In this Chapter, we discuss how the origami structure models for sheets and tubes are developed for the purpose of analyzing deployment dynamics. Inertial properties of the structure are represented by a system of point masses that reflect the translational and principal rotational inertias of each parallelogram panel in the Miura origami structures. Rather than assuming rigid panels as is common in kinematic origami models, we adopt the bar and hinge approach to capture the panel flexibility[101-104] for both the Miura origami sheets and the tubes, which thereby allows us to capture dynamic behaviors associated with panel deformations, where bars capture in-plane stiffness while rotational springs capture out of plane stiffness related to panel bending and crease folding. Loading from the internal pressure field is represented by a nodal force system that reflect the first and second momentum of the pressure load on the panels.

2.1 Geometry

2.1.1 Miura Origami Sheet

The Miura origami sheet is formed by repeating a pattern of mountain and valley creases (Figure 1a). A single repeating unit of the Miura origami pattern (Figure 1a) is composed of four identical parallelogram panels. It is defined by three independent geometric parameters: two crease lengths (a, b), and the smaller interior angle, also known as the sector angle (γ). Under a rigid folding assumption, all the panels are fully rigid with no deformation during reconfiguration or folding. With this assumption, the Miura origami sheet possesses a single

degree of freedom (DOF). The 3-D folded configuration of the whole structure can then be determined by defining one of the dihedral angles inside the Miura origami unit (or sheet, or tube). In this study, the dihedral angle ρ (Figure 1c and Figure 1a) is used to describe the configuration of origami sheets and tubes under the rigid folding assumptions.

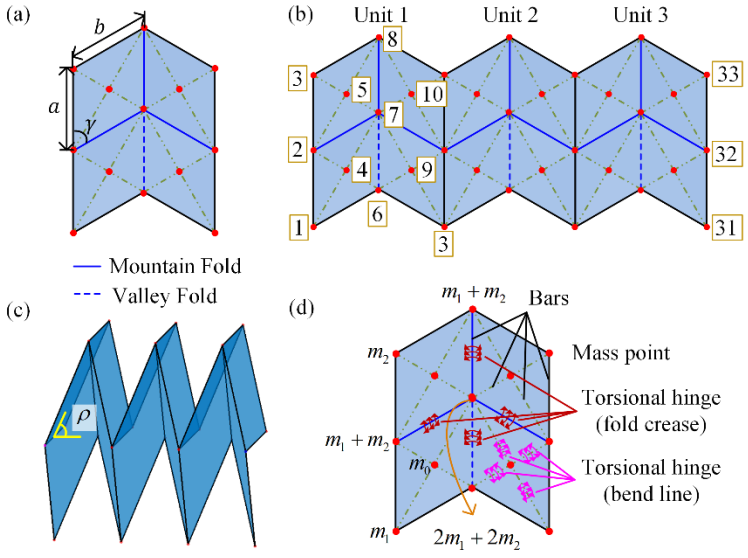

Figure 1. (a) A Miura origami unit, consisting of four panels connected with fold lines. The dashed line represents a valley fold while the solid lines represent mountain folds, or vice versa. (b) A Miura origami sheet consisting of three Miura origami units. Node numbering is denoted in the orange blocks. (c) The folded configuration of the Miura origami sheet, with the dihedral angle ρ in yellow. (d) The bar and hinge model representation for the Miura origami unit. The circular points represent nodes with nonzero mass, which are connected by massless bars (shown as lines). Torsional springs are placed at the rotational hinges, for both the fold creases (at both mountain and valley folds), and for the bend lines (within a panel).

2.1.2 Miura Origami Tube

To study the deployment dynamics of fluidic origami tube, we explore a 3-unit Miura origami tube, which is built by connecting two identical Miura origami sheets (Figure 2a) along their horizontal creases. The same as the sheet, the Miura origami tube has three independent geometric parameters $[a, b, \gamma]$ (Figure 2b) and possesses a single DOF under the rigid folding assumption, which is denoted by the dihedral angle ρ in Figure 2a.

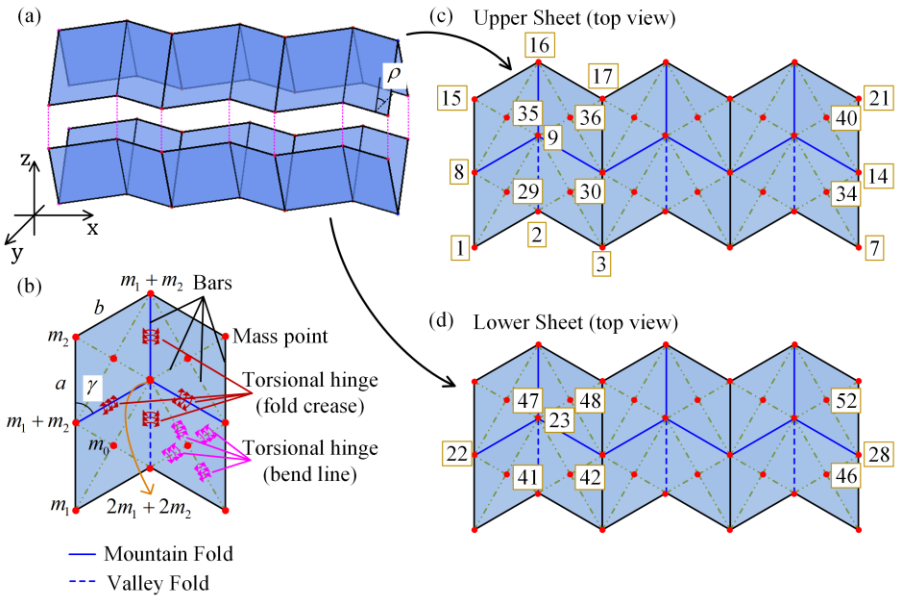

Figure 2. (a) A 3-unit Miura origami tube consists of two identical Miura origami sheets, the upper sheet (c) and the lower sheet (d). (c-d) Node numbering in the upper and lower sheets. (b) A bar and hinge representation of a Miura origami unit. The blue dashed and solid lines represent the valley and mountain folds respectively (or vice versa).

2.1.3 Miura Origami Multi-Tube Structure

To study the deployment dynamics of fluidic origami multi-tube structure, we explore an aligned-tube structure, which consists of two identical 3-unit Miura origami tubes. We adopt different interface designs as shown in Figure 3. The same as the single tube, the multi-tube structure has three independent geometric parameters $[a, b, \gamma]$ and possesses a single DOF under the rigid folding assumption, which is denoted by the dihedral angle ρ.

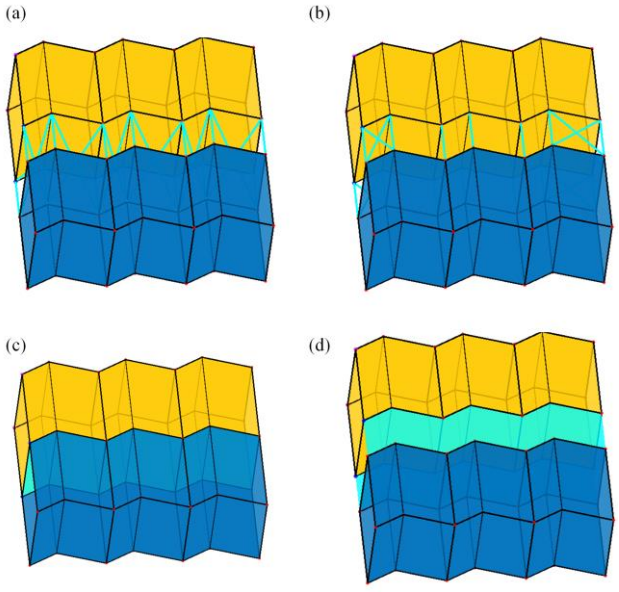

Figure 3. Different types of interface modeling for fluidic origami multi-tube structures, where the two tube elements are in blue and yellow, and the interface is in cyan. (a) Two tube elements are connected by elastic bars through corresponding vertices, which represent a solid material interface. (b) Two tube elements are connected by elastic bars, which allow rigid folding, representing a flexible interface. (c) Two tube elements are connected rigidly, which indicates there will be no displacement at the interface, representing an integrated manufactured multi-tube structure. (d) Two tube elements are connected through flexible facets, which is a variant of the three-element multi-tube structure. The interface can undergo bending and stretching deformation in each facet, and inter-facet folding deformation.

2.2 Stiffness

This Section and the following Section 2.3 apply to both the Miura origami sheet and the Miura origami tube. The stiffness of the structure is represented by a bar and hinge model, specifically the N5B8 representation where a node is placed in the middle of each panel. The bar and hinge model incorporates realistic material characteristics in its parameters, and reflects a reasonable approximation of scalable, isotropic, and realistic system behaviors, such as in-plane and out-of-plane deformations. For more details about the bar and hinge model, the reader is directed to REF[101-107]. The panel in-plane behavior is represented by bar elements with the stiffness of $k_s = EA/L$ where E is the Young's Modulus, L is the length of the bar and A is a representative cross section area of the bar as defined in Eq. 1. The values A_X, A_Y, A_D refer to the

cross-section areas of the bars located on the horizontal side, the vertical side, and the diagonal of the parallelogram respectively. The panel thickness is t, the lengths of the two sides of the parallelogram are H and W, and ν is the Poisson's ratio, the nominal values for which are in Table 1. Equation 1 shows that changing panel thickness and the shape of the parallelogram such as the sector angle and side lengths will affect the bar cross-section areas and the resulting stretching stiffness. The in-plane stiffness of the panels scales linearly with the thickness of the sheet and is orders of magnitude higher than the bending or folding stiffness of the sheet which scale near cubically with the thickness, while here we have found that it does not influence the dynamic behavior of the Miura sheet. Changing the in-plane stiffness results in negligible quantitative, and no noticeable qualitative influence on structural dynamic behaviors. Therefore, in the following parametric analyses of the Miura sheet system, the stretching stiffness is kept constant, while other variables are systematically varied.

$$A_X = t\,\frac{H^2 - \nu W^2}{2H(1-\nu^2)}$$

$$A_Y = t\,\frac{W^2 - \nu H^2}{2W(1-\nu^2)} \tag{1}$$

$$A_D = t\,\frac{\nu(H^2+W^2)^{3/2}}{2HW(1-\nu^2)}$$

As for the out-of-plane stiffness, Equation 2 shows the relationship between the bending angle θ and the reactive torque M_b representing panel bending. In the linear region of hinge deformation $\theta \in [10°, 350°]$, the stiffness per length is denoted by k_b.

$$M_b = \theta \cdot k_b = \theta \cdot \left(0.55 - 0.42\,\frac{2\gamma}{\pi}\right)\frac{Et^3}{12(1-\nu^2)}\left(\frac{D_S}{t}\right)^{1/3} \tag{2}$$

Equation 2 includes the sector angle γ, the length of short diagonal D_S, the thickness t of the panel. The material constants included are Young's modulus E and Poisson's ratio ν. The

panel bending stiffness is computed to be $k_b = 406\ [N]$ for a Miura panel with nominal material and geometric parameters as stated in Table 1. In our study, the panel bending stiffness k_b and the crease folding stiffness k_f will be varied to represent different types of folded origami structures, and to acquire insights into a wider range of origami dynamic behaviors. Here, we introduce a stiffness parameter $r_k \triangleq k_b/k_f$, which is the ratio between panel bending stiffness and crease folding stiffness. This ratio is kept higher than 5, which is generally true for most folded origami structures. We perform the stiffness parametric study by varying $[r_k, k_f]$ rather than $[k_b, k_f]$.

Table 1. Nominal material and geometric properties of the Miura sheet

Parameter	Nominal value
Young's modulus (E)	$7 \times 10^{10}\ [N/m^2]$
Poisson ratio (ν)	$0.33\ [-]$
Panel size (side length of the parallelogram)	$0.1 \times 0.1\ [m]$
Sector angle (γ)	$60°$
Panel thickness (t)	$0.001\ [m]$
Panel density (ρ)	$3000\ [kg/m^3]$

2.3 Inertia

To represent the inertia of the system in a manner compatible with the bar and hinge model, the parallelogram panels in the Miura origami are replaced by sets of lumped masses. The bars and hinges themselves are assumed to be massless. As a result, the Miura origami structure becomes a simplified finite-DOF structure, as shown in Figure 4a.

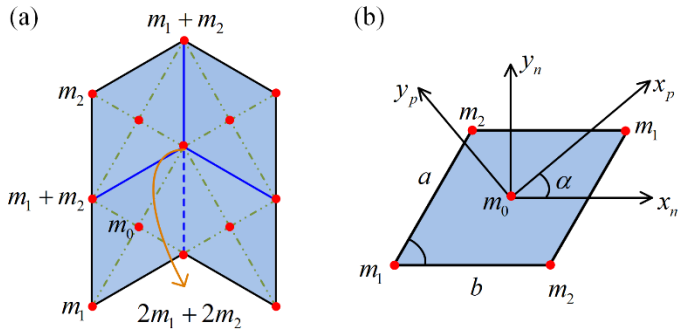

Figure 4. (a) The lumped mass system that represents the inertia of a Miura origami unit. Mass points are placed at the center and four corners of the parallelogram panels. (b) The lumped mass system for each panel, which is a quarter of the Miura origami unit. The vector x_n is the axis parallel to the side b of the parallelogram, and y_n is a vector perpendicular to x_n. The vectors x_p and y_p are the principal axes of this parallelogram. The angle between these two coordinate systems is α.

We arrange five mass points with prescribed values at the positions of the five nodes in the N5B8 model to represent the inertia of the panel, as in Figure 4b. The values of the mass points are denoted by m_0 for the center mass point and m_1 and m_2 for the mass points at the two different corners of the parallelogram. The mass points along each diagonal share same value. To capture the inertia properties of the panel, we compute the values of the mass points (m_0, m_1, m_2) that make the first and second moments of inertia of the discretized representation equivalent to those of the continuous panel, as Eq. 3. The value m_c is the mass of the whole panel, I_c is the inertia of the panel, and I_{mp} is the second moment of inertia of the mass point system.

$$m_0 + 2m_1 + 2m_2 = m_c$$
$$I_{mp} = I_c \tag{3}$$

The principal moments of inertia I_{x_p} and I_{y_p} of the homogeneous parallelogram panel are derived in Eq. 4. In Figure 4b, the coordinate system x_p and y_p are the principal axes of this continuum parallelogram. The angle α is between the principal axis x_p and the axis x_n which is parallel with side b of the parallelogram. The area of the parallelogram is defined as S.

$$I_{x_B} = \frac{m}{24}(a^2 + b^2 - \sqrt{(a^2 + b^2)^2 - 4S^2})$$

$$I_{y_B} = \frac{m}{24}(a^2 + b^2 + \sqrt{(a^2 + b^2)^2 - 4S^2}) \tag{4}$$

$$\cos(\alpha) = \sqrt{\frac{a^2 + b^2 + \sqrt{(a^2 + b^2)^2 - 4S^2} - 2a^2 \sin^2 \gamma}{2\sqrt{(a^2 + b^2)^2 - 4S^2}}}$$

Equation 5 calculates the second moment of inertia of the mass point system in the principal directions of the continuum parallelogram. The position of the i^{th} mass point with respect to the origin is defined as r_i, and is used to compute the rotational inertia of the node I_i.The inertia of the full mass point system is derived by summation of the rotational inertias of all the mass points.

$$I_i = m_i(|r_i|^2 - r_i r_i^T)$$

$$I_{mp} = I_0 + I_1 + I_2 + I_3 + I_4 \tag{5}$$

When the values of the mass points are defined as in Eq. 6, the first and second moments of inertia of the model match those of the parallelogram plate. Thus, the inertia of a panel can be represented by the set of independent mass points with these designated values.

$$m_0 = \frac{2}{3}m_c$$

$$m_1 = m_2 = \frac{1}{12}m_c \tag{6}$$

2.4 Non-Dimensional Equations of Motion

Having established the stiffness and inertia elements of the system, the equations of motion (EOMs) are derived for each DOF of all the nodes by Lagrange's equations (Eq. 7). In the bar and hinge model, if no constraints are imposed on the structure, then each node will have three degrees of freedom.

$$\frac{d}{dt}\left(\frac{\partial L}{\partial \dot{x}}\right) - \frac{\partial L}{\partial x} + \frac{\partial D}{\partial \dot{x}} = 0 \quad (7)$$

The Lagrangian is defined by $L(x, \dot{x}) = V(x) - T(x, \dot{x})$, where $V(x)$ is the strain energy of the system, and $T(x, \dot{x})$ is the kinetic energy. The nodal position is defined as x, and the nodal velocity is $\dot{x}$.

The total strain energy V consists of contributions from crease folding (V_{fold}), panel bending (V_{bend}), and panel stretching ($V_{stretch}$). The strain energy from crease folding V_{fold}, results from bending of torsional hinges at folding creases. The panel bending strain energy V_{bend}, is due to bending of the torsional hinges at bend lines in the model. Finally, the strain energy from stretching in the panels $V_{stretch}$, is due to elongation and compression of bars. Strain energy from crease folding or panel bending is computed as in Eq. 8, where θ_i can be the folding angle θ_f or the bending angle θ_b, and M is the reactive torque. The force generated on related nodes from the torque M is calculated by Eq. 9. Each dihedral angle θ_i is formed by its two adjacent triangular panels, containing a total of four nodes, therefore the partial derivative $\partial\theta_i/\partial x$ results in four vectors.

$$V_i = \sum_i \int_{\theta_0}^{\theta} M(\hat{\theta}_i) d\hat{\theta}_i \quad (i = fold, bend) \quad (8)$$

$$F_i = \frac{\partial V_i}{\partial x} = \sum_i \frac{\partial V_i}{\partial \theta_i}\frac{\partial \theta_i}{\partial x} = \sum_i M(\theta_i)\frac{\partial \theta_i}{\partial x} \quad (i = fold, bend) \quad (9)$$

In the strain energy from panel stretching $V_{stretch}$, the variable W is the strain energy density function as expressed in Eq. (11-12), in which E is the Green-Lagrange strain tensor, with material constants $\alpha_i,\ \mu_i,\ N$, and axial stretch λ_1. The corresponding nodal force F_s is derived by Eq. 13.

$$V_{stretch} = \sum_{s=bar} \int_0^{L_{bar}} W(E_s) A_{s\_bar} dx \tag{10}$$

$$W(E) = \sum_{i=1}^{N} \frac{\mu_i}{\alpha_i} (\lambda_1^{\alpha_i} - 1) \tag{11}$$

$$\lambda_1 = \sqrt{2E + 1} \tag{12}$$

$$F_s = \frac{\partial V_{stretch}}{\partial x} \tag{13}$$

Our dynamic model considers damping due to crease folding and panel elastic deformations, including the panel bending and stretching. The damping from crease folding and panel bending are represented by damping at hinges in the bar and hinge model with equivalent linear damping coefficient c_f (crease folding) and c_b (panel bending). The nodal force F_{di} of damping from crease folding or panel bending is derived in Eq. 14. The angular velocity $\dot{\theta}$ is a function of the dihedral angle in the hinge (θ) and the translational velocity $\dot{x}$: $\dot{\theta} = \frac{d}{dt}\theta(x) = \frac{d\theta}{dx}\frac{dx}{dt}$. The damping from panel stretching is represented by damping of bar deformation in the bar and hinge model with equivalent linear damping coefficient c_{vs}. The nodal force F_{ds} from panel stretching is as shown in Eq. 15, where l is the length of a bar, and $\dot{l}$ is the rate of length change of the bar.

$$F_{di} = c_i \dot{\theta} \frac{\partial \dot{\theta}}{\partial \dot{x}} \quad (i = fold, bend) \tag{14}$$

$$F_{ds} = c_{vs} \dot{l} \frac{\partial l}{\partial x} \tag{15}$$

The kinetic energy $T(x, \dot{x})$ is computed by a summation of kinetic energy of each individual node as in Eq. 16. The parameter m_i is the mass of the i-th node, and $\dot{x}_i$ is its nodal linear velocity.

$$T = \sum_i \frac{1}{2} m_i \dot{x}_i^2 \tag{16}$$

We perform non-dimensionalization to the EOMs. The general form of the EOM for a DOF u_i is shown in Eq. 17, in which u_i is the i-th non-dimensionalized nodal displacement. In this equation, the summation over $p = fold$ refers to all the fold creases that are related to this node; the summation over $q = bend$ refers to all bend lines at this node; the summation over $r = bar$ refers to all the bars that are connected to this node. The forces $\bar{F}_{f_p}$ and $\bar{F}_{b_q}$refer to the non-dimensional nodal forces at this node generated by the p-th folding crease and the q-th bending line respectively. The force $\bar{F}_{s_r}$ is the non-dimensional force from panel stretching represented by deformation of r-th bar. The non-dimensional nodal forces generated from the damping are $\bar{F}_{df_p}$, $\bar{F}_{db_q}$ and $\bar{F}_{ds_r}$, for the p-th folding crease, the q-th bending line, and the r-th bar respectively. Equation 18 shows a detailed expression.

As for the external load, in the sheet analysis, $\bar{F}_{ex} = 0$ because the deployment is fulfilled by the stored strain energy at the initially folded folding hinges from the structure itself.

In the deployment of Miura origami tube, the deployment is driven by the applied fluidic field inside the tube. Here we assume a space-invariant fluidic field and use nodal forces at the three vertices of each triangular element of a facet to represent the force from the internal fluidic field. When the three nodal forces all take on value as $\bar{P}_i \bar{S}_i/3$ with orientation perpendicular to the facet pointing to the outside of the tube, the first and second moments of the nodal forces match those of the pressure load. In the tube analysis, we keep fixed ratios $\bar{c}_f/\bar{k}_f$ and $\bar{c}_b/(\bar{r}_k \bar{k}_f)$ such that the damping ratios are constant for better observation of the deployment behaviors.

$$\bar{m}_i \ddot{u}_i + \sum_{p=fold} \left(\bar{F}_{f_p} + \bar{F}_{df_p}\right) + \sum_{q=bend} \left(\bar{F}_{b_q} + \bar{F}_{db_q}\right) \tag{17}$$

$$+\sum_{r=bar}\left(\bar{F}_{s_r}+\bar{F}_{ds_r}\right)=\bar{F}_{ex}$$

$$\bar{m}_i\ddot{u}_i+\bar{k}_f\bar{L}_f\sum_{p=fold}\left(\frac{\partial\theta_p}{\partial u_i}\left(\theta_p-\theta_{p0}\right)+\frac{\bar{c}_f}{\bar{k}_f}\frac{\partial\theta_p}{\partial u_i}2\zeta_0\dot{\theta}_p\right)$$

$$+\bar{r}_k\bar{k}_f\bar{L}_b\sum_{q=bend}\left(\frac{\partial\theta_q}{\partial u_i}\theta_q+\frac{\bar{c}_b}{\bar{r}_k\bar{k}_f}\frac{\partial\theta_q}{\partial u_i}2\zeta_0\dot{\theta}_q\right) \tag{18}$$

$$+\sum_{r=bar}\left(\frac{\bar{L}_r-\bar{L}_{r0}}{\bar{L}_r}\frac{\partial\bar{L}_r}{\partial u_i}+\bar{L}_r\frac{\partial\bar{L}_r}{\partial u_i}2\zeta_0\dot{\bar{L}}_r\right)=\bar{F}_{ex}$$

All the parameters and the variables are non-dimensionalized with the parameters found in Table 2. In this table, m_0 is the mass of the central node in the parallelogram panel. The mass-related variables (m_0, m_1, m_2) are non-dimensionalized by m_0. The crease length a depicted in Figure 1a and Figure 2a is used to non-dimensionalize the length-related variables (lengths of folding creases, bending lines, and bar elements). The variable τ is the non-dimensional time, and ω_0 is defined by $\omega_0=\sqrt{\frac{E\cdot A_D}{a\cdot m_0}}$, in which A_D is the cross-section area of the bar along the diagonal of the parallelogram as in Eq. 3. We introduce a stiffness parameter $\bar{r}_k$, which is the stiffness ratio between panel bending and crease folding. The damping coefficient of torsional springs are non-dimensionalized by the viscous damping coefficient c_{vs} of bar deformation. The damping ratio is defined by $\zeta_0=\frac{ac_{vs}}{2m_0\omega_0}$.

Table 2. Non-dimensionalization parameters.

Scales	ND parameters
Mass	$\bar{m}=m_i/m_0\ \ (i=0,1,2)$
Length	$\bar{L_i}=l_i/a\ \ (i=p,q,s)$
Time	$\tau=\omega_0 t$

Stiffness	$\bar{k}_i = k_i / EA_{bar} \ (i = f, b)$
	$\bar{r}_k = \bar{k}_b / \bar{k}_f$
Damping	$\bar{c}_i = c_i / a^2 c_{vs} \ (i = f, b)$

Chapter 3 Deployment Dynamics of Miura Origami Sheets

We utilized the models described in Chapter 2 to analyze the deployment dynamics of the origami structures. The investigation on the Miura origami sheet deployment is presented in Chapter 3, covering discussions of how the problem is set up (Section 3.1) and the effects of stiffness (Section 3.2), geometry (Section 3.3), and control rate (Section 3.4) on the deployment dynamics of the Origami sheet.

3.1 Deployment Setup

In the sheet analysis, the deployment occurs because there is strain energy stored in the initially folded stage, thus we fix the structure on one end, and then the free end can deploy automatically if set free. One common way to control deployable structures is to apply a pulling force or a displacement control on the free end[39]. In this study, we apply a time-dependent displacement control at the free end of the structure to mimic a common method where cables or cords are used to control the deployment of the structure. We set up three sets of different boundary constraints for the Miura origami sheet, one at the initial folded stage, the second for during the deployment process, and the third at the post-deployment stage. These constraints are applied at the relevant nodes, which are numbered according to Figure 1b.

At the initially folded stage, to ensure compact folding with internally stored energy, we fix all the vertices so that they will remain at prescribed positions. During deployment, to achieve smooth deployment and avoid additional panel deformation due to boundary constraints, we only fully constrain nodes 2 and 3 at the left end of the Miura origami sheet, denoted by the

pink squares in Figure 5. For the right end, we restrain node 32 in the y and z direction and control its position in the x direction. We perform a rate analysis in Section 3.4, in which we deploy the structure with different values of the rate. The default deployment control rate is 0.6 [-/sec] if not otherwise specified, e.g., in Section 3.2 and Section 3.3. Under these boundary constraints, the structure will be able to follow the kinematic path if panels are rigid. If we fixed all three nodes (node 1, 2, 3) on the left end, these nodes would form a V shape (colored in yellow in Figure 5) that remains fixed and prevents full deployment to a flat state. Deployment is controlled by prescribing the motion of the middle node on the right end (denoted with a green triangle) along a straight path, as shown by the green arrow in Figure 5. When the structure reaches its deployed stage, in which the sheet is fully flat, the displacement control will stop, and the controlled node will be fixed at the final position. In our analysis, the stress-free state is the flat configuration. Before deployment starts, the Miura origami sheet is folded into a compressed state with a fold angle of $\rho = 80°$. Once the Miura origami sheet is released, the deployment will occur by the releasing of the strain energy initially stored at the folded creases. The three different kinds of boundary constraints are shown in Table 3. Nodes which are not included in the table are only constrained before the deployment begins.

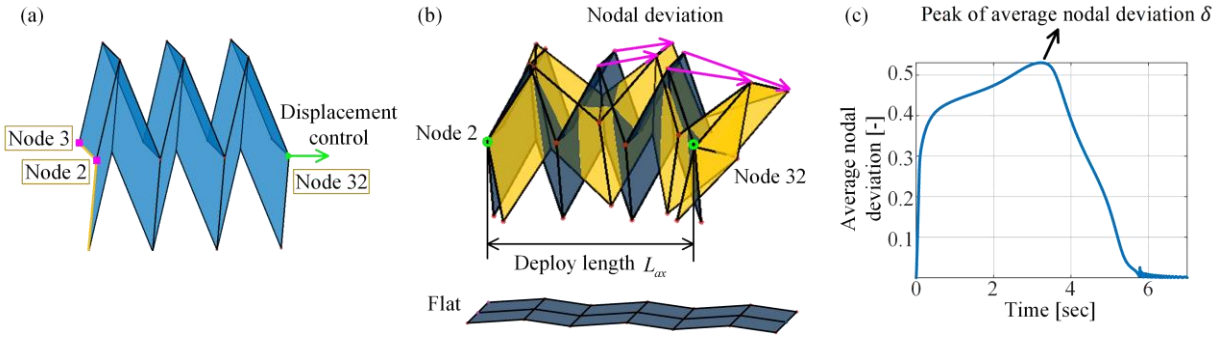

Figure 5. A Miura origami sheet at a mostly folded stage for illustration of boundary constraints. The nodes with pink squares are fixed in all three directions. The node with a green triangle is controlled during deployment and fixed after deployment. The arrow shows the path of displacement control.

Table 3. Boundary constraints before, during, and after the deployment process.

DOF / Stage	Node 2			Node 3			Node 32		
	x	y	z	x	y	z	x	y	z
Before deployment	All vertices fully fixed								
During deployment	fixed	fixed	fixed	fixed	fixed	fixed	controlled	fixed	fixed
After deployment	fixed	fixed	fixed	fixed	fixed	fixed	fixed	fixed	fixed

3.2 Influence of Stiffness Coefficients on Deployment Dynamics

In this Section, we investigate the role of the crease folding stiffness and the ratio between the panel bending stiffness and crease folding stiffness on the structural dynamic response. We perform numerical simulations on the non-dimensional model. The structure starts to deploy when the Miura origami sheet is released, and a displacement control with a constant velocity 0.6 [-/sec] is applied to the right end to guide the deployment process (Figure 5a). Unlike the single DOF rigid kinematic unfolding process, the panels undergo bending and stretching deformations, and the entire Miura origami sheet shows transient oscillation during the deployment.

In Figure 6, we use yellow color to represent the dynamic deployment configuration of the sheet, while blue color refers to the corresponding rigid unfolding configuration at the same stage of deployment. The deployment stage is defined using the distance between the fixed node 2 and the controlled node 32 in the x direction, denoted by L_{ax} in Figure 5b. We represent the

deployment stage using a percentage of the length of the current configuration, L_{ax}, with respect to that of the fully deployed flat configuration (Figure 5b). To quantitatively evaluate the dynamic behaviors of the Miura origami sheet, we compare the dynamic configuration with the corresponding kinematic configuration at the same deployment stage, and compute the deviation for each of the nodes (four sample node deviations are shown with pink arrows in Figure 5b). The average of the magnitude of the deviation among all the nodes is used to evaluate the difference between the dynamic deployment configuration and the rigid kinematic unfolding configuration, which is presented as a function of time in Figure 5c. To characterize the performance of the deployment process, we employ the peak value of the averaged nodal deviation δ that occurs during the deployment time history (e.g., 3.8 sec in Figure 5c) as an index for comparison.

From the normalized stiffness terms in Eq. (20), we vary the effective stiffness by changing the stiffness variables $\left(\bar{r}_k, \bar{k}_f\right)$, where the structure may exhibit qualitatively very different deployment behaviors. The deployment processes of three structures with different stiffness ratios $\bar{r}_k$ are shown with snapshots in Figure 6. In cases where the panel stiffness is similar in magnitude to the fold stiffness, the structure undergoes a large global bending and snaps into a 'pop-up' configuration. This pop-up occurs at different stages depending on the stiffness ratio. In Figure 6, the structure with $\bar{r}_k = 5$ undergoes pop-up earlier during deployment than structure with $\bar{r}_k = 7$. However, as the stiffness ratio $\bar{r}_k$ increases, the dynamic deployment starts to follow closer to the rigid kinematic unfolding, and as with $\bar{r}_k = 10$ and higher, the pop-up does not occur throughout the deployment process. Experimentally, we observe similar behaviors through studying a proof-of-concept prototype as shown in Figure 7. The facets are built by two layers of paper, and are connected by a thin 0.5 [mm] plastic sheet in the middle

(Figure 7i). The dimensions are the same as listed in Table 1. The deployment is guided by stored strain energy and a displacement control on the right end denoted by the white arrow. The structure can stabilize at configurations similar to those captured in the snapshots of the dynamic process from the analysis, indicating that the different dynamic configurations are the results of the different stable equilibria of the structure at different deployment stages. In Figure 6, the model exhibits the squeezed configuration (Figure 6a), a pop-up configuration (Figure 6b,c,f), a less distorted shape at a more deployed stage (Figure 6d,g,h), and the stress-free flat state (Figure 6e).

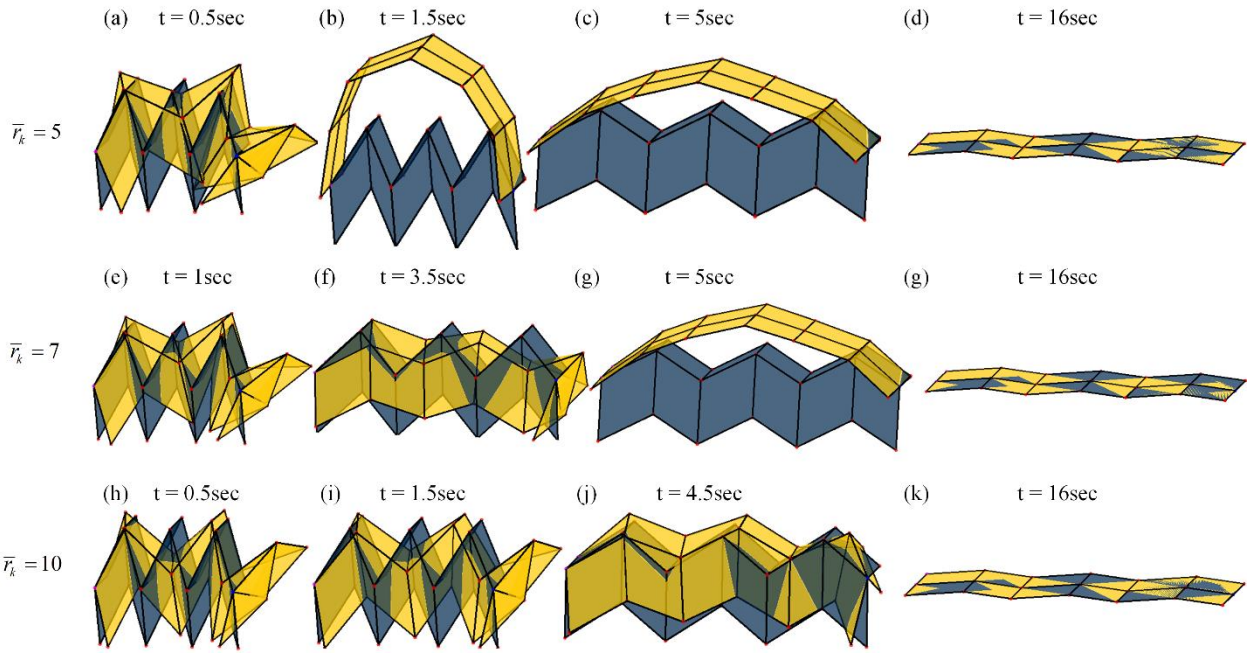

Figure 6. Snapshots of the deployment process of the 3-unit Miura origami sheet structure with different stiffness ratios: (a-d) $\bar{r}_k = 5$*; (e-g)* $\bar{r}_k = 7$ *; and (h-k)* $\bar{r}_k = 10$*. The fold stiffness is the same for all cases with* $\bar{k}_f = 3.8 \times 10^{-7}$ *(*$\bar{k}_f / \bar{k}_{f0} = 1$*).*

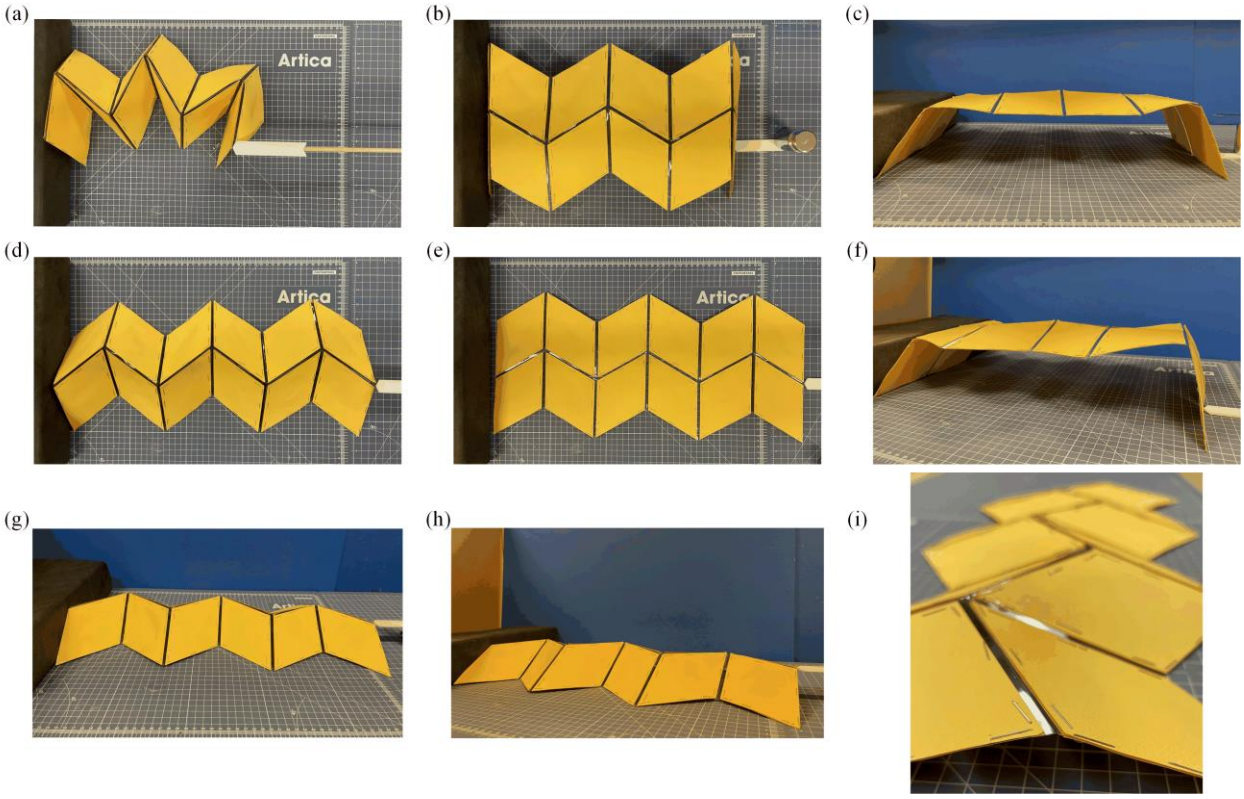

Figure 7. Experimental investigation: snapshots of the configurations at different deployment stages of a 3-unit Miura origami sheet prototype. The upper crease on the left end is fixed, and the central vertex on the right end is controlled, denoted by the white arrow. (a) refers to a folded state, (b) refers to a pop-up state, with (c) and (f) showing a front view and side view of the pop-up state, respectively. (d) refers to a more deployed state with (g) and (h) showing a front view and side view. (e) refers to the flat configuration. (i) shows a detailed view of the crease.

The global pop-up motion in the snapshots (Figure 6) result in large nodal deviations and are dependent of stiffness. We perform a parametric study on the stiffness coefficients $\left(\bar{r}_k, \bar{k}_f\right)$ and compute the corresponding δ for each of the deployment processes (Figure 8). We use a normalization value $\bar{k}_{f0} = 3.8\times10^{-7}$ to allow for simpler representation of the folding stiffness. The structures with higher $\bar{k}_f$, meaning stiffer fold lines, results in slightly higher δ than those with lower fold stiffness but the same ratio $\bar{r}_k$. Because the deployment is facilitated by strain energy stored in the fold creases, systems with higher $\bar{k}_f$ have more energy stored initially, which results in more reactions among units during the dynamic motion and more panel

deformation, and thus higher overall deviation. The stiffness ratio $\bar{r}_k$ has more significant effects on the structural dynamic behaviors. As the ratio $\bar{r}_k$ increases, meaning that the panels become stiffer relative to the folds, there is less panel bending, and the deviation δ decreases to zero where the structure follows the nominal rigid unfolding path. Three sharp declines are observed in the averaged nodal deviation peak, the first between $\bar{r}_k = 7$ and $\bar{r}_k = 8$, the second between $\bar{r}_k = 9$ and $\bar{r}_k = 10$, and the last between $\bar{r}_k = 78$ and $\bar{r}_k = 100$, depending on the fold stiffness $\bar{k}_f$. These three drops happen due to distinct changes in the structural behaviors. Before the first drop of δ in Figure 8, the stiffness of the panels is similar to the stiffness of the folds. The corresponding structure snaps into the "pop-up" state as soon as it is released from the initial boundary constraints (Figure 6(a-d)) which results in the highest nodal deviations. As the panel to fold stiffness ratio increases to $\bar{r}_k = 7$, there is a drop in the deviation, because the structure only pops up later during the deployment process (see difference between Figure 6(b) and Figure 6(f)). This later occurrence of the pop-up deformation results in a relatively smaller δ than if the pop-up occurs at the beginning of the deployment process. The second drop in deviation in Figure 8 occurs when the panels are further stiffened with a ratio of $\bar{r}_k = 10$. In this case, despite some modest deviations, the system remains close to the rigid kinematic unfolding configuration, and no pop-up occurs throughout the deployment process. As the panel to fold stiffness ratio increases beyond $\bar{r}_k = 10$, the origami sheet will not pop up, indicating the existence of a critical value for the stiffness coefficient $\bar{r}_k$, beyond which large global deviations can be avoided. We define the minimum stiffness ratio that keeps the structure from pop-up as $\bar{r}_{km}$. In Section 3.3.2, we will discuss that this critical value $\bar{r}_{km}$ also depends on the number of units in the Miura origami sheet. The nodal deviations undergo the third drop around $\bar{r}_k = 78$ with $\bar{k}_f / \bar{k}_{f0} = 1$, and at

successively higher ratios for structures with stiffer folds (up to $\bar{r}_k = 100$ for structures with $\bar{k}_f / \bar{k}_{f0} = 50$). We select the curve with $\bar{k}_f / \bar{k}_{f0} = 1$ for illustration and compare the case $\bar{r}_k = 78$ with $\bar{r}_k = 80$, as shown in Figure 9. When released, the softer structure ($\bar{r}_k = 78$) snaps into a configuration with uneven deviations among the different units, where the rightmost unit is more compressed, while the left and middle units are more deployed than the rigid unfolding configuration (Figure 9a). Later in the deployment process the structure snaps back to a more uniform configuration that closely follows the rigid configuration, as shown in Figure 9c. As for the stiffer case ($\bar{r}_k = 80$), the structure always stays at near the rigid unfolding configuration throughout deployment, and the deviations are thus much smaller.

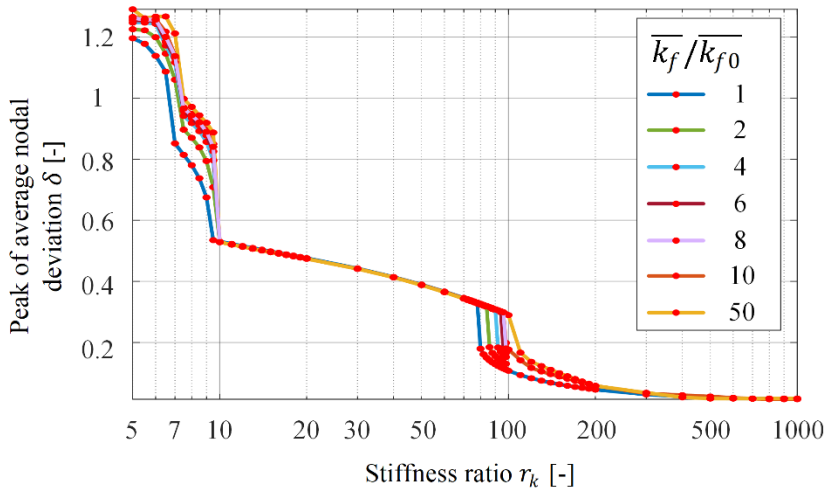

Figure 8. A parametric study of the stiffness coefficients for a 3-unit Miura origami sheet. We vary the stiffness ratio $\bar{r}_k \in [5,1000]$, where 5 refers to a system where panels and folds have a similar stiffness (e.g., a paper prototype), and 1000 refers to a system where the panels are much stiffer (e.g., metal panels connected with hinges). The x-axis is the stiffness ratio $\bar{r}_k$ in log scale, and the y-axis is the peak value of the averaged nodal deviations δ on a linear scale. The curves in different colours indicate different fold stiffness $\bar{k}_f$. We vary the $\bar{k}_f$ with respect to $\bar{k}_{f0} = 3.8 \times 10^{-7}$, and present a normalized ratio. In the regions $\bar{r}_k \in [10, 70]$ and $\bar{r}_k > 200$, the difference between results is small, and the curves overlap each other.

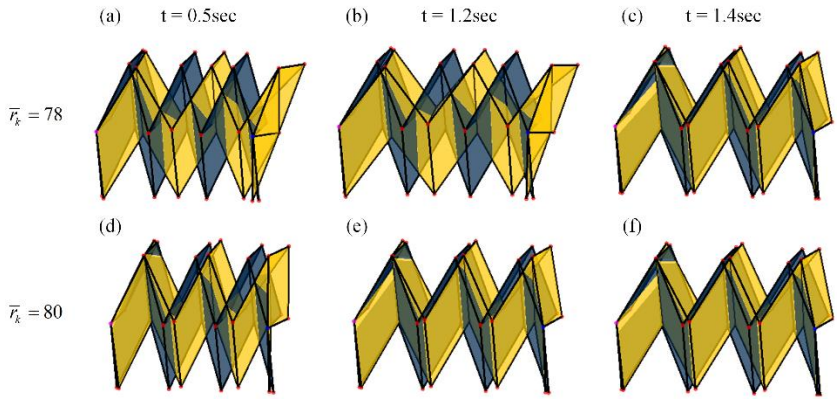

Figure 9. Snapshots of the deployment process of structures with (a-c) $\bar{r}_k = 78$*; and (d-f)* $\bar{r}_k = 80$*. Both structures have* $\bar{k}_f / \bar{k}_{f0} = 1$*. These two deployment processes correspond to directly before (a-c) and after (d-f) the third drop in the* $\bar{k}_f / \bar{k}_{f0} = 1$ *curve in Figure 8. The two systems have different extents of deviation from the rigid path.*

This study shows that the structure can exhibit significantly different behaviors as a function of stiffness. The fold stiffness $\bar{k}_f$ directly affects the initially stored strain energy, and a higher fold stiffness can slightly increase the deviation between systems with the same ratio $\bar{r}_k$. The ratio $\bar{r}_k$ plays a more important role than the absolute value of the fold stiffness. Low $\bar{r}_k$ values result in large panel deformations and possibly a global pop-up type motion. When the ratio $\bar{r}_k$ is increased beyond a critical value $\bar{r}_{km}$ the pop-up behavior is inhibited, and the structure eventually follows the rigid kinematic unfolding configuration.

3.3 Influence of Geometry on the Deployment Dynamics

According to Section 3.2, the structural dynamic deployment behaviors can be greatly influenced by changing the material stiffness coefficients, especially the stiffness ratio $\bar{r}_k$. Large $\bar{r}_k$ represents stiffer panels compared to the fold lines, and thus less deformation and deviation occurs during the deployment when compared to the rigid unfolding case. In this Chapter, we

will show that, other than the material stiffness coefficients, the number of units and geometry of the origami can also change the effective stiffness of the structure (Sections 3.3.1 and 3.3.2), and thus will affect the dynamic deployment process (Sections 3.3.3 and 3.3.4).

3.3.1 Influence of Geometry on Structural Stiffness Properties

The EOM in Eq. (20) reveals that the nodal force can be affected by the crease length L and partial derivative $\partial\theta/\partial u$, which implicitly contain other geometric parameters and thereby affect the overall stiffness of the crease. Here, we first examine one unit to show how the effective stiffness ratio between a fold line and bend line (Figure 10a), defined as $\bar{r}_{eff} = \bar{L}_p \frac{\partial \theta_p}{\partial u_i} \Big/ \bar{L}_q \frac{\partial \theta_q}{\partial u_j}$, is affected by the geometric parameters. The contour plot in Figure 10b shows the effective stiffness ratio with respect to the crease length ratio and the sector angle. The crease length ratio is the ratio between the length of the horizontal folds versus the length of the vertical folds: $\bar{b} = b/a$ (Figure 10a). A unit with a low sector angle of $30°$ and a high crease length ratio of 2 (Figure 10f) has an effective stiffness ratio that is about 5 times higher than that of the unit with a sector angle of $80°$ and a crease length ratio of 0.5 (Figure 10c). These large differences in the effective stiffness ratio indicate that the geometric parameters can have a significant effect on the global stiffness properties, and thus may influence the deployment dynamics.

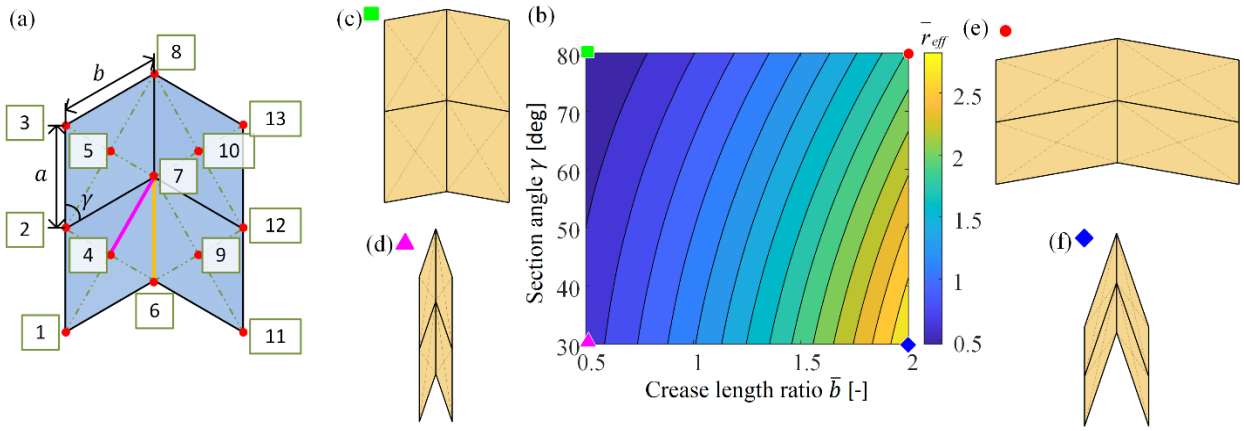

Figure 10. (a) A unit of the Miura with the fold line (yellow) that is related to the movement of nodes 6-7-4-9, and the bend line (pink) related to nodes 4-7-2-6. (b) Contour plot of the effective stiffness ratio $\bar{r}_k$, which is shown in the z-direction with colored shading. The parameter space is spanned by the crease length ratio $\bar{b}$ in the x-axis and the sector angle γ in the y-axis. (c, d, e, f) show the extreme cases of geometric parameters at the four corners of the contour plot.

As the origami sheet deploys, its overall geometric shape changes with the folding angle, which will affect the effective stiffness of the system. This shape change occurs even though the base geometric parameters γ and $\bar{b}$ are kept constant. Because the mass of the structure remains proportional to the size of the structure, the modal natural frequencies derived from an eigen-analysis can provide a direct representation of the effective structural stiffness. Here, we perform an eigen-analysis on the static equilibrium state of the system at different points along the deployment path. We apply the same boundary constraints as in the dynamic analysis except that we fix node 32 at each stage along the deployment path. The static equilibrium state is obtained by allowing the nodal position of the origami to converge to a new configuration through an iterative process of the static governing equations (delete the time varying variables and inertial and damping terms from the dynamic EOM) which minimizes the sum of internal forces within the system. An eigen-analysis using the mass and stiffness matrices of the structure is then performed to find the natural frequencies and the corresponding fundamental modes. Figure 11 shows results from this analysis for different points along the deployment path of the origami.

This 3-unit sheet has a crease length ratio at $\bar{b}=1$, sector angle at $\gamma=60°$, and stiffness parameters ($\bar{r}_k=100$, $\bar{k}_f/\bar{k}_{f0}=1$). The natural frequencies of the structure increase with deployment, and reach a peak value followed by a sharp decline near the fully deployed stage (Figure 11g). At a low deployment extent of 5%, the first two eigenmodes refer to deployment mainly in the longitudinal direction (Figure 11(b, c)), while the third eigenmode refers to a near pop-up transverse or bending configuration (Figure 11a). As the deployment increases to 20%, the second (Figure 11e) and third (Figure 11c) eigenmodes switch in order. As the structure becomes more deployed, the eigenmodes become significantly different (Figure 11(h-j)). A sharp reduction in the natural frequencies is observed around the deployment extent of 100%. By comparing the shape of the eigenmodes at 99% and 100% we see that the behavior changes drastically, and the origami sheet at a flat state has modes that resemble the transverse bending modes of an elastic beam (Figure 11(l-m)). In these modes, the deformation concentrates at the creases, which results in less energy and a lower natural frequency.

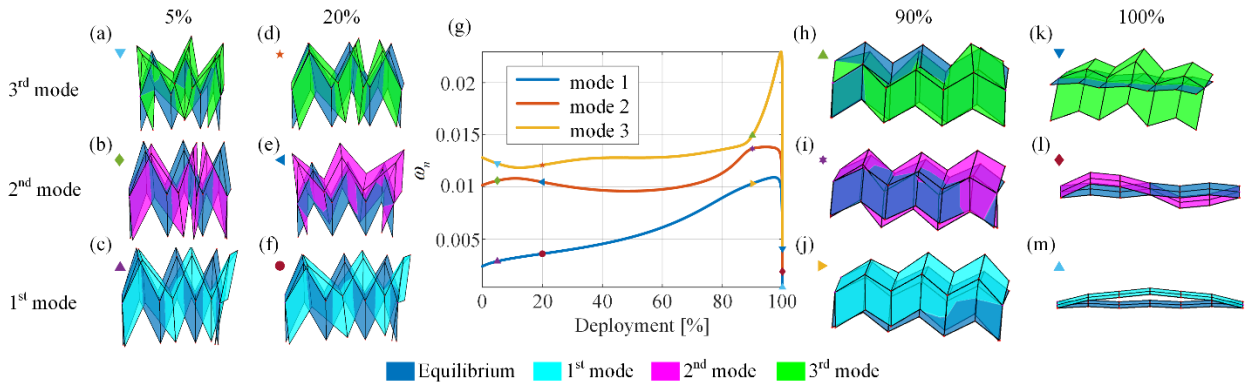

Figure 11. The first three natural eigenmodes of the sheet. (g) The natural frequencies as a function of the deployment stage. In the snapshots, the dark blue configurations refer to the quasi-static equilibrium position, and the remaining colors (cyan, magenta, and green) refer to the shape of the first three eigenmodes. Each row corresponds to a certain mode, while each column corresponds to a certain extent of deployment.

To obtain a more comprehensive understanding, these eigenvalue analyses are performed for the sheet with different geometric parameters and with different numbers of units. Figure 12

shows contour plots of the first mode natural frequency ω_n for structures with different parameters (crease length ratio $\bar{b}$, sector angle γ, and number of units) presented in the horizontal axis and the deployment stage in the vertical axis. Structures with higher $\bar{b}$ appear softer (lower natural frequency) given the same stage of deployment Figure 12a). From Figure 12b, we see that the maximum natural frequency (and stiffness) occurs for structures with a sector angle γ of around $65°$. For low deployment stages, structures with $\gamma < 57°$, have a discontinuity in the natural frequency values which is due to the stable quasi-static state entering another equilibrium state as will be discussed in 4.3.3. In Figure 12c, we perform the eigenvalue analysis on sheets with different numbers of units and show that the Miura origami sheets consisting of more units tend to be softer (lower natural frequency) because more creases and panels in the structure allow for more global deformation. Note that with more units, the internal mass and stiffness of the structure both increase proportionally, but the overall effective stiffness decreases. The apparent discontinuities in Figure 12c occur because the contour lines have fixed values, and there is sparse data in the horizontal direction corresponding to discrete values for the number of units. With all different parameter variations, as the structures become more deployed (i.e., around 80-99%), they exhibit a higher natural frequency and effective stiffness similar to the results observed in Figure 11g.

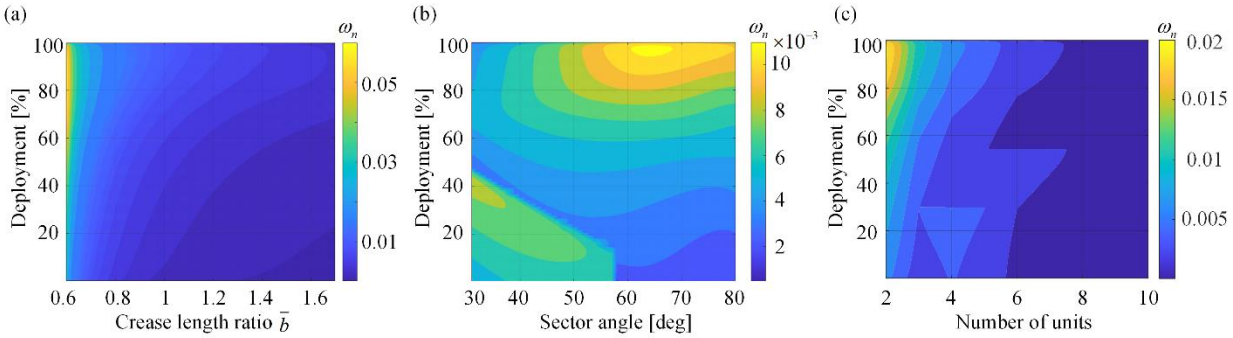

Figure 12. The first mode natural frequency ω_n of the Miura sheet structure with different geometric parameters. The geometric parameter is varied with the x axis and the deployment stage with the y axis. (a) Different crease length ratios $\bar{b}$, where the sector angle is kept at $\gamma = 60°$, and there are 3 units in the sheet. (b) Different sector angles, where the crease length ratio is kept at $\bar{b} = 1$, and there are 3 units in the sheet. (c) A different number of units in the sheet, while the crease length ratio is kept at $\bar{b} = 1$, and the sector angle is kept at $\gamma = 60°$. (Note: a continuous contour is presented, but only discrete values of the number of units are used in c).

3.3.2 Influence of Number of Units on the Dynamic Deployment Process

The eigen analysis in Section 3.3.1 showed that origami sheets consisting of more units have a lower natural frequency and lower effective stiffness (Figure 12c). In this Section, we investigate the dynamic deployment behavior of origami sheets with different numbers of units. Figure 13 shows that the nodal deviation δ increases with the number of units, indicating that the longer and more flexible structures experience more deformation as can be expected.

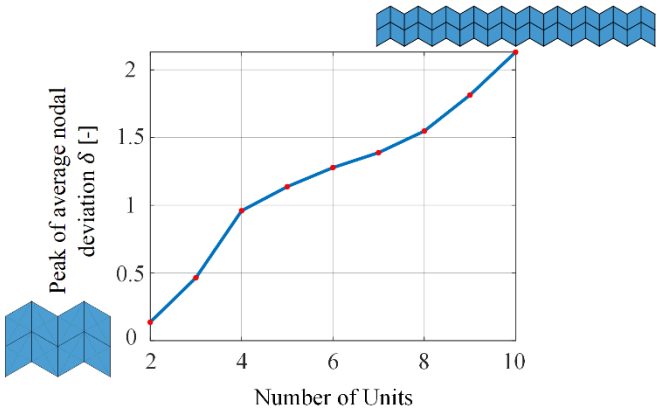

Figure 13. Nodal deviation δ increases with the number of units in the origami sheet. The Miura sheet has the geometry of ($\bar{b}=1$, $\gamma=60°$), and stiffness parameters of ($\bar{r}_k=100$, $\bar{k}_f/\bar{k}_{f0}=1$). With these stiffness parameters, the structures do not experience the pop-up deformation observed earlier in Chapter 3.

The value of the critical stiffness ratio $\bar{r}_{km}$ at which the structure will no longer experience a pop-up deformation (Figure 6(b, c, g)) also varies with the number of units in the structure. We vary the number of units and perform dynamic analyses on structure with different stiffness parameters ($\bar{r}_k$, $\bar{k}_f/\bar{k}_{f0}$), and show the relationship between the nodal deviation δ and stiffness parameters ($\bar{r}_k$, $\bar{k}_f/\bar{k}_{f0}$) for systems with 5, 7 and 10 units (Figure 14(a-c)). As discussed in Chapter 3, the ratio γ plays a more significant role than the fold stiffness in affecting the qualitative deployment behavior. For stiffness ratios lower than $\bar{r}_{km}$, the structure undergoes a pop-up and results in high nodal deviation, while for higher stiffness ratios, the pop-up is avoided, and the structure follows the rigid kinematic configuration more closely. The analyses on structures with 5, 7, and 10 units show the same qualitative behaviors (Figure 14(a-c)). Moreover, the critical ratio $\bar{r}_{km}$ increases as we increase the number of units, and a higher stiffness ratio $\bar{r}_k$ is needed to avoid pop-up in the longer and more flexible structures (Figure 14d). In other words, stiffer panels are needed to avoid the pop-up deformation for longer sheets.

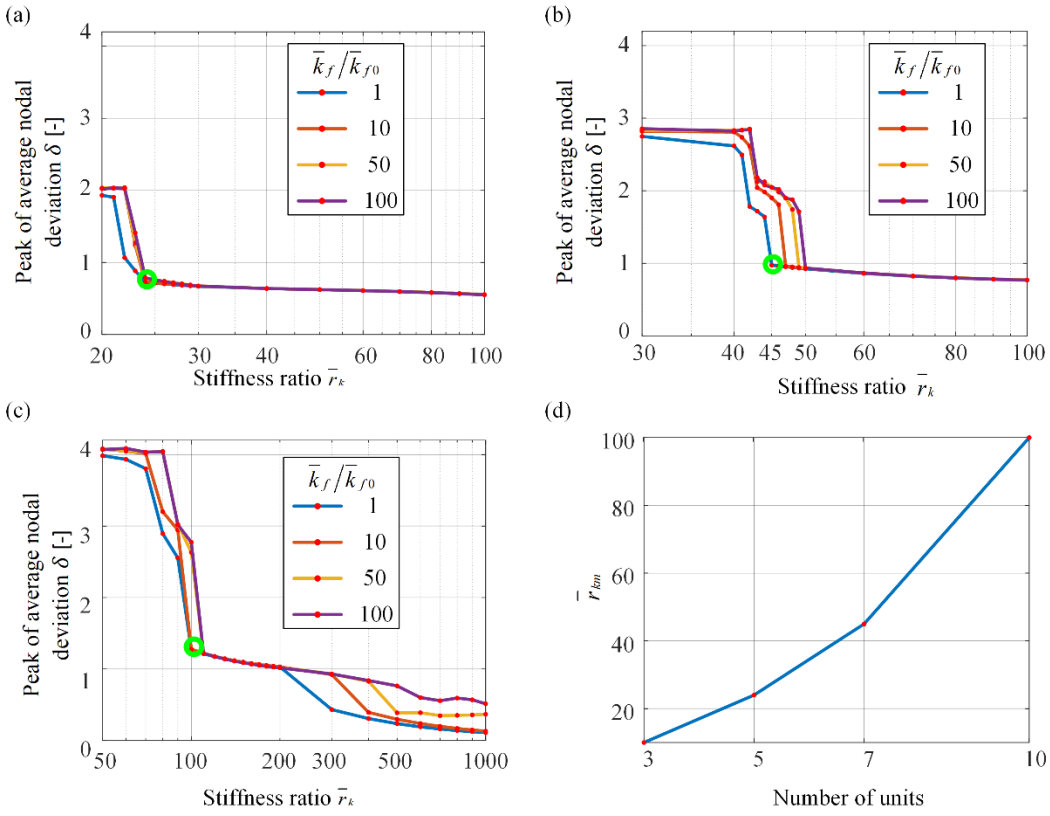

Figure 14. Stiffness ratio with respect to the nodal deviation for (a) a 5-unit, (b) a 7-unit, and (c) a 10-unit Miura origami sheet. In (a-c), the $\bar{r}_{km}$ is circled for the case where $\bar{k}_f/\bar{k}_{f0}=1$. (d) The critical value $\bar{r}_{km}$ for $\bar{k}_f/\bar{k}_{f0}=1$, which is the minimum stiffness ratio to avoid a "pop-up" deformation, is higher as more units are used in the Miura origami sheet.

3.3.3 Influence of Geometry on the Dynamic Deployment Process

In this Section, we present numerical simulation results to illustrate how the geometric parameters of the Miura origami sheet affect the dynamic deployment process. We specifically explore the influence of the sector angle γ and the crease length ratio $\bar{b}$. The geometric parameters under investigation are varied while the other parameters remain at their nominal values. In the nominal pattern, the sector angle $\gamma=60°$, crease length ratio $\bar{b}=1$, and the number of units in the sheet is three. In this geometric parametric study, the stiffness parameters are ($\bar{r}_k=100$, $\bar{k}_f/\bar{k}_{f0}=1$) and the deployment control rate is set to be 0.6 [-/sec].

With the given stiffness parameters, the study in Chapter 3 showed that the structure would deploy with little deviation from the rigid kinematic configuration ($\bar{r}_k = 100$, $\bar{k}_f / \bar{k}_{f0} = 1$ in Figure 8). By changing the geometric parameters, the effective stiffness will change, thus affecting the dynamic deployment behavior. In Figure 15 we show the deviation of dynamic deployment of a 3-unit Miura origami sheet with different sector angles and crease length ratios. We find that the peak nodal deviation δ increases with the increasing crease length ratio $\bar{b}$. This phenomenon can be explained by the increase of structural flexibility as reflected by the decreasing natural frequency shown in Figure 12a. By increasing the sector angle γ, the nodal deviations remain constant or increase slightly until they reach a boundary marked by a white dash-dot line in Figure 15. To the left and above the boundary line, the nodal deviations are much higher than that to the lower right side on the contour plot, indicating a qualitative change in the deployment behavior. To gain more insight into this discontinuity, we first perform two case studies: in Section 3.3.3.1, we fix the crease length ratio at 1 and vary the sector angle (yellow line in Figure 15), and in Section 3.3.3.2 we fix the sector angle at $60°$ and vary the crease length ratio (magenta line in Figure 15). In Section 3.3.4, we further explore the geometric influence, and show that this discontinuity is due to a second stable equilibrium of the structure.

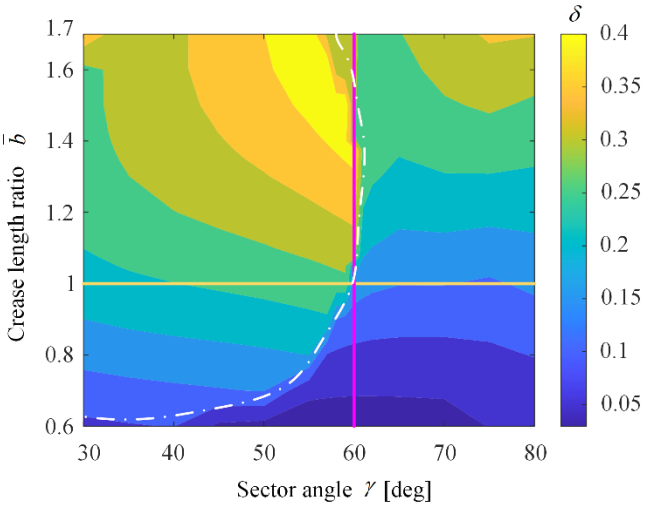

Figure 15. The nodal deviation of the dynamic deployment process of the Miura sheet structure with different geometric parameters. The sector angle γ is varied with the x axis and the crease length ratio $\bar{b}$ with the y axis. The magenta line shows the case when the crease length ratio is varied with a fixed sector angle at $60°$; the yellow line represents the case when the sector angle is varied with a crease length ratio fixed at 1.

3.3.3.1 Case study on the sector angle γ when $\bar{b}=1$

In this Section, we discuss the influence of the sector angle γ on the deployment dynamics when the crease length ratio $\bar{b}$ is set to 1. Figure 15a shows that the nodal deviation δ slightly increases as the sector angle increases in the range of $\gamma \in [30°, 59.4°]$. A sharp decrease in nodal deviation occurs between $\gamma = 59.4°$ and $59.6°$,which corresponds to the intersection of the contours near the white curve in Figure 15. This decrease occurs because the deployment process is qualitatively different between the structures with a sector angle of $\gamma < 59.4°$ and those with $\gamma \geq 59.4°$ (Figure 16). During the deployment process, the structure with $\gamma = 59.4°$ first snaps into a distorted configuration with a high deviation (Figure 16c). As the structure deploys, it first becomes more distorted (Figure 16d), and then, around the middle of the deployment process, it returns to a configuration that is near the rigid folded state. The structure then has little deviation until it becomes fully deployed (Figure 16e). The structure with $\gamma = 59.6°$ also deforms into a distorted configuration when it is first released (Figure 16f), but quickly returns near to the rigid

unfolding configuration (Figure 16g) and maintains little deviation until fully deployed (Figure 16h). This sharp drop in nodal deviation and the corresponding change in deployment behavior indicate that a slight change in sector angle can cause a qualitative change to the dynamic deployment process.

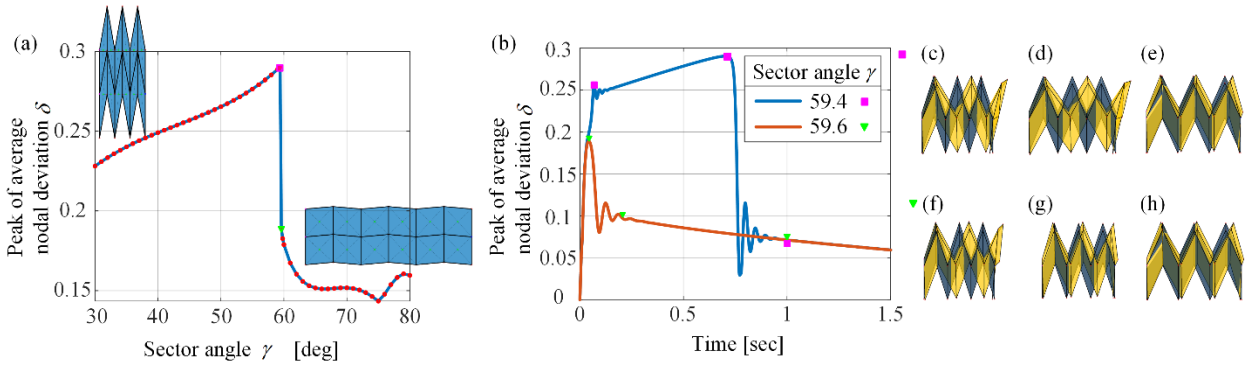

Figure 16. (a) Nodal deviation δ during the deployment process with respect to the sector angle (each dot represents the result of an individual deployment analysis). The two embedded images show the extreme values of sector angle $\gamma = 30°$ and $\gamma = 80°$. (b) Time history of the nodal deviation for the structures with different sector angles. The yellow color refers to the dynamic deployment configuration, while the blue color refers to the corresponding rigid unfolding configuration at the same stage of deployment. (c-e) are snapshots of the configuration during deployment for $\gamma = 59.4°$, in which (c) refers to 0.069 sec, (d) to 0.709 sec, and (e) to 1 sec, corresponding to the pink squares on the blue curve in (b). (f-h) are snapshots of the configuration during deployment for $\gamma = 59.6°$, in which (f) refers to 0.044 sec, (g) to 0.2 sec, and (h) to 1 sec, corresponding to the green triangles on the red curve in (b). The structures here have a crease length ratio of $\bar{b} = 1$.

3.3.3.2 Case study on the crease length ratio $\bar{b}$ when $\gamma = 60°$

In this Section, we discuss the effect of the crease length ratio $\bar{b}$ on the dynamic deployment behaviors of the Miura origami sheet, when the sector angle γ is kept at $60°$. Results in Figure 17a show that the nodal deviation δ increases and eventually approaches a constant value as the crease length ratio $\bar{b}$ increases. However, the curve shows a discontinuity in its middle part, which corresponds to the two intersections between the magenta line and the white curve in Figure 15. The overall increase of δ with $\bar{b}$ is because the structure becomes wider and thus softer with higher $\bar{b}$, which is consistent with the results in Figure 12a. We then

investigate the discontinuity in the relationship between δ and $\bar{b}$, which are the sudden increase of 41.5% in δ at $\bar{b}=[1.051,1.052]$ and the drop of 23.1% at $\bar{b}=[1.375,1.380]$. The deployment process is illustrated by the time history of deviation δ in Figure 17b. For $\bar{b}\in[1.052,1.375]$, the structure will be in a distorted configuration (distorted from the rigid kinematic configuration) at the beginning of the deployment process (shown in Figure 17b, Figure 17(f-g) and Figure 17(i-j)). This distortion will result in higher deviation δ than the structure with crease length ratio of $\bar{b}\in[0.6,1.051]\cap[1.380,1.7]$, in which the structure is mostly close to the rigid kinematic configuration during the deployment process (Figure 17b, Figure 17(c-e) and Figure 17(l-n)). The qualitative change in configuration indicates the existence of multiple equilibria of the Miura Origami sheet. The structure can approach different equilibrium configurations during deployment, depending on the shape of the origami pattern resulting in different levels of deviation from the rigid kinematic deployment path. The nodal deviation for different geometric patterns can differ by more than a factor of ten as shown in Figure 17a, which confirms the importance of the origami geometric effect on deployment dynamics.

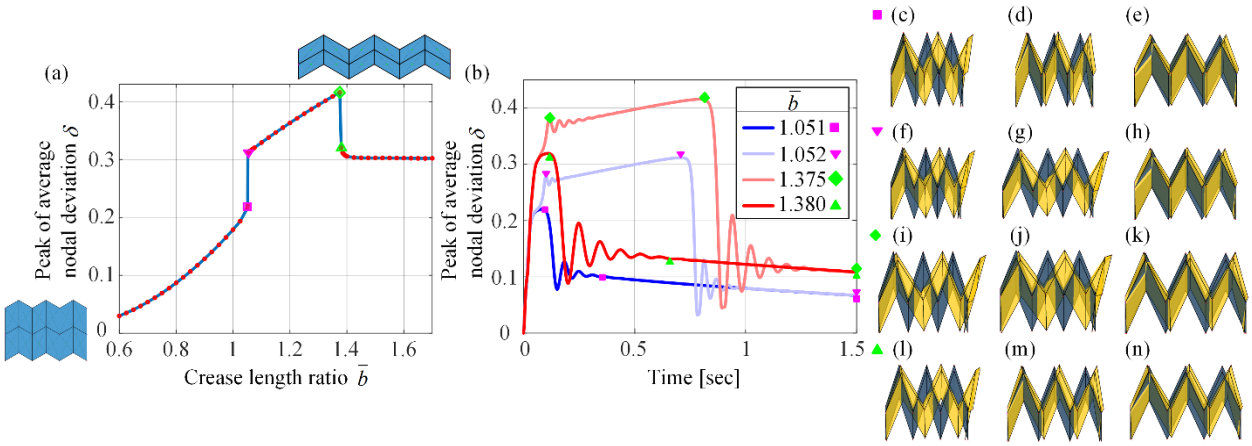

Figure 17. (a) Nodal deviation δ with respect to the crease length ratio $\bar{b}$ (each dot represents the result of an individual deployment analysis). (b) Time history of the nodal deviation for structures with crease length ratios of $\bar{b}=[1.051,1.052,1.375,1.380]$. Snapshots of the sheet configuration during deployment, where the yellow color refers to the dynamic deployment configuration, and the blue color refers to the corresponding rigid unfolding

configuration at the same stage of deployment. (c-e) are for $\bar{b} = 1.051$ at (c) 0.082 sec, (d) 0.35 sec, and (e) 1.5 sec, corresponding to the pink squares in (b). (f-h) are for $\bar{b} = 1.052$ at (f) 0.1 sec, (g) 0.71 sec, and (h) 1.5 sec, pink triangles in (b). (i-k) are for $\bar{b} = 1.375$ at (i) 0.116 sec, (j) 0.796 sec, and (k) 1.5 sec, green rhombi in (b). (l-n) are for $\bar{b} = 1.380$ at (l) 0.116 sec, (m) 0.65 sec, and (n) 1.5 sec, green triangles in (b). The structures here have a sector angle of $\gamma = 60°$.

3.3.4 Localized multistability during the dynamic deployment

The dynamic analyses in Section 3.3.3 show significantly different deployment behaviors for origami sheets with different geometric designs. In this section, we will demonstrate that these deviations occur because the structure can snap between different stable states during the deployment process.

We start with a case study to investigate the structural multistability by analyzing the structure with a crease length ratio $\bar{b} = 1.2$ and a sector angle of $\gamma = 60°$ where we observe the distinct increase in deviation as shown in Figure 17a. We use a quasi-static simulation to find stable equilibrium states of the structure and to verify that there do in fact exist multiple stable states. We use an iterative process on the static governing equations (delete the time varying terms and inertial/damping effects from the dynamic EOM), similar to Section 3.3.1, where the nodal positions of the origami are updated until we converge to a configuration that minimizes the sum of the internal forces in the structure. When we start the iterative process from the rigid folding configuration, we consistently converge to the first stable equilibrium state which has little deviation from the rigid folding orientation (dark blue images in Figure 18). To search for a second stable equilibrium state, we need to begin the iterative process from another initial state where the structure is already deformed. We pick an initial deformed state corresponding to the shape of the origami during a transient dynamic deployment (magenta images in Figure 18). With these initial conditions, the structure can converge to another stable equilibrium (yellow

images in Figure 18), which is markedly different from the first (blue images), and has a substantial deviation. Figure 18 shows the two stable states of the origami sheet and the transient shape of the sheet at different stages of the deployment process. When the dynamic process begins the structure snaps into the second stable equilibrium (0 to 0.06 sec Figure 18(a-c)) where it has a large deviation from the rigid folded state (Figure 18d). Furthermore, as the structure becomes more deployed this second equilibrium state deviates more from the rigid folded state (0.06 to 0.75 sec Figure 18(c, e)), which leads to a further increase in the nodal deviation (Figure 18d). As the origami reaches a more deployed state (0.8 sec Figure 18f) we can no longer find the same second stable equilibrium, even when we start the iterative process with a deformed initial configuration. While other stable equilibria may exist, the nearest stable equilibrium is the same as the first, and thus the structure snaps back to the first stable equilibrium during the dynamic deployment (0.8 to 1.1 sec Figure 18(f-g)). The dynamic deployment process experiences some transient oscillations after each time the structures snaps into a new configuration (~0.06 sec and ~0.9 sec in Figure 18d). For higher states of deployment, the transient dynamics closely follow the first stable equilibrium (Figure 18h).

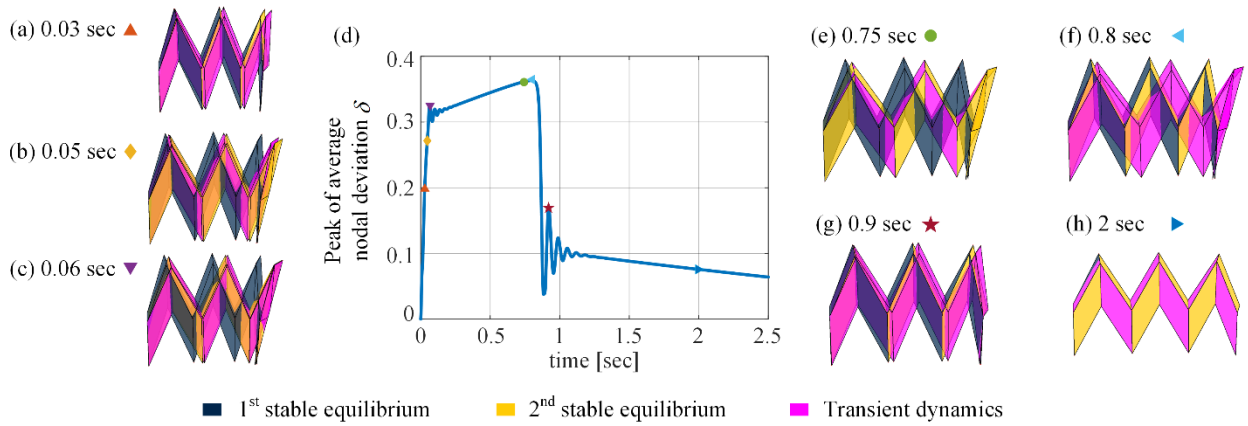

Figure 18. Stability analysis of a 3-unit origami sheet with crease length ratio $\bar{b} = 1.2$ *and sector angle* $\gamma = 60°$. *(d) Time history of nodal deviation* δ . *(a-c, e-h) Configurations of the stable equilibria and snapshots of the transient dynamic deployment at selected deployment stages. The yellow and blue refer to the two stable*

equilibria, and the magenta refers to the snapshot in dynamic deployment. The stiffness parameters are ($\bar{r}_k = 100,\ \bar{k}_f / \bar{k}_{f0} = 10$*).*

We next extend this same multistability analysis to other origami sheets with different sector angles and crease length ratios. The yellow region in Figure 19a shows the geometries where the structure snaps into and stays near the second stable equilibrium during the dynamic deployment process. The boundary of this region is also similar to the white curve in Figure 15, to the left of which the structure undergoes higher nodal deviation. We find that during the dynamic deployment structures with some geometries (Figure 19(b, d)) snap and oscillate near the second stable equilibrium, but structures with other geometries may not (Figure 19(c, e)). The structure is still multistable to the right of the boundary (i.e., two stable equilibria can be found in Figure 19(c, e)) but a snap does not occur during deployment. This different behavior is because the snap-through depends not only on the existence of multistability, but also other factors such as the initial strain energy that drives the deployment and the initial conditions of the system. Both quantities are well known to influence the response in nonlinear structural dynamics.

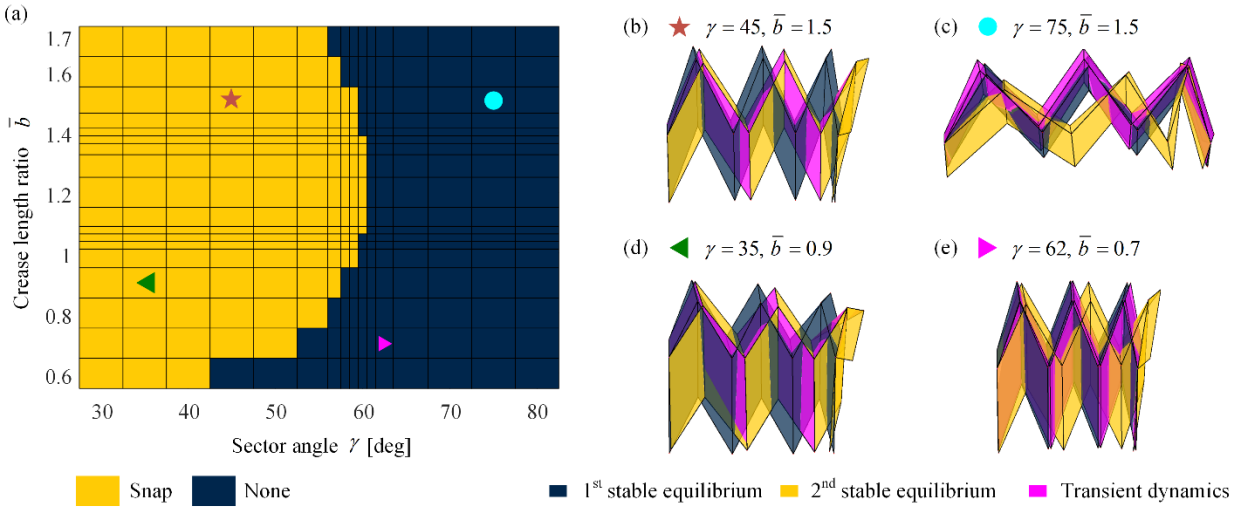

Figure 19. Dynamic behaviors and multistability of a 3-unit origami sheet with different crease length ratios and sector angles. (a) The yellow region represents the parameter sets with which the origami sheet snaps into and stays at the second stable equilibrium during the dynamic deployment process. (b-e) Configurations of the

two stable equilibria, blue and yellow, for selected pattern geometries. The magenta-colored shape is the deformed state of a snapshot from a transient deployment analysis that was used to find the second stable equilibrium. The stiffness parameters are ($\bar{r}_k = 100$, $\bar{k}_f / \bar{k}_{f0} = 10$).

From this parametric study, it is shown that the geometry, including pattern shape and number of units in the sheet, can affect the structural effective stiffness and modal eigenvalues, indicating that the structure properties can be varied by designing the origami pattern. Numerical simulation further shows significantly different dynamic response of the Miura origami sheet with different geometries. Under the same displacement control, structures with certain geometric designs are shown to be able to follow the rigid kinematic path better, which is explained by the multistability analysis, indicating that the origami geometry can be designed for more desirable deployment behavior. These results will provide a foundation for the exploration and understanding of origami design for desired deployment performance.

3.4 Influence of Deployment Control Rate

Prior Sections have illustrated how the stiffness and geometry of the structure affect the dynamic deployment process when the deployment rate is fixed to 0.6 [-/sec]. However, the deployment behavior also depends on how fast the structure is controlled to deploy. In our study, the structure is deployed while controlling the horizontal displacement at the right end with a constant velocity. Without loss of generality, we vary the deployment control rate from 0.05 [-/sec] to 1000 [-/sec]. To understand the influence of the deployment control rate, we perform analysis where we change the rate, and compute the average nodal deviations. In these studies, the nodal deviations are computed both with respect to the nominal rigid kinematic unfolding configuration, and with respect to a quasi-static deployment configuration (prediction considering the panel flexibility but not the inertial effect). The structure is a 3-unit Miura

origami sheet with geometric parameters ($\gamma = 60°, \bar{b} = 1$). We perform this rate analysis on structures with different stiffness parameters ($\bar{r}_k$, $\bar{k}_f / \bar{k}_{f0}$) and present the results in Figure 20.

3.4.1 Comparison between Dynamic Deployment and Rigid Kinematic Unfolding

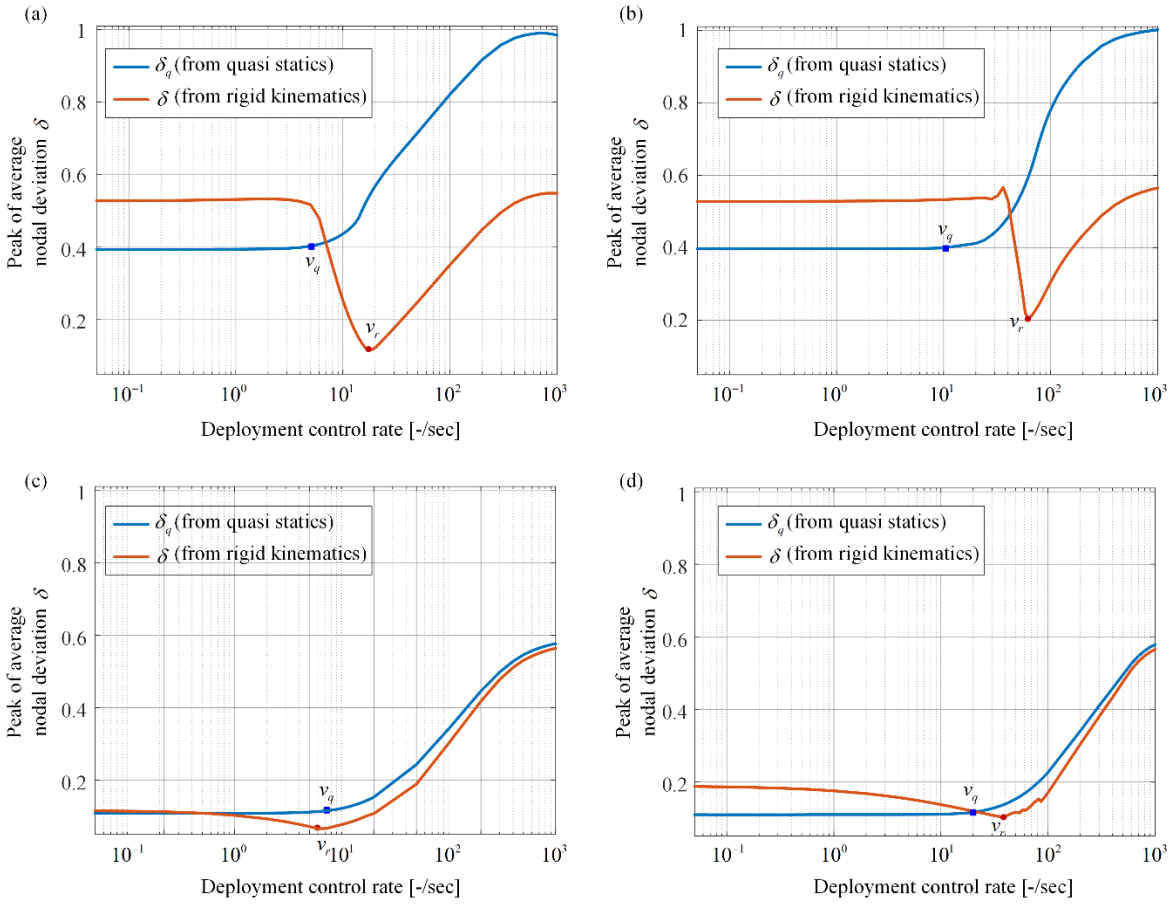

Figure 20. Nodal deviation with respect to the deployment control rate. A logarithmic scale is used for the deployment control rate in the x axis. The red curve shows the nodal deviation δ between the dynamic and rigid kinematic unfolding process. The blue curve shows the nodal deviation δ_q between the dynamic and quasi-static deployment The stiffness parameters are: (a) $\left(\bar{r}_k = 10,\ \bar{k}_f / \bar{k}_{f0} = 1\right)$, (b) $\left(\bar{r}_k = 10,\ \bar{k}_f / \bar{k}_{f0} = 10\right)$, (c) $\left(\bar{r}_k = 100,\ \bar{k}_f / \bar{k}_{f0} = 1\right)$, and (d) $\left(\bar{r}_k = 100,\ \bar{k}_f / \bar{k}_{f0} = 10\right)$.

In this Section, we derive the peak averaged nodal deviation δ between the dynamic deployment process and the nominal rigid kinematic unfolding to explore the rate effect. In Figure 20a, under extremely low and high deployment control rates, the structure deviates from the rigid unfolding configuration the most. When deployed slowly, the units inside the Miura origami sheet experience non-uniform deformation where the left units are stretched, and the right unit is compressed. This deformation occurs especially at the beginning stage when the structure is near folded, and the strain energy is high (Figure 21a-c). As the deployment control rate is increased, the sheet deploys more uniformly and the deviation decreases. There exists a critical value v_r for the control rate, where the structure experiences a minimum deviation. For the system with stiffness parameters of $\left(\bar{r}_k = 10, \bar{k}_f / \bar{k}_{f0} = 1\right)$ the critical rate is $v_r = 17$ [-/sec] with snapshots of the deployment process shown in Figure 21(e-g). If the deployment control rate continues to increase, then δ will increase again. At deployment rates that are much higher than v_r the structure will be stretched during the deployment (Figure 21(j-l)), and after it reaches a fully deployed state it will continue to undergo oscillations that deviate from the rigid unfolding path (Figure 21(k)). This type of analysis can provide guidance for selecting a deployment control rate which minimizes the deformation and deviation from the rigid kinematic deployment configuration.

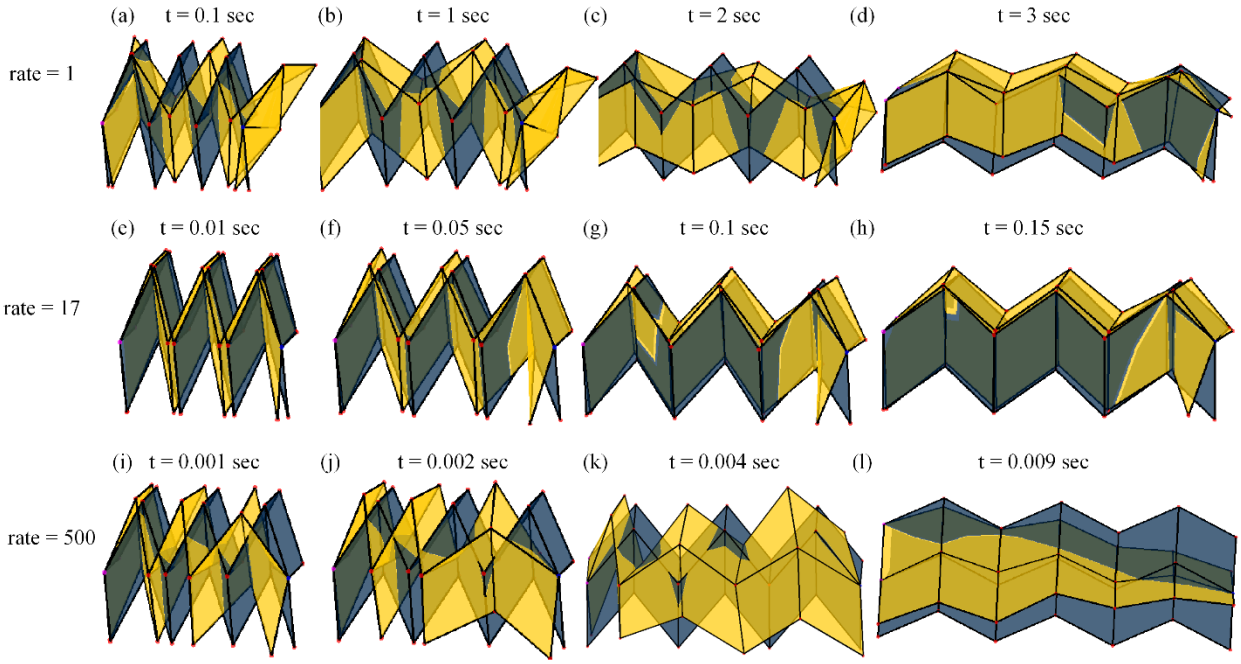

Figure 21. The deployment process of the structure with stiffness parameters $\left(\bar{r}_k = 10,\ \bar{k}_f / \bar{k}_{f0} = 1\right)$ *with the deployment control rate of (a-d) 1 [-/sec]; (e-g) 17 [-/sec]; and (h-k) 500 [-/sec]. The structure exhibits significantly different behaviors under the different deployment control rates. The yellow color refers to the dynamic deployment configuration, while the blue color refers to the corresponding rigid unfolding configuration at the same stage of deployment.*

The critical value of the deployment control rate v_r under which the structure achieves minimum deviation is affected by the stiffness properties. Rate control analyses are performed for structures with different stiffness parameters, and the results are presented in Figure 20(c-d). These results show a similar tendency as in Figure 20a where δ will first decrease to a minimum deviation at a critical rate v_r, and then increase with the increase in deployment control rate. By comparing Figure 20a with Figure 20b, and Figure 20c with Figure 20d where the stiffness ratios are kept constant ($\bar{r}_k = 10$ and $\bar{r}_k = 100$ respectively), but the fold stiffness $\bar{k}_f / \bar{k}_{f0}$ is increased, it can be seen that the structures with stiffer creases (b, and d) have a higher v_r than those with softer creases (a and c). The higher v_r is because structures with stiffer creases possess more strain energy and will undergo more non-uniform deformation induced by

the higher strain energy. Thus, the structure needs to be deployed faster to avoid the non-uniform deformations. Additionally, by comparing Figure 20a with Figure 20c and Figure 20b with Figure 20d where the creases stiffness is kept constant ($\bar{k}_f = 3.8\times10^{-7}$ ($\bar{k}_f / \bar{k}_{f0} = 1$) and $\bar{k}_f = 3.8\times10^{-6}$ ($\bar{k}_f / \bar{k}_{f0} = 10$), respectively), but the stiffness ratio is increased, we can see that the structures with a higher ratio $\bar{r}_k$ have lower v_r. This lower deployment rate for the structures with a higher stiffness ratio is because their relatively stiffer panels can better restrain the squeezing deformations among units and thus the structure can be deployed at a lower rate. Additionally, the higher stiffness ratio $\bar{r}_k$ (closer to the rigid kinematics unfolding scenario) results in an overall lower δ because there is less panel deformation and less deviation (i.e., similar to results from Chapter 3).

Under very fast deployment, there exists an upper limit on δ. For the structure in Figure 20a $\left(\bar{r}_k = 10, \bar{k}_f / \bar{k}_{f0} = 1\right)$ we approach the upper limit with the deployment rate close to 1000 [-/sec]. For that case, the maximum deviation δ occurs at a time of 0.004 sec during the deployment and the corresponding snapshot is shown in Figure 21j. The comparison between the snapshot of the dynamic deployment and the corresponding rigid configuration shows squeezing among the units, where the leftmost unit is compressed while the rightmost unit is stretched by the displacement control. The upper limit in deviation exists because of this large distortion between units. As the deployment control rate keeps increasing, the leftmost unit will become less compressed and the total δ will start decreasing slightly (Figure 20a).

3.4.2 More Insight on the Role of Inertia and Flexibility in Dynamic Deployment

The deviation of the origami dynamic deployment from the nominal rigid kinematic unfolding configuration originates from both the panel flexibility and the inertial effects. In this

Chapter, the dynamic deployment is compared with the quasi-static deployment process (which includes the panel flexibility but not the inertial effect) to understand more about the role of inertia. The nodal deviation between the dynamic and the quasi-static deployment configurations is denoted by δ_q. At low deployment control rate, δ_q remains constant, meaning that the inertial effect on the dynamic deployment process does not change much with the rate. As the control rate exceeds a turning point v_q, shown as a blue square in Figure 20, the nodal deviation δ_q increases corresponding to an increase of the inertial effects.

To gain more insight on the effects of the panel flexibility and system inertia, we compare the two types of deviation, δ and δ_q. Both the effects of flexibility and inertia are reflected in δ while only the inertial effect is reflected in δ_q. At low control rate, the cases with inertia have a larger deviation ($\delta > \delta_q$) because inertia dependent oscillations occur after the initial release of strain energy which drives the structure into a non-uniform squeezed shape, (Figure 21a). At higher control rates, $\delta < \delta_q$, due to the combined inertia and flexibility effects.

Additionally, the turning point changes with the stiffness of the structure. By comparing Figure 20a with Figure 20b, as well as Figure 20c with Figure 20d, the structure with stiffer folding creases (b and d) has a higher v_q, meaning that the quasi-static panel deformation dominates the overall nodal deviation for a wider range of deployment rates. On the other hand, the stiffness ratio $\bar{r}_k$ has relatively low influence on v_q, as can be seen by comparing Figure 20a with Figure 20c, as well as Figure 20b with Figure 20d.

3.5 Conclusion

In Chapter 3, we investigate the dynamics of deployment of a Miura origami sheet. For the first time, through analyzing a dynamic model that includes the combination of panel inertia and flexibility, we uncover new phenomena and qualitative features that have not been observed previously and cannot be derived via traditional quasi-static and rigid kinematic unfolding analyses. Some of the system behaviors observed in the analysis are also shown experimentally on a test prototype. By analyzing the deviation of the dynamic deployment configurations from those of the traditional approaches, the tools we developed as well as the outcomes can provide quantitative information (e.g., parametric space) of where the deployment dynamics would become important for better system design and control.

We develop the dynamic model by considering panel inertia and flexibility, where we discretize the structure by using equivalent lump mass elements. We derive the nondimensionalized equations of motion and perform analysis to gain general understanding of the system dynamic behaviors during deployment. The deployment of the origami sheet is facilitated by the stored strain energy in the creases when the structure is folded and a displacement control on one end point of the sheet.

With different stiffness, the structure may exhibit qualitatively very different deployment behaviors. In cases where the fold stiffness to panel stiffness ratio ($\bar{r}_k$) is low, the structure may undergo a large global bending 'pop-up' state. This pop-up occurs at different stages depending on the stiffness ratio $\bar{r}_k$. As $\bar{r}_k$ becomes sufficiently large, the dynamic deployment would be closer to the rigid kinematic unfolding configuration without pop-ups. Specifically, there exists a critical value $\bar{r}_{km}$, below which the structure would undergo large pop-up motion. Such $\bar{r}_{km}$ value

can vary with the number of units in the origami sheet, and in particular the $\bar{r}_k$ value needs to be higher for origami sheets with more units to avoid pop-up.

It is shown that apart from the material stiffness parameters, the pattern geometry including the crease length ratio and the sector angle, can influence the structural effective stiffness properties, and thus affect the transient dynamics of the deployment process. It is discovered that the origami sheet possesses multiple stable equilibria under different geometric parameters and may reconfigure between the stable equilibria during dynamic deployment.

We found that the dynamic deployment performance can also be affected by changing the control deployment rate. Under slow rates, the origami sheet undergoes squeezing among its units, while it undergoes stretching under fast rates. The structure can best follow the rigid kinematic configuration under a certain value of the control rate, which also varies with the structure properties, such as fold stiffness. These results indicate that the displacement control can be utilized to obtain more desirable dynamic deployment performance.

Overall, this research provides a foundation for the exploration and understanding of the dynamic characteristics of origami sheet deployment. The tools and insights developed can be utilized to design for desired (e.g., smooth and fast) deployment or intentional reconfiguration of origami sheet structures. Moreover, they are especially valuable in raising awareness of new phenomena that have not been observed in the past, and providing original guidelines to create origamis with design parameters (e.g., material and geometric properties) and operating conditions (e.g., deployment rate) that are outside the traditional range of consideration. In other words, this basic research is impactful in extending our fundamental knowledge and expanding our comfort zone with the deployment dynamics of origami.

Chapter 4 Deployment Dynamics of Fluidic Origami Tubes

Building on the model presented in Chapter 2, we performed analysis to investigate the deployment dynamics of a single Miura origami tube and present the finding in this chapter (Chapter 4). Chapter 4 covers the problem setup (Section 4.1) and the discussions of the influence of fluidic pressure and structural stiffness (Section 4.2 and Section 4.3), multistability landscape (Section 4.4), deployment rate (Section 4.5), on the deployment dynamics of the Origami single tube structure.

4.1 Deployment Setup

In the deployment of fluidic origami tubes, we assume that the two ends of the tube are sealed off. The structure initially rests at its folded state (33.2% of full deployment as in Figure 22e) and is deployed by increasing the internal pressure. The deployment extent is defined by the ratio between the axial projection of the tube L_{ax} and the length of the tube when it is deployed flat (Figure 22e). We restrict axial movement on the left end of the tube and release the other end to move freely. In the following analysis, the fixed left end is achieved by fixing node 8 and 15 in all directions and fixing the axial movement of node 1 and 22 (Figure 22 (c-d)).

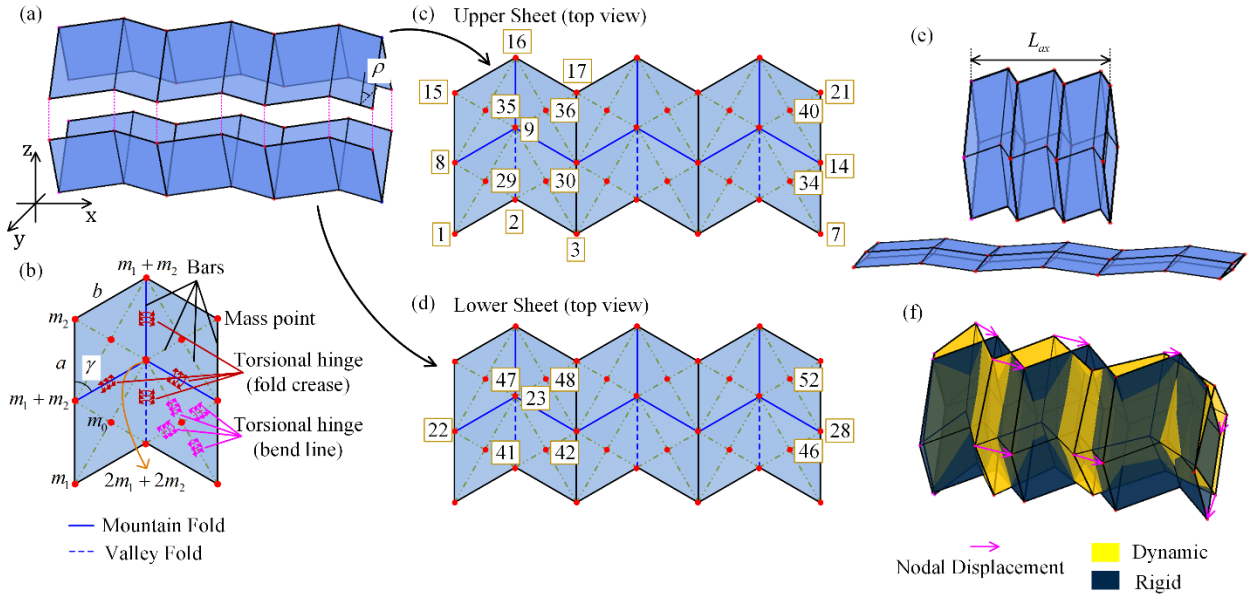

Figure 22. (a) A 3-unit Miura origami tube consists of two identical Miura origami sheets, the upper sheet (c) and the lower sheet (d). (c-d) Node numbering in the upper and lower sheets. (b) A bar and hinge representation of a Miura origami unit. The blue dashed and solid lines represent the valley and mountain folds respectively (or vice versa). (e) L_{ax} is defined to be the length of axial (x direction) projection of the origami tube. (f) The pink arrows show the nodal displacement between the dynamic configuration and the corresponding rigid configuration.

s

4.2 Quasi-Static Deployment

We first explore the deployment behavior using a quasi-static analysis. The analysis will provide us with information on the deployed configuration under pressurization, which are affected by the magnitude of the internal fluidic field pressure and the structural stiffness. This is because the deployed configuration is the result of force balance between the pressure load and reactive forces of the structure. We assume a space-invariant fluidic field inside the tube and perform quasi-static analysis on the deployment. We vary the pressure magnitude $\bar{P}$ in our numerical analysis and derive the configuration of the tube under each pressure magnitude, with different stiffness parameters $\left(\bar{r}_k, \bar{k}_f\right)$. For each case with a certain set of stiffness parameters, we increase the pressure magnitude over multiple incremental steps, and for each step we iterate to find the configuration under force balance, which is the so-called incremental and iteration

method. For each step, the structure inherits the converged configuration from the previous step r_{n0} and is then simulated with an increased pressure magnitude, where the first step takes on the rest configuration where the deployment starts. The structure configuration numerically converges after several iterations, where we use $\bar{U} = \bar{K}^{-1}\left[\bar{F}_{ex}\left(\bar{P}\right) - \bar{F}_{in}\right]$ to equilibrate the resultant reactive force, where $\bar{U}$ is the nodal displacement; $\bar{K}$ is the stiffness matrix; $\bar{F}_{ex}\left(\bar{P}\right)$ is the external load from fluidic field and is a function of pressure magnitude $\bar{P}$ (note that the word *external* here refers to loads applied onto the numerical model, rather than the location of pressure within the tube); $\bar{F}_{in}$ is the internal reactive force from panel and crease deformation. The structure takes on an updated configuration $\bar{r}_{n,i} = \bar{r}_{n,(i-1)} + \bar{U}$ in the *i*-th iteration. Because the external load from pressure is always perpendicular to the panels, the term $\bar{F}_{ex}$ is updated after each iteration when the configuration $\bar{r}_n$ changes. The internal reactive force $\bar{F}_{in}$ is also iteratively updated through the process. For better presentation and illustration, in the rest of the paper, we normalize the applied pressure $\left(\bar{P}\right)$ using $\left(\bar{P}/\bar{P}_0\right)$, where $\bar{P}_0 = 3.8\times10^{-6}$.

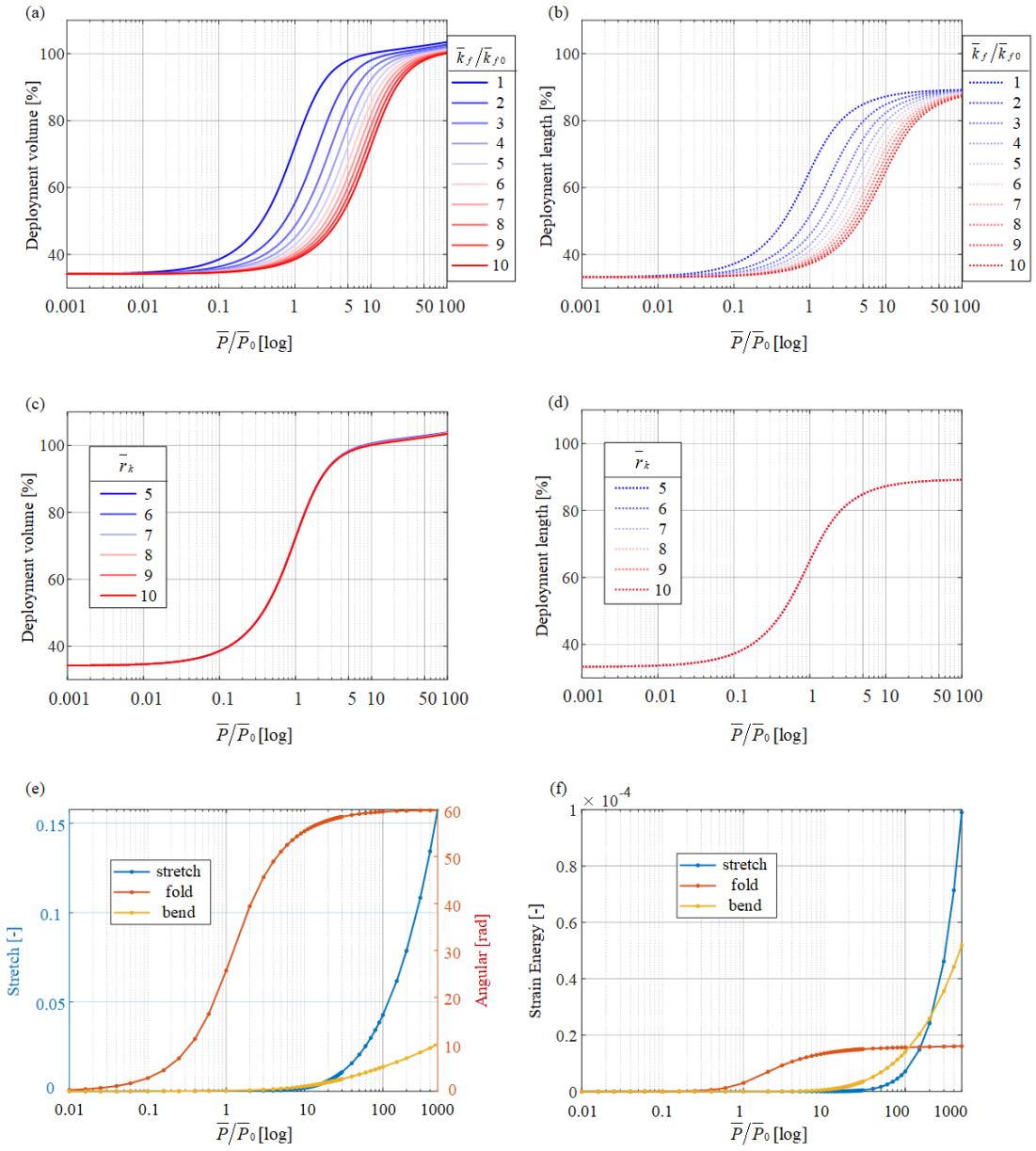

Figure 23. (a-d) The quasi-static deployment extent of the origami tube versus pressure for different folding stiffness $\bar{k}_f$ and stiffness ratios $\bar{r}_k$. The pressure is in log scale as shown by the lower x-axis. The stiffness ratio in (a, b) is constant at $\bar{r}_k = 10$, and the folding stiffness in (c, d) is constant at $\bar{k}_f / \bar{k}_{f0} = 1$. The deployment extent is described by the volume (a, c) and the end-to-end length (b, d), which are represented by the groups of solid and dotted lines respectively. (e) The deformation of the entire structure, including the panel stretching deformation represented by bar elongation of the model, the panel bending deformation by angular rotation at hinges, the crease folding deformation by angular rotation at folding creases. (f) The strain energy decomposed into the energy from panel stretching and bending deformation, and the crease folding deformation.

Figure 23(a-d) show the deployed configuration of the origami tube derived from the quasi-static analysis, in which the lower horizontal axis is the normalized pressure magnitude in log scale, and the vertical axis is the deployment extent. We use both the volume denoted by

solid lines and the axial length denoted by dotted lines to describe the deployment configuration. Specifically, instead of the absolute value of the volume the ratio is shown as a percentage of the tube volume under elastic deformation over the maximum volume without considering panel deformation. For axial length, the ratio of the tube axial length over the length at a fully deployed flat state is selected.

In Figure 23a, curves in color from blue to red represent tube with stiffer folding creases. They all share a similar tendency that the tube has a greater deployment extent when a higher pressure is applied. The deployment extent in volume (Figure 23a) can exceed the maximum volume under rigid folding assumption under high pressure, indicating that tube considering panel elastic deformation can be inflated. The maximum deployment extent in length (Figure 23b) is around 89% regardless of the pressure, which corresponds to the length of the maximum volume state. The tube length and volume together show that by increasing the internal pressure $\bar{P}/\bar{P}_0$, the tube is deployed until its maximum length is reached and cannot be further deployed in length even when higher pressure is applied. The increasing volume in the inflated tube is due to panels stretching instead of elastic deformation at fold creases, which can be seen from the strain energy in Figure 23(e, f). In Figure 23(e, f), at low pressure magnitudes the majority of the deformation and the strain energy are from crease folding, because the structure undergoes deployment with little panel stretching or bending deformation. As the pressure continues to increase, the length levels off at around 89% and the volume starts to exceed the maximum volume. From the deformation and strain energy plots, the crease folding deformation and the corresponding strain energy also level off, while the stretching deformation increases with a sharp slope, and the stretching energy exceeds the folding energy, indicating the structure inflates rather than deploys. Additionally, comparing the curves in Figure 23ashows that for

structures with a higher folding stiffness $\bar{k}_f$, a higher pressure is needed to reach the same extent of deployment as a structure with a lower $\bar{k}_f$. On the other hand, the stiffness ratio $\bar{r}_k$ does not affect the deployment because there is almost no panel deformation during the quasi-static deployment (Figure 23c, d).

4.3 Influence of Pressure Field on Structural Properties

For the dynamic deployment, we assume a space-invariant fluidic field with pressure applied as a step function in time.

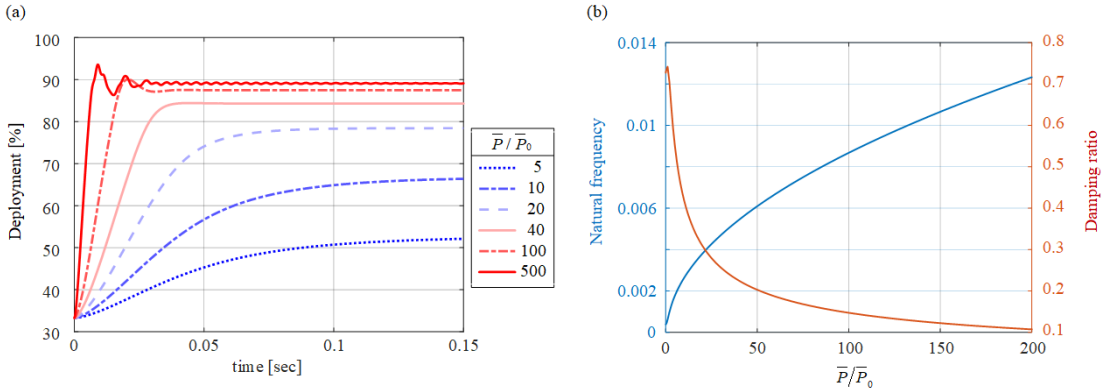

Figure 24. (a) Time history of the dynamic deployment process for different pressure magnitudes. The deployment stage is represented in percentage of the ratio between the axial projection $\bar{L}_{ax}$ of the structure at that stage over that of a fully deployed flat tube. (b) The first mode natural frequency and damping ratio vary with internal pressure magnitude. The eigen analysis is performed to the stable configuration at each pressure magnitude. The stiffness parameters of this structure are $\left[\bar{r}_k = 10, \bar{k}_f / \bar{k}_{f0} = 10\right]$.

From the dynamic analysis, it can be observed that the internal fluidic field affects both the extent of deployment and the transient process. Figure 24a shows the time history of the dynamic deployment of the structure with stiffness parameters $\left[\bar{r}_k = 10, \bar{k}_f / \bar{k}_{f0} = 10\right]$ and damping coefficients $\left[\bar{c}_b / \bar{r}_k \cdot \bar{k}_f,\ \bar{c}_f / \bar{k}_f\right] = [2.6, 1.3] \times 10^5$. For low pressure magnitudes, the structure exhibits an overdamped behavior, as shown by the smooth curve in blue. When the pressure increases to $\bar{P}/\bar{P}_0 = 100$, there is an overshoot in the axial direction, where the tube first deploys to an overstretched state and then comes back without much oscillation to the settled state

corresponding to the applied pressure. When the pressure magnitude further increases, more axial oscillations are observed, showing that the structure is underdamped. The switch from an overdamped system into an underdamped system with increased pressure magnitude indicates that the internal fluidic field can influence the effective structural stiffness which in turn affects the effective system damping and the resulting deployment behavior. An eigen analysis on the stable equilibria of this structure under different pressure magnitudes is shown in Figure 24b. It shows that the natural frequency increases and the damping ratio decreases as the internal pressure increases.

To get further understanding of the structural properties, we perform analysis on structures with different stiffness under varied pressure fields. In Section 4.2, it shows that structural folding stiffness has a more significant influence than the stiffness ratio on the deployment configurations, thus in this analysis we select the folding stiffness as the varied stiffness parameter. Figure 25 shows an eigen study with varied stiffness and pressure parameters. Each point on this contourplot corresponds to a stable equilibrium of a structure with certain fold stiffness under designated pressure magnitude, the shape of which can be affected by both the pressure and the stiffness parameters. Figure 25c shows the deployment extent of each configuration of the structure with certain folding stiffness under a certain pressure magnitude. The structure with softer folding creases under higher pressure magnitude settles at a greater deployment extent. Figure 25b shows the effective damping ratio where the region in white represents the overdamped systems, while the colored region stands for the underdamped systems. Dynamic simulations for four selected sets of parameters have been performed and the time history in Figure 25 shows these four cases. For the datapoint selected from the overdamped region, the time history shows a smooth but slow deployment process; for the data point selected

in the underdamped region, the structure will have overshoot and possibly oscillations during the deployment; for the datapoint selected at the boundary between the overdamped and underdamped regions, the structure undergoes fast and smooth deployment, which is close to a critically damped system. The change of structural properties under varied pressure fields implies the possibility to achieve certain deployment performance by controlling the applied pressure field instead of changing the structure itself. Even though this eigen analysis is performed on the stable equilibria, it can still shed light on the parametric design for the structure to achieve desired dynamic deployment behavior.

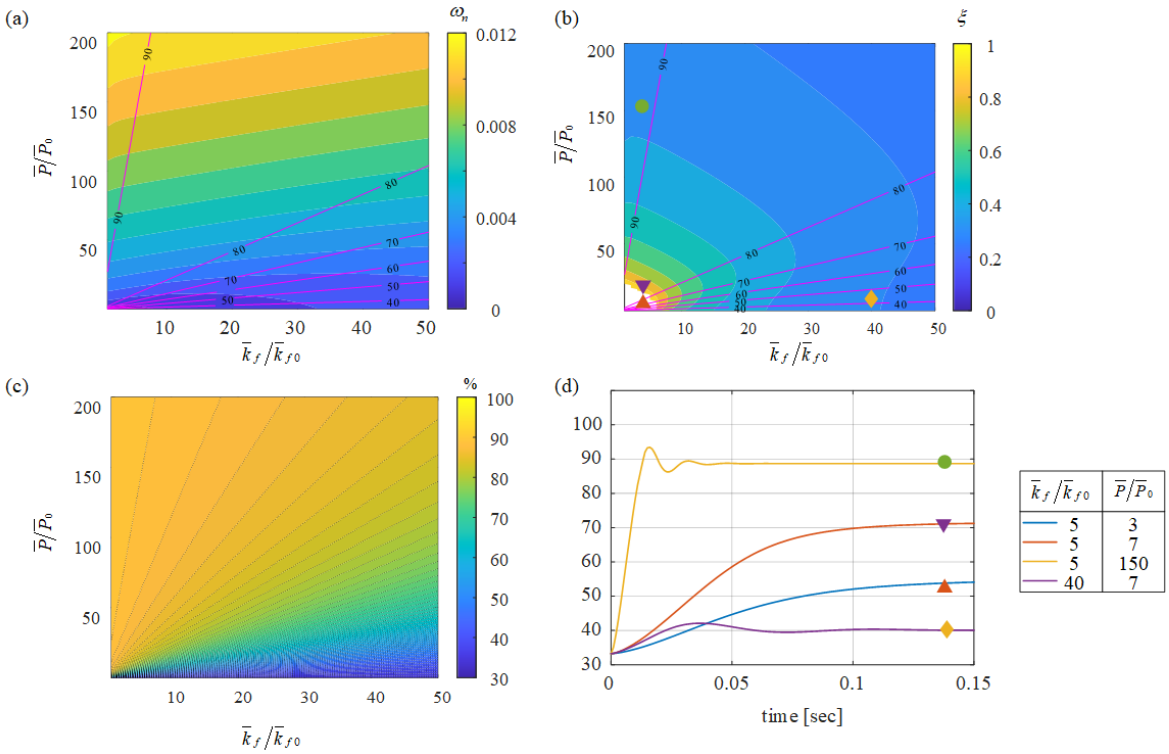

Figure 25. The first mode natural frequency ω_n (a) and the damping ratio ζ (b) of the Miura origami tube with different stiffness parameters under different pressure magnitudes. The stiffness parameter is varied with the x-axis and the pressure magnitude with the y axis. (c) The configuration of each stable equilibrium that the eigen analysis is performed on is represented by the deployment extent. (d) Time history of the dynamic deployment of the four (stiffness, pressure) sets from (b).

4.4 Multiple Stable Equilibria

The magnitude of pressure can also change the deployment behaviors qualitatively. Here we introduce the average nodal deviation δ to describe the distortion or system deformation for a certain dynamic configuration as compared to the rigid-folded configuration derived based on rigid kinematics assumptions. We select the rigid-folded configuration with the same axial length L_{ax} to be the baseline (blue configuration in Figure 22) and calculate the differences between the corresponding nodes from the dynamic (yellow configuration in Figure 22f) and rigid-folded configurations denoted by the pink arrows. The δ is then defined as the average of the difference among all the corresponding nodes.

For the origami tube with stiffness parameters $\left[\bar{r}_k = 10, \bar{k}_f / \bar{k}_{f0} = 1\right]$ and damping coefficients $\left[\bar{c}_b / \bar{r}_k \cdot \bar{k}_f,\ \bar{c}_f / \bar{k}_f\right] = [7.8, 3.9] \times 10^4$, we find three very different groups of deployment behaviors depending on the amplitude of the pressure: (1) When the pressure is low ($\bar{P}/\bar{P}_0 < 12$), the structure expands (Figure 26c), oscillates in the axial direction (Figure 26d), and comes to rest at configurations with little deviation from the rigid-folded state (Figure 26e). The average deviation shown in Figure 26b remains low throughout the deployment. As the pressure increases, the deployment extent of the settled configuration increases when comparing the dashed and dotted blue curves in Figure 26a. Results also show that when the pressure is within this range, the structural oscillation frequency and stiffness increase with increased fluidic pressure. (2) When the normalized pressure $\bar{P}/\bar{P}_0$ takes on value in the range of [12, 30], the structure snaps (Figure 26f) and oscillates around a configuration that is highly distorted from the rigid-folded configuration with significant global bending (Figure 26g-h). Such different deployment behaviors are also reflected in Figure 26b where the deviation δ jumps to a peak value and remains high throughout the dynamic simulation, meaning the structure does not

deploy along the nominal rigid-folding path and remains distorted. (3) When $\bar{P}/\bar{P}_0$ is higher than 30, the structure initially snaps to a highly distorted and bent configuration (Figure 26i) like in Group (2), but then snaps back to the undistorted or nominal shape. When it snaps back to the nominal shape, it temporarily reaches a configuration that is stretched out, as shown in Figure 26j. This transient configuration, also denoted by a blue square in Figure 26a, is more deployed and flatter than the maximum volume state (Figure 23a). The deployment extent among the three units of the tube is uneven, indicating non-negligible panel deformation with a relatively higher average nodal deviation δ as shown in Figure 26b. The structure finally settles near the rigid state with a low δ (Figure 26k).

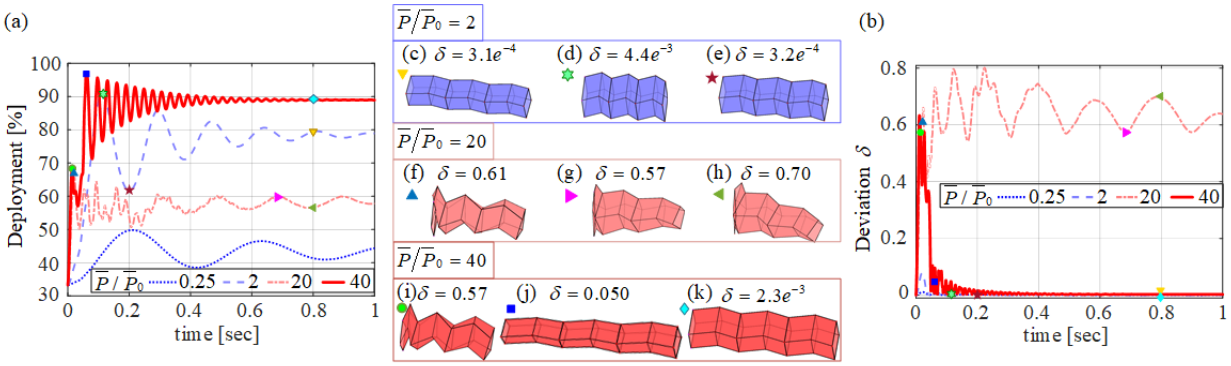

Figure 26. (a) Time history of the dynamic deployment process under a step input of the pressure with different magnitudes. The snapshots are shown by (c-k) for $\bar{P}/\bar{P}_0 = [2, 20, 40]$ *respectively. (b) Time history of the nodal deviation* δ *for the structure under different magnitudes of the pressure. The stiffness parameters for this structure are* $\left[\bar{r}_k = 10, \bar{k}_f/\bar{k}_{f0} = 1\right]$.

In order to explain the three types of deployment behaviors, we explore the multiple stable equilibria of the origami tube. To derive the stable equilibria, we perform an energy minimization process where we apply a certain internal pressure $\bar{P}/\bar{P}_0$ and allow the structural configuration to converge to a stable equilibrium starting from a given perturbed initial configuration $\bar{r}_{n0}$. We iterate by using$\mathrm{U} = \mathrm{K}^{-1}(\mathrm{F_{ex}}\text{-}\mathrm{F_{in}})$ $\bar{U} = \bar{K}^{-1}\left[\bar{F}_{ex}(\bar{P}) - \bar{F}_{in}\right]$ to equilibrate the

resultant reactive force and update the configuration by $\bar{r}_{n,i} = \bar{r}_{n,(i-1)} + \bar{U}$. We derive two stable equilibria using this approach. For the first stable equilibrium, we start the process from the rigid-folded state of the tube and converge to a stable state with slight panel deformation, but no significant nodal deviation. For the second stable equilibrium, we start with an initial condition sufficiently different from the rigid-folded state, which we take from the transient process in this analysis, and we converge to a second stable state with a high level of distortion. In addition to the pressure field, the structural properties can also exert an influence on the multistability landscape. In the following Sections, we discuss the influence of both the pressure field and the structural stiffness on the multistability landscape.

4.4.1 Influence of Pressure Field on Stable Equilibrium

In this Section, we vary the internal pressure magnitude and perform equilibrium stability analysis on the structure. Figure 27a shows that two stable equilibria exist for all the different internal pressures explored. For the first stable equilibrium, the structure deploys more with an increased pressure magnitude. For the second stable equilibrium, the percent deployment first decreases and then increases again. This is because the second stable equilibrium has global bending in the *y* and *z*-direction. With the pressure $\bar{P}/\bar{P}_0 \leq 0.4$, the second stable equilibrium bends and rotates in the transverse direction (Figure 27b-c), resulting in a decrease in the length of the axial projection. When $\bar{P}/\bar{P}_0 > 0.4$, the second equilibrium configuration does not bend further, and increases in length as the pressure increases. In the dynamic scenario, the structure starts from and stays around the first branch during the deployment when pressure $\bar{P}/\bar{P}_0 < 12$ is applied. When $\bar{P}/\bar{P}_0$ is within [12, 30], the dynamic deployment of the tube settles at the highly

distorted equilibrium. In this range, the initial excitation of applying the step fluidic pressure provides sufficient energy to overcome the energy barrier between the two stable equilibria, which causes the structure to snap and settle at the second stable equilibrium. When $\bar{P}/\bar{P}_0$ is higher than 30, the structure initially snaps into the second stable equilibrium, then it snaps back and settles at the first stable equilibrium. This indicates that after the initial impact, the fluidic pressure field provides enough energy for the structure to overcome the energy barrier twice to snap through and snap back during the transient oscillation.

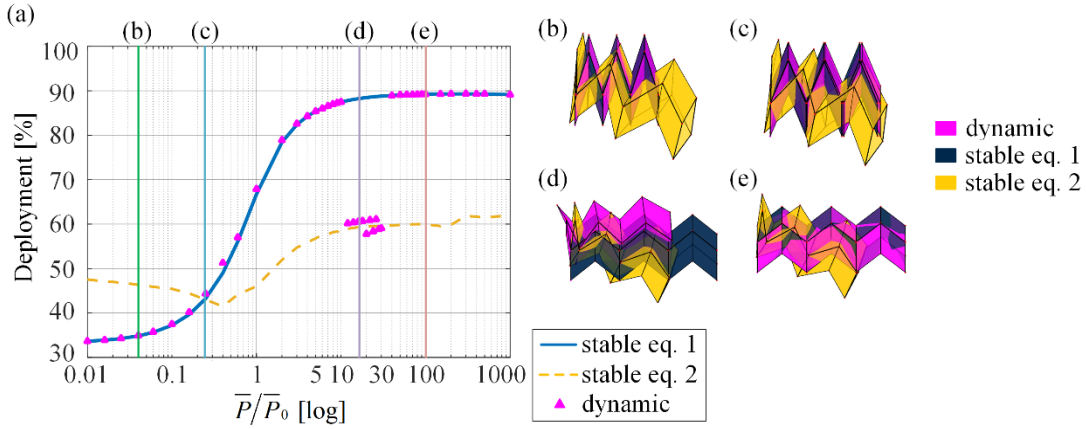

Figure 27. (a) The two stable equilibria and the settled dynamic configuration of the structure under different magnitudes of pressure are shown with respect to the length of the tube axial projection. (b-e) The comparison among the two stable equilibria and the settled dynamic configuration in different colors under pressures of $\bar{P}/\bar{P}_0 = [0.04,\ 0.25,\ 16,\ 100]$ *respectively.*

4.4.2 Influence of Stiffness on Stable Equilibria

Since both the pressure field and structural stiffness can affect the energy barrier that the structure needs to snap through, we perform a thorough investigation on structures with various stiffness under different pressure fields. Based on the pressure field study in Section 4.3, in Figure 28(a-d) the pressure magnitudes are selected such that the structure exhibits snap-through or snap-back behaviors under certain stiffness parameters.

Figure 28(a, b) show the settled configurations of structure with different folding stiffness $\bar{k}_f$. From dynamic analysis in Section 4.3, the structure with folding stiffness $\bar{k}_f = 1$ snaps though when $\bar{P}/\bar{P}_0 = [20,30]$. By varying the folding stiffness as in Fig. 21(a-b), the structure with different folding stiffness still possesses these two distinct stable equilibria. With stiffer folding creases, under a certain magnitude of pressure, both the two stable equilibria and the settled dynamic configuration become less deployed because of the higher reactive forces at the folding creases. The dynamic deployment process shows that structure with low folding stiffness tends to snap through under fixed pressure magnitude, while those with stiffer folding stiffness are less likely to snap through due to the relatively higher energy barrier. There exists a critical value for the folding stiffness $\bar{k}_{fcr}$, under which the structure has the first type of deployment with snap-through, otherwise the structure undergoes the second type of deployment without snap-through. This critical folding stiffness increases with the magnitudes of the internal pressure, for example $\bar{k}_{fcr}/\bar{k}_{f0} = 3$ for $\bar{P}/\bar{P}_0 = 20$ and $\bar{k}_{fcr}/\bar{k}_{f0} = 4$ for $\bar{P}/\bar{P}_0 = 30$. On the other hand, Figure 28(c, d) show that the stiffness ratio between panel bending and crease folding can hardly influence the shape of the two stable equilibria. The structure also tends to stay at the same stable equilibrium during the dynamic deployment process by changing the panel bending stiffness, indicating that changing the panel bending stiffness can result in little influence on the dynamic performance. This analysis shows that the dynamic deployment behaviors, as well as the stable equilibria, can be affected by changing the stiffness of origami tubes. We can design the deployment process by selecting a certain set of stiffness parameters and pressure magnitudes.

To obtain further understanding, Figure 28e considers both factors including the structure stiffness and pressure field. Each color block corresponds to a structure with certain folding

stiffness and under certain magnitudes of step input pressure. We use different colors to represent the dynamic deployment behaviors. The horizontal direction of this contourplot corresponds with Figure 28(a, b), where the structure with soft folding creases tends to snap through under fixed pressure magnitudes. The vertical direction of this contourplot shows that structures with fixed folding stiffness will have regular deployment with a low level of distortion under low pressure magnitudes (shown by the blue blocks). The structure will snap through and stay at the distorted stable equilibrium when the pressure magnitude increases (shown by the yellow blocks). In this scenario, the structure obtains energy from the pressure field to overcome the energy barrier. When the pressure becomes high enough, the structure will undergo snap through twice and settle at the regular less-distorted state, as shown by the magenta blocks. The two critical values of the pressure magnitude increase as the folding creases become stiffer, as also shown in Figure 28(a, b).

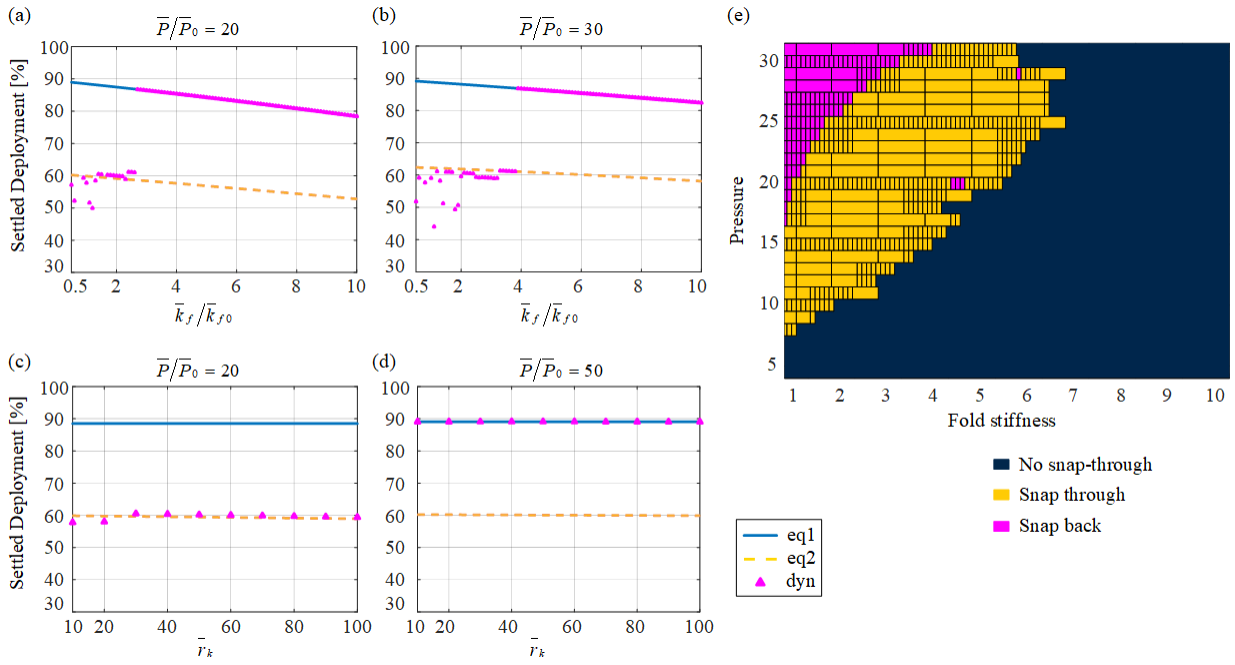

Figure 28. (a, b) The two stable equilibria and the settled dynamic configuration of structure with different folding stiffness with pressures of $\bar{P}/\bar{P}_0 = [20,30]$ *respectively. The stiffness ratio is kept constant at* $\bar{r}_k = 10$. *(c, d) The two stable equilibria and the settled dynamic configuration of structure with different stiffness ratios with*

pressures of $\bar{P}/\bar{P}_0 = [20, 50]$ respectively. The folding stiffness is kept constant at $\bar{k}_f/\bar{k}_{f0} = 1$. (e) The contourplot of the dynamic deployment behaviors of structures with different folding stiffness under varied pressure magnitudes.

4.5 Deployment Dynamics via Ramp Input

In previous Sections, the pressure is applied as a step input, while here we pressurize via a ramp function (Figure 29b). We define t_0 as the time it takes to reach the final pressure magnitude. In this case study, the system is pressurized to $\bar{P}/\bar{P}_0 = 20$ where we had observed the distorted deployment. We vary t_0 such that the pressure is applied with different rates and perform dynamic analysis. When the pressure is applied rapidly, in this case at a rate faster than $t_0 \leq 5$ ms, the high distortion occurs, where the structure snaps and stays at the second stable equilibrium without further deployment as shown in Figure 29d. On the other hand, when we apply the pressure at a lower rate, the structure roughly follows the rigid folding shape with some axial oscillation and settles with little distortion (Figure 29c).

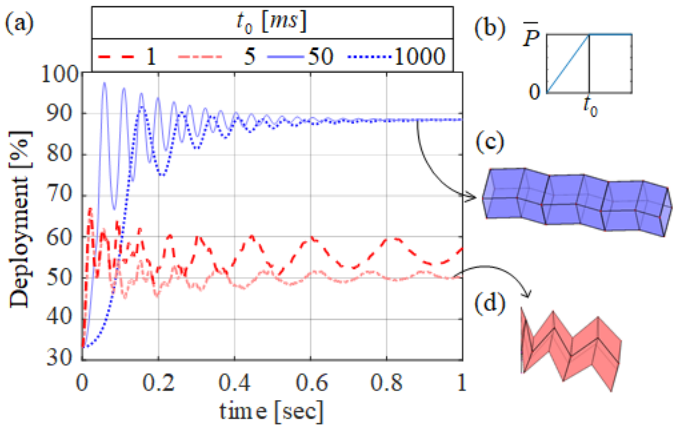

Figure 29. (a) Time history of the dynamic deployment under different rates of pressurization. The stiffness parameters are $\left[\bar{r}_k = 10, \bar{k}_f/\bar{k}_{f0} = 1\right]$. The final value of the pressure magnitude is $\bar{P}/\bar{P}_0 = 20$. (b) We define the pressurization rate by the time t_0. (c-d) The settled configurations of the dynamic deployment under t_0 = 50 and 5 ms, respectively.

Since both the pressurization rate and the ending pressure magnitude can influence the dynamic deployment behaviors, to understand the dynamic deployment under ramp input of the

pressure field, we vary both the ending pressure magnitude and the pressurization rate, as shown in Figure 30. These contourplots (Figure 30 (a, c)) show three types of the dynamic deployment process based on the parameters of the pressure field, the time history of which are in Figure 30d. When the pressurization rate is high enough as in the magenta region, the structure can snap through into the distorted shape (Figure 30f) and then snap back. This deployment behavior is shown by the time history with the blue curve in Figure 30d. Under a certain range of pressurization rate, the structure will snap into the distorted shape and stop without further deployment (Figure 30e). The volumes of the corresponding configurations are shown in Figure 30b. In the lower right triangle as well as the upper left triangle of this parameter space, the volume increases with pressure, while the middle blue region shows discontinuity, which refers to the snap-through region. Figure 30a shows that for a designated ending pressure magnitude, the structure can follow different dynamic deployment paths based on the pressurization rate. Figure 30b shows that there exist relatively constant critical values for the pressurization rate at different ending pressures to achieve different deployment paths. This indicates that we can achieve adaptable deployment behaviors by controlling the pressure rate and pressure field.

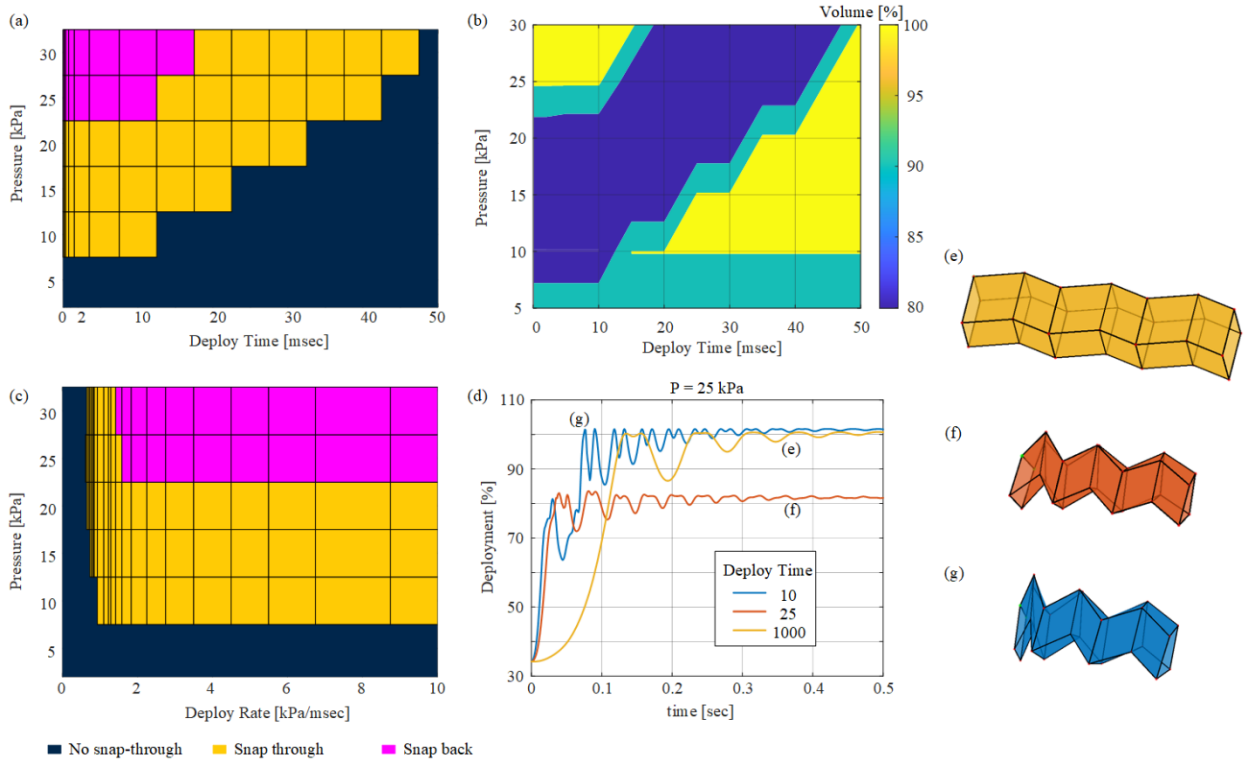

Figure 30. (a, c) The three types of dynamic deployment paths are denoted by three color blocks.. The parameter space is spanned by the ending pressure magnitudes in the y-axis, and the pressurization rate, in the x-axis, is represented by the time to achieve ceratin ending pressure in (a, b) and the pressurization rate in (c). (b) shows the contourplot of the volume of the settled state from the dynamic deployment process. (d) Time history of three typical dynamic deployment paths with pressure magnitude 25 and different deployment times. (e-g) Snapshot of the dynamic configurations during the dynamic deployment process denoted in (d) respectively.

4.6 Conclusion

In Chapter 4, we advance the state of the art by studying the *deployment dynamics* of fluidic origami tubular structures. We uncover new phenomena that have not been observed previously and cannot be derived via traditional quasi-static analysis. It is shown that the fluidic pressure will not only control the final deployed configuration and volume of the tube, but it will also change the effective stiffness and damping ratio of the system, and thus will affect the transient dynamics of the deployment process. It is also discovered that the fluidic origami tube possesses multiple stable equilibria under different pressure levels of the internal fluidic field and could reconfigure among different stable equilibria during dynamic deployment. When

pressurized with a step input or a ramp input with a sufficiently fast rate, for certain pressure amplitudes, the tube could snap into a stable equilibrium with a highly distorted configuration. At lower pressure, the structure cannot overcome the energy barrier to snap through, while at higher pressure the tube experiences snap through and then may snap back to the nominal state near the rigid-folded configuration. The tools and insights developed in this research show the potentials that structural parameter design and pressure rate control can be utilized to achieve smooth and fast deployment, correct for distortions, or reconfigure the structure intentionally to different stable states as desired. These discoveries can be harnessed for potential applications in space booms, morphing surfaces, to soft robotics.

Chapter 5 Deployment Dynamics of Fluidic Origami Multi-Tube Structures

In Chapter 5, we build on the models presented in Chapter 2 and the analysis of the single tube structures from Chapter 4 to investigate the deployment of fluidic Origami multi-tube structures. The problem setup is described in Section 5.1, follows by discussions of findings from the quasi-static (Section 5.2) and dynamic (Section 5.3) analyses, and ends with insights on the effect of the inter-tube interface on the structure deployment characteristics (Section 5.4).

5.1 Deployment Setup

We assume the multi-tube structure initially rests at its folded state and is deployed by increasing the internal pressure, pressurizing either one or both of the tube elements. The pressurized tube element has its two ends sealed off, and the unpressurized tube element can have either sealed or open ends. The deployment extent can be described by both the length of the tube and the internal volume. The length ratio is defined as the ratio of the end-to-end length of the tube over the length of the tube when it is deployed flat. The volume ratio is defined as the ratio of the deformed shape volume over the max volume derived from rigid kinematics. We restrict axial movement on the left end of the tube and release the other end to move freely.

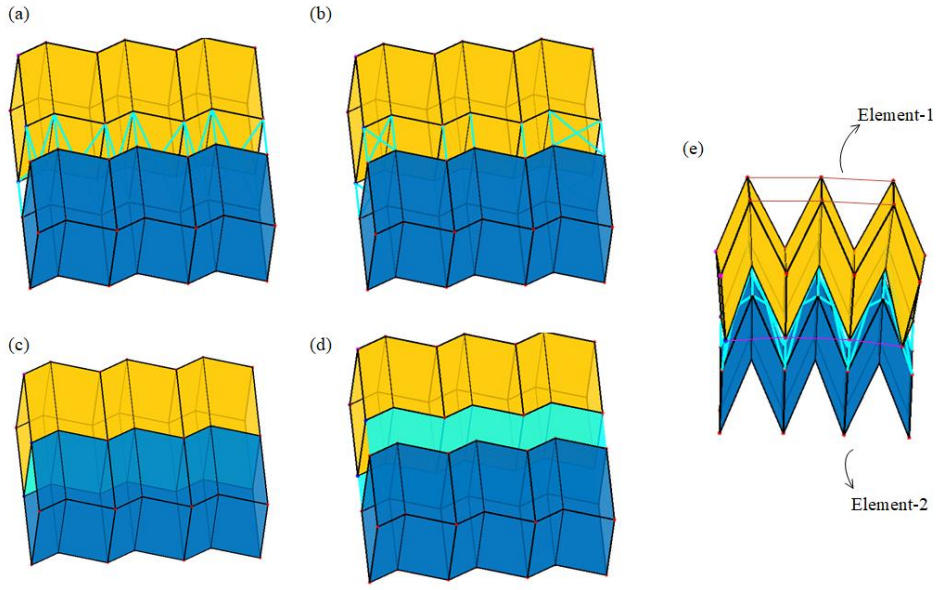

Figure 31. Different types of interface modeling for fluidic origami multi-tube structures, where the two tube elements are in blue and yellow, and the interface is in cyan. (a) Two tube elements are connected by elastic bars through corresponding vertices, which represent a solid material interface. (b) Two tube elements are connected by elastic bars, which allow rigid folding, representing a flexible interface. (c) Two tube elements are connected rigidly, which indicates there will be no displacement at the interface, representing an integrated manufactured multi-tube structure. (d) Two tube elements are connected through flexible facets, which is a variant of the three-element multi-tube structure. The interface can undergo bending and stretching deformation in each facet, and inter-facet folding deformation. (e) The upper tube elemnt in yellow is referred to as element 1 and the lower tube element in blue is referred to as element 2 in the following figures. We use the arch shape to describe the bulge-out configuration, as shown by the deformed state

5.2 Quasi-Static Deployment

We first perform quasi-static deployment analysis on the multi-tube structure under different pressurization methods and boundary constraints. Figure 32 shows the quasi-static deployment process with both elements sealed at two ends, where the internal pressure magnitude of the unpressurized tube element varies with the configuration change according to the ideal gas law.

The overall structure deploys as the pressure in the pressurized tube gradually increases (Figure 32a). The pressurization method can influence the deployment configuration. By comparing the blue and green lines in Figure 32 (a, b), it is shown that the pressurized tube

element will be deployed more than the unpressurized one, which is due to the deformation of the flexible interface in this design. In Figure 32c, the structure can form two different arch shapes under different pressurization methods, the configurations of which are shown in Figure 32 (d, e). We quantify the arch shape by comparing the nodal distances shown in Figure 31e. In the undeformed state, the distances spanned by the red lines and the purple lines maintains the ratio of 4:3. We use the change of the ratio in percentage of the extended tube element to describe the arch shape. The arch shapes in different directions are the two modes according to the eigen analysis on single tube structures. For example, as in the blue lines in each plot of Figure 32, the upper element is fixed on the left end and pressurized, with the lower element unpressurized. During the deployment, the pressurized element will deploy and force the unpressurized element to also deploy. The upper element takes on the arch shape in the positive direction because its lower layer is constrained by the interface and the less-deployed lower element, while the lower element takes on the arch shape in the same direction because its upper layer is driven to expand due to the force balance at the interface and the more-deployed upper element. The difference between the tube elements also grows with the pressure magnitude. Additionally, when the lower tube element is pressurized, the entire structure will acquire a greater deployment extent than when the upper tube element is pressurized, and consequently greater difference between the two elements. Through eigen analysis on the configurations of these two cases at the same overall deployment stage, the former case has a lower natural frequency in the deployment mode than the latter case, which means the structure requires less energy to deploy and arch in the situation where the lower element is fixed and pressurized.

The multi-tube structure deploys the most when both elements are pressurized, and maintains the highest strain energy (Figure 32d). The two tube elements stay at different

deployment stages under the same pressure field, which is because of the asymmetry in origami geometry. The influence from the boundary constraints can be less significant when comparing the yellow and cyan lines in Figure 32. Additionally, Figure 32b shows that the lower tube element deploys more regardless of the boundary constraints, which results in non-negligible arch shapes, where the two elements form arch shapes in the opposite directions.

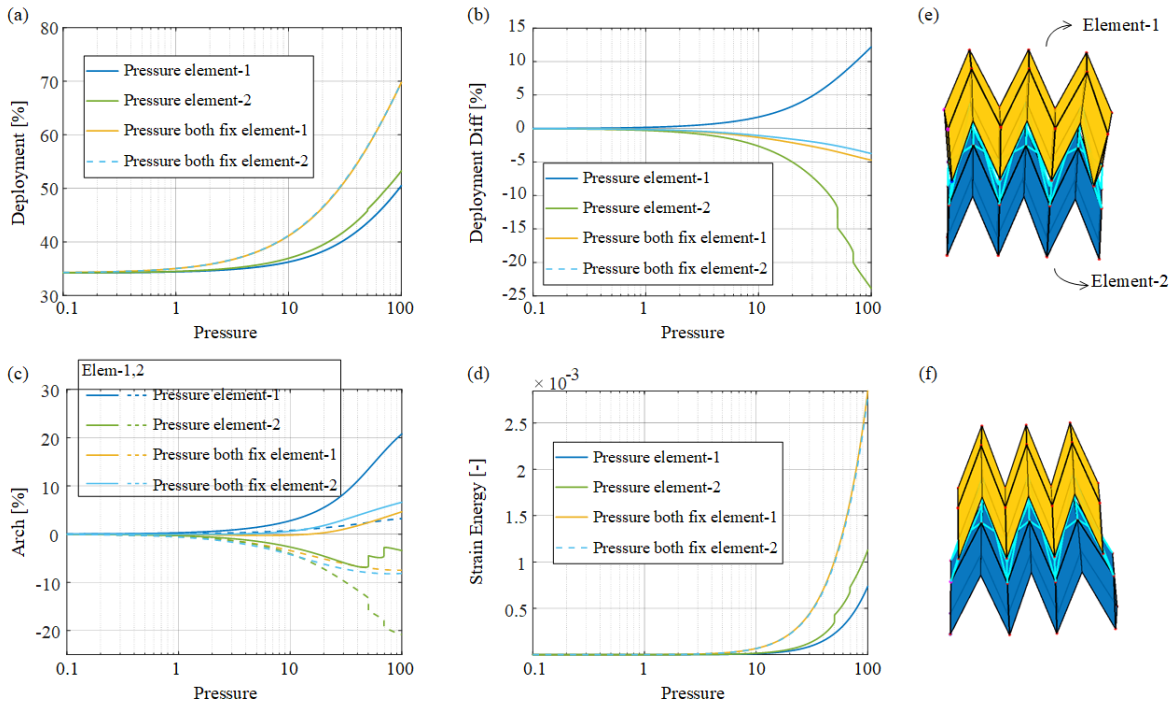

Figure 32. Quasi-static analysis of multi-tube structure with interface modeled by springs. Each line color corresponds to a pressurization method and boundary constraints: blue denotes the case when the upper element in Figure 312e is fixed and pressurized, while the lower element is set free and unpressurized; the green line shows the opposite; with the yellow line, both elements are pressurized, and the upper element while the lower element is fixed with the cyan line. (a) shows the deployment process by the volume of the entire structure. (b) shows the difference in deployment between the two tube elements, with a positive value meaning the upper element is greater in volume. (c) shows the arch shape formed during the deployment due to panel deformation. The positive arch shape is defined as concave up and is shown in (e). In (c), the solid line denotes the upper tube element and the dashed line denotes the lower element. (d) shows the total strain energy in the structure including crease folding, panel stretching and bending, and interface deformation.

We describe the deformation of the multi-tube structure by the average and the difference in strain energy between the two tube elements. In Figure 33, the multi-tube structure is fixed and pressurized at the upper tube element, and the lower element is unpressurized and free to

move. Figure 33a shows that the strain energy increases with the deployment, and the strain energy from the interface is the greatest among all kinds of deformation, which is twice as high as the bending energy even though the stiffness at the interface is only 10% of the panel stiffness. This shows that in the origami multi-tube structure connected by a solid material the interfaces have a significant influence on the overall behavior because it experiences the highest strain energy. From the difference in strain energy between the two tube elements in Figure 33b, the pressurized tube element shows a higher strain energy from pressurization which corresponds with the fact that the pressurized tube element will also be more deployed. The pressurized element also undergoes more tube distortion such as facet bending and stretching. This analysis can provide insight into the deformation behaviors and precision of the system when actuating multi-tube structures.

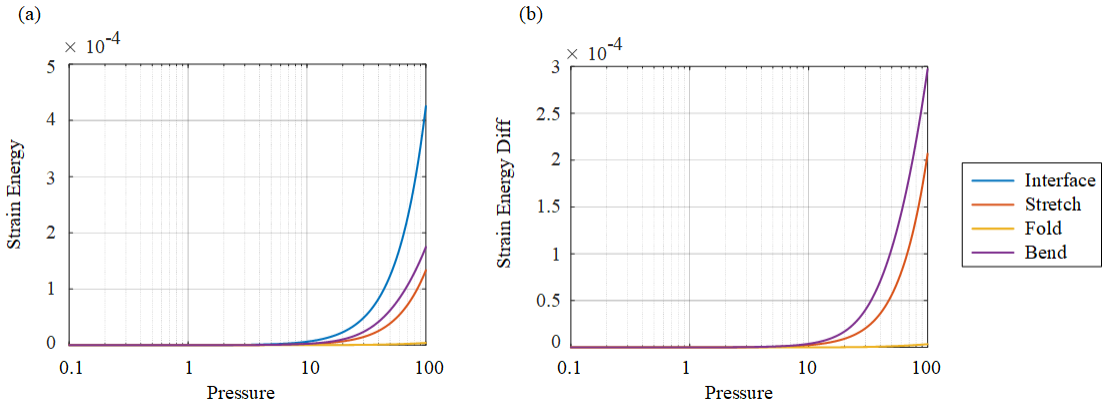

Figure 33. Deformation in the multi-tube structure during quasi-static deployment with the upper element fixed on the left end and pressurized from the left end while the lower element is free and unpressurized. Both tube elements are sealed off on both ends. (a) shows the strain energy from interface deformation and tube deformation including tube crease folding, facet bending, and stretching. (b) shows the difference in the strain energy between the two tube elements. The default positive value means the upper element has greater strain energy than the lower element.

5.3 Dynamic Deployment

We perform dynamic analysis on the deployment of the multi-tube structure under different pressurization methods and boundary conditions. We fix the left end and pressurize the different tube elements, denoted by different line colors in Figure 34 and Figure 35. Similar to the quasi-static deployment, the pressurized tube element is always more deployed than the unpressurized tube. The tube elements take on arch shapes in the same direction, for example, when the upper element is pressurized, the two elements in the structure will form arch shapes in the positive direction, which is due to the constraints from the interface. By comparing the solid and the dotted lines, where the unpressurized tube element is sealed vs. open, the structure deploys more in the latter case. This is because when the two ends of the unpressurized tube are sealed, a pressure field forms that forces this tube element to stay less deployed. This type of negative pressure field results in more significant arch shapes for both pressurization methods because the pressure field together with the interface apply force in the opposite direction to the pressurized tube element, which causes distortion in the tube body and results in higher strain energy as shown by Figure 35(c, d). The greater deployment extent results in higher strain energy at folding creases and the interface deformation (Figure 35(a, b)). By considering the pressurization method and boundary conditions, this analysis can provide insight into the design for desired reconfiguration or deployment performance.

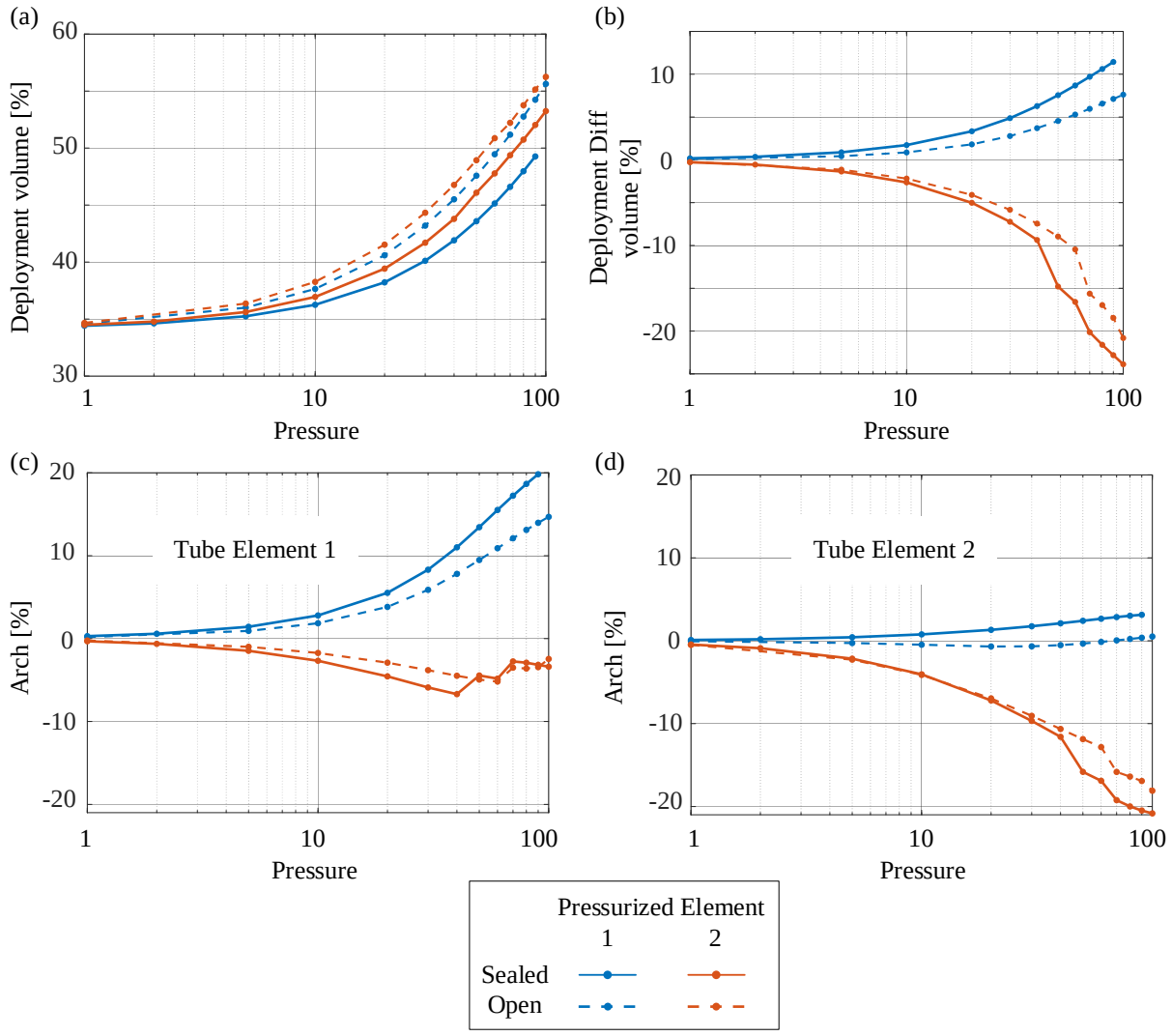

Figure 34. The dynamic deployment of the multi-tube structure. Each point corresponds to a settled configuration from the dynamic deployment simulation. The solid lines refer to the case when the unpressurized tube element is also sealed at the two ends, indicating a varying pressure field with the deployment process. The dotted lines refer to the case when the unpressurized tube element has an open end, meaning that its pressure will not change. In the red lines, the upper element is fixed and pressurized, while in the blue lines the lower element is fixed and pressurized. We use deployment extent as a percentage by volume (a) and the difference in deployment stage in length??????? (b) between the two elements to describe the dynamic deployment process. We also compute the arch shape (c, d) formed in each of the elements respectively to describe the configuration.

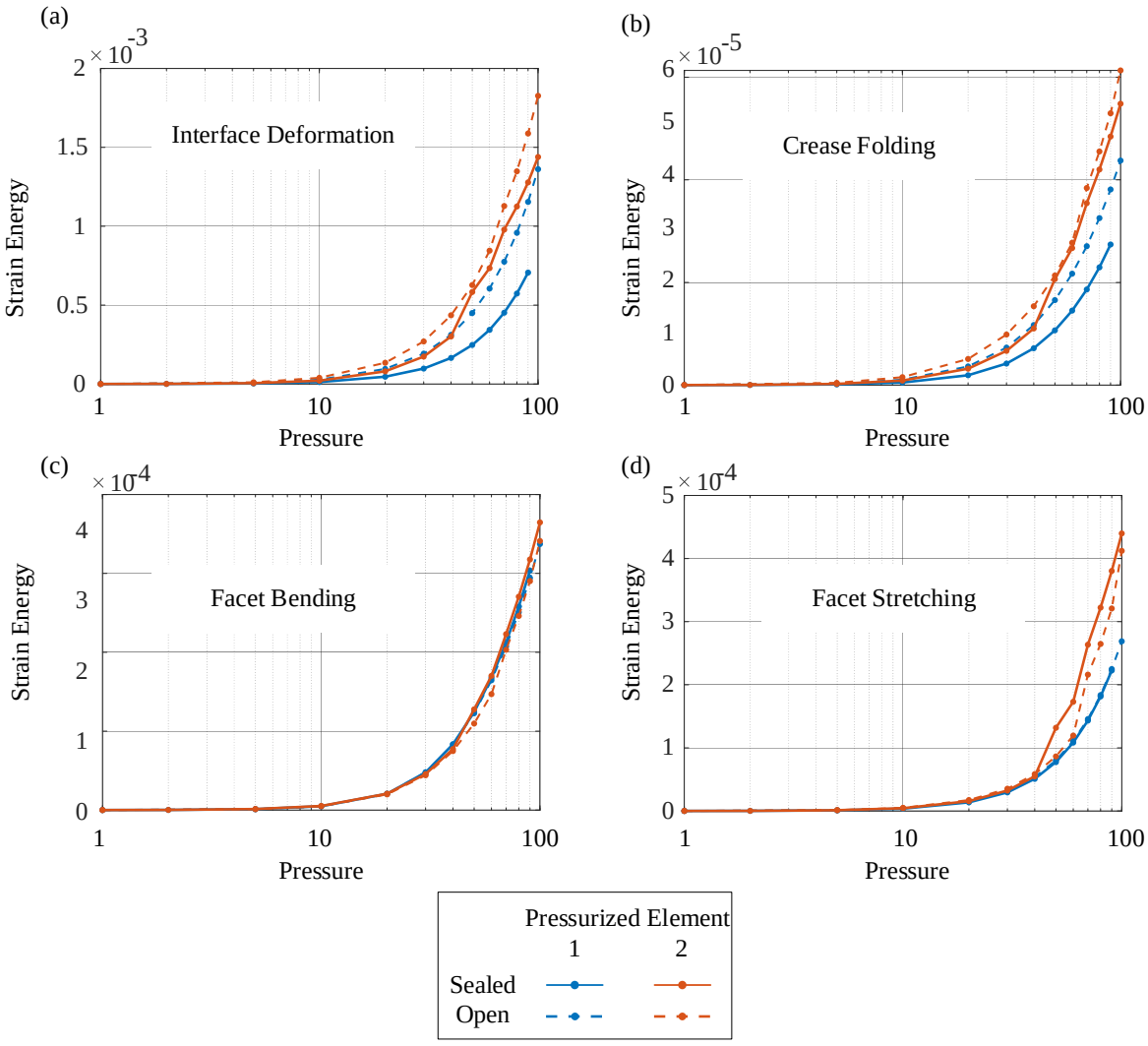

Figure 35. Strain energy from structure deformation at the end of the dynamic deployment process. Each point corresponds to a settled dynamic configuration. The color and line styles are the same as in Figure 34. The strain energy is decomposed into the strain energy from interface deformation (a), tube crease folding deformation (b), tube facet bending (c), and stretching (d) deformation.

5.4 Influence of the Interface

In addition to the pressure field and boundary conditions, the interface design can significantly influence the deployment behavior of a multi-tube structure. In this Section, we perform a parametric study on the interface stiffness and then explore different interface designs.

5.4.1 Influence of Interface Stiffness

Based on previous quasi-static and dynamic deployment analysis on the multi-tube structure (Figure 31a), we vary the interface stiffness to explore how it influences the deployment characteristics. We vary the interface materials such that the ratio of the Young's modulus of the tube body over the interface is [10,50,100].

By decreasing the interface stiffness, the overall structural stiffness decreases, and therefore the overall structure achieves greater deployment under the same pressure magnitude. The structure also deploys more when both elements are pressurized by comparing the group of yellow and blue lines (Figure 36(a, b)). The group of yellow lines shows that when the pressure is high enough, the difference between the tube elements first increases with the deployment, and then decreases because the tube elements reach the deployed state sequentially. The extent of the arch shape also first increases and then decreases with the deployment, because the arch shape is a result of the deployment stage difference.

Similar to Section 5.2, Figure 36(c, d) show that the different directions of the arch shape also apply to structure with different interface stiffness under different pressurization methods. In the case with two elements in the structure where only a single element is pressurized will form an arch shape in the positive direction, while the element in the structure with both elements pressurized will form an arch shape in the negative directions. On the other hand, the extent of the arch shape under different pressurization methods can be influenced by the interface stiffness in different ways. The arch shape is more significant in the pressurized tube element with a stiffer interface as shown by the blue lines in Figure 36c and yellow lines in Figure 36(c, d), while arching becomes less significant in the unpressurized tube element as shown by the blue lines in Figure 36d for deployment stage in the range of [30, 60]. As for the pressurized tube,

when the interface is stiffer there is a larger constraining force, which results in higher arch shape. On the other hand, the unpressurized tube element is under the combined effect of the interface deformation and the negative pressure force from the internal pressure field. At certain deployment stage, the structure has a greater deployment stage difference with respect to the deployment stage on the x axis as shown by the group of green lines in Figure 36e, which share the same tendency as the extent of arch shape depicted by the group of blue lines. This indicates that the arch shape is formed to accommodate the configuration difference between the tube elements.

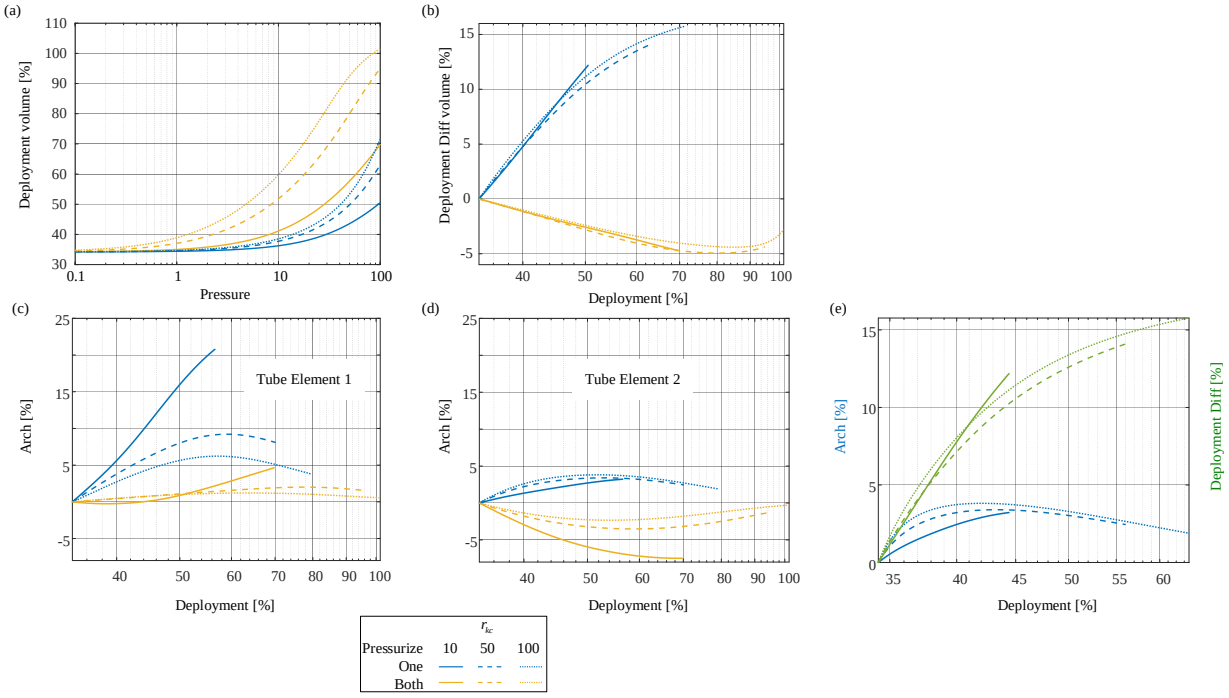

Figure 36. Quasi-static deployment of the multi-tube origami structure (Figure 31a). We vary the interface materials such that the ratio of the Young's modulus of the tube body over the interface is [10,50,100], denoted by different line styles in this figure. This figure also includes two types of pressurization methods under the same boundary condition where the upper tube element is fixed on the left end and both elements are sealed off: the group of blue lines refers to the upper tube element pressurized only, and the group of yellow lines refers to both tube elements pressurized. We use these metrics to describe the deployment: (a) the deployment stage represented by the volume in percentage; (b) the difference in deployment stage between the two tube elements with respect to the overall (average) deployment length in the x-axis; the arch shape formed in the upper tube element (c) and lower tube element (d) with respect to the deployment stage of the pressurized tube element in the x-axis. We relate the arch shape in the unpressurized tube element with the deployment stage difference in (e) and is plotted against the deployment stage of the unpressurized tube element in the x-axis.

Figure 37 shows the strain energy generated from structural deformation. The total strain energy (Figure 37a), the strain energy from interface deformation (Figure 37b), tube deformation including tube facet bending (Figure 37e) and stretching deformation (Figure 37f), increase with a stiffer interface. The strain energy within hinges at fold creases, decreases with a stiffer interface, which is because of the tube elements deploy less with stiffer interfaces. Figure 37c shows the energy difference between tube elements. The group of blue lines shows that the pressurized tube element has more strain energy than the unpressurized one. The higher strain energy is because the two elements have the same stiffness, yet the pressurized element deforms more, which agrees with the configurations described in Figure 36.

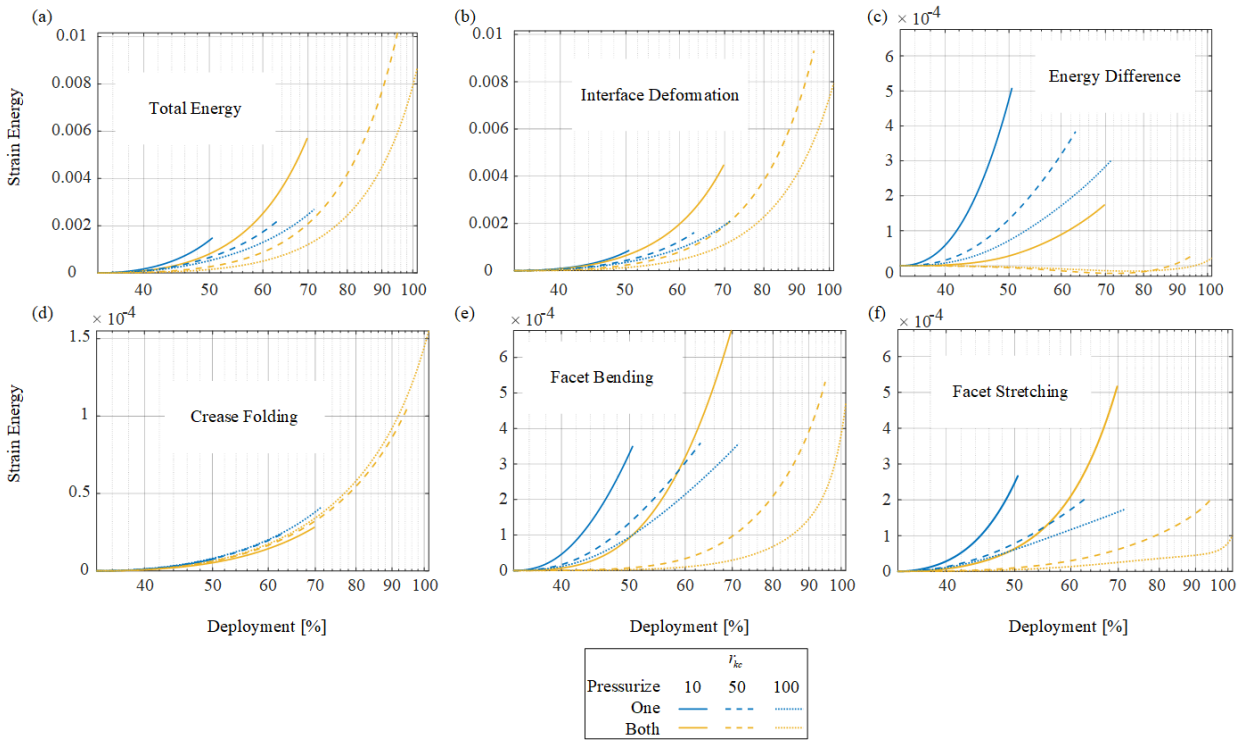

Figure 37. Strain energy from deformation during quasi-static deployment. The deployment setup is the same as in Figure 36. The energy distribution is described by the total energy of the entire structure (a); the energy from interface deformation (b), the difference of strain energy between the two tube elements (c); crease folding deformation (d), tube facet bending (e), and tube facet stretching deformation (f).

We also perform dynamic analysis on the deployment process of structure with different interface stiffness, as shown in Figure 38. The dynamic result denoted by points is compared with the quasi-static results denoted by lines. Similar to results from Section 5.2 and Section 5.3, the structure deploys more when the lower tube element is pressurized rather than the upper tube element. The multi-tube structure with a softer interface gains greater deployment, while the overall behaviors are qualitatively the same. It is shown that the points all fall on the corresponding lines, indicating that under this type of interface design, the structure will stay at a single stable equilibrium, and will not undergo snap-through during the dynamic process even when the material of the interface becomes flexible. The consistency between the dynamic and quasi-static analyses also indicates that the models developed in this research are valid for both dynamic and quasi-static analyses.

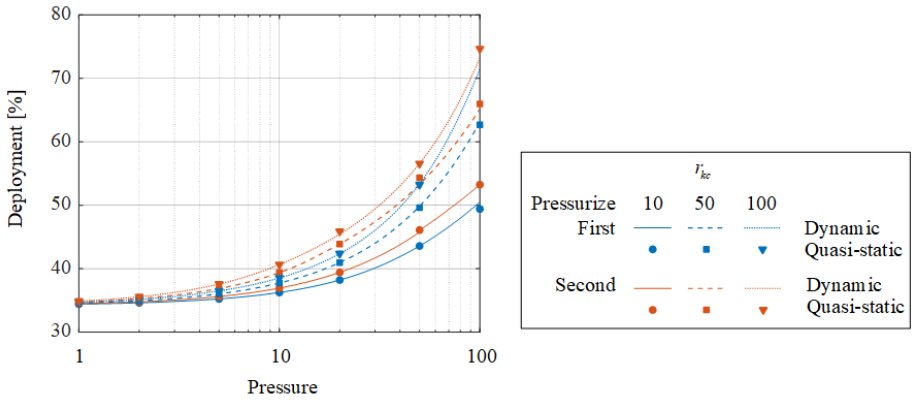

Figure 38. The comparison between the configuration from quasi-static deployment analysis shown by the lines, and that from the settled state in the dynamic deployment process denoted by points. Lines and points in different colors represent different pressurization methods, where blue refers to the upper tube element being fixed and pressurized, and red refers to the lower tube element being fixed and pressurized. Lines in different styles represent different interface stiffness ratios, denoted by solid, dashed, and dotted lines. Points in different shapes also represent different interface stiffness ratios, denoted by circular, rectangular, and diamond shapes.

5.4.2 Influence of Interface Design

In this Section, we explore different interface designs as shown in Figure 31. In the first design (Figure 31a), we use elastic bars to link the tube elements at the hinges. The bars placed in the diagonals restrict the relative displacement between the corresponding panels, which can also represent a solid material for connection. We change the bar arrangement in the second design (Figure 31b) such that the interface allows one degree of freedom in the multi-tube structure and represents connecting the two tube elements through hinges. The third design (Figure 31c) represents a rigid connection that does not allow displacement variations between the two connecting layers, while still allowing for the rigid folding and deployment motions. The fourth interface design (Figure 31d) adopts the flexible origami panels placed between the two tube elements, which can have varied widths showing the distance between the tube elements. This design allows for rigid folding and deployment motions with flexible panels as the connection. This design can also refer to an interleaved origami tubular structure.

Figure 39 shows the dynamic deployment of the tubes with different interfaces, different pressure magnitudes, and different pressurization methods. In the low-pressure region [0, 10], the difference between pressurization methods is negligible. In the high-pressure region, the structure in the first design (Figure 31a) follows the same branch of the stable equilibrium while the three other designs (Figure 31 (b-d)) undergo snap-through into other branches of the stable equilibrium as shown in Figure 39a, which corresponds to high strain energy levels (Figure 39b). The configurations of the tube element at the highly distorted stable equilibrium (Figure 39(c-e)) have been discussed in detail in the single tube analysis in Section 4.4. The tube element in Figure 39f corresponds to an eigenmode of the single tube structure. These results indicates that the analysis on the single tube can be useful for the multi-tube structure.

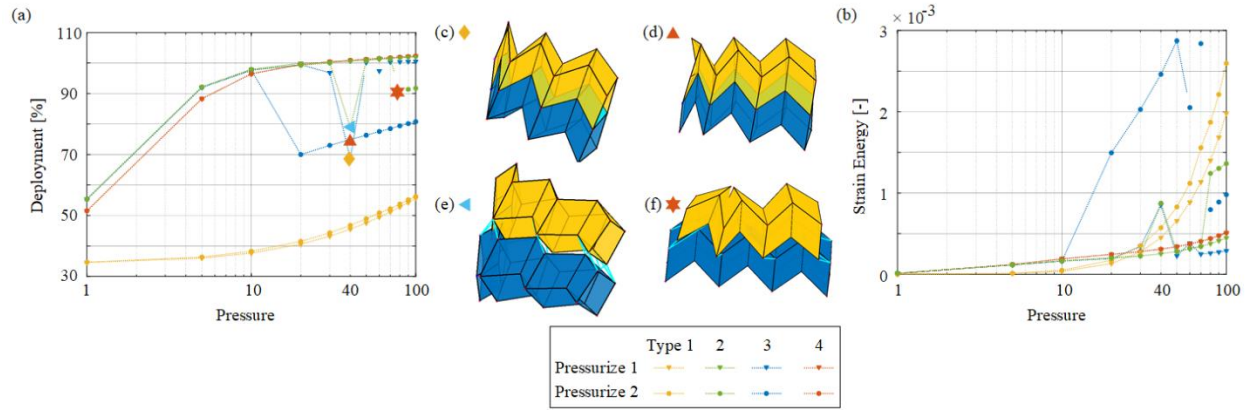

Figure 39. The dynamic deployment of multi-tube structures with different interface designs listed in Figure 31. The line colors refer to different interface designs, and the point shapes represent different pressurization methods. Pressurize 1 means the upper tube element is fixed and pressurized, and pressurize 2 means the lower tube element is fixed and pressurized. (a) shows the settled configuration of each dynamic deployment process, and the corresponding strain energy at that configuration is shown in (b). (d-f) shows the snapshot of the configuration denoted by different points in (a).

5.5 Conclusion

In Chapter 5, we advance the state of the art through studying the *deployment dynamics* of fluidic origami multi-tube structures. We adopt four different interface designs and perform quasi-static and dynamic analyses to understand the effect of structural properties and to explore the dynamic deployment behaviors. It is discovered that the multi-tube structure can process more complex behaviors than the single tube structure such as the arch shapes. It is shown that the tube element can take on different configurations, and such differences vary with the internal pressure field and the inter-tube interface stiffness. The pressurization method and boundary conditions can influence the deployment significantly. By pressurizing different tube elements, the multi-tube structure can achieve different deployment extent and arch shapes in positive and negative directions as shown in Figure 32(e, f). Depending on whether the unpressurized tube element is sealed, the overall deployment extent and the extent of arch shape could be very different. Furthermore, it is discovered that with the same material stiffness of the interface, the

multi-tube structure with certain interface designs possesses multiple stable equilibria and could reconfigure among different stable equilibria during dynamic deployment. The tools and insights developed in this research show the potential that the structural design and pressure field control can be utilized to achieve reconfigurations of the structure as desired. The work presented in this chapter can serve as a foundation for future research on even more complex structural architecture of integrating multiple tubes with different orientations and pressurization schemes.

Chapter 6 Conclusions and Future Directions

In this concluding Chapter, we summarize the scholarly contributions and broader impact of this thesis research, follow by a discussion of the possible future research directions.

6.1 Scholarly Contributions

Origami has great potential for creating deployable, reconfigurable, and functional structures. However, it is crucial to understand the dynamic characteristics of origami to achieve desired system performance. This dissertation investigates the deployment of origami structures, including Miura origami sheets, fluidic origami tubes, and fluidic origami multi-tube structures. We develop a dynamic model by considering panel inertia and compliance, where we discretize the structure by using equivalent lump mass elements. We also create a discretized force system to represent the internal pressure field in origami tubes. We derive the nondimensionalized equations of motion and perform analysis to gain insight on the system dynamic behaviors during deployment. We perform quasi-static and dynamic analysis on the deployment process of the origami sheet and tube structures to understand the effects of various system parameters and inputs on the overall dynamic deployment performance. We uncover new phenomena and qualitative features that have not been observed previously and cannot be derived via traditional quasi-static and rigid kinematic unfolding analyses.

In Chapter 3, we investigate the deployment dynamics of Miura origami sheets. Results show that structural stiffness can influence the dynamic deployment behaviors qualitatively, as compared to rigid kinematics analysis. For origami sheets built by panels with finite compliance,

pop-ups can occur at different stages depending on the stiffness ratio between panel bending stiffness and crease folding stiffness $\bar{r}_k$. There also exists a critical value for the stiffness ratio. $\bar{r}_{km}$, below which the structure would undergo large pop-up motion. Apart from the material stiffness parameters, the pattern geometry can influence the effective structural stiffness properties, and thus affect the transient dynamics of the deployment process. It is discovered that the origami sheet possesses multiple stable equilibria under different geometric parameters and may reconfigure between the stable equilibria during dynamic deployment. We also study the inertia effect by changing the controlled deployment rate, and uncover the potential of tunable deployment behavior by utilizing deployment control.

In Chapter 4, we study the dynamics of deployment of Miura origami tubes under fluidic actuation. Results in the quasi-static analysis show that the folding stiffness plays a more significant role than the panel bending stiffness in deployment process. Eigen analysis also shows that both the folding stiffness and the internal pressure field can influence the structural properties, which indicates the possibility to design the structure and pressure to achieve a desired dynamic deployment path. It is discovered that the structure maintains different stable equilibria over a wide range of pressure magnitudes. Dynamic simulations show that the structure can undergo snap-through under certain pressure magnitudes and pressurization rates, which means that the structure can achieve desired reconfiguration by proper design and tuning of the internal pressure field.

In Chapter 5, we extend our knowledge on fluidic origami tubes by investigating fluidic origami multi-tube structures. It is shown that the multi-tube structure can have more complex behaviors than the single tube structure, where the tube elements can take on different configurations. The multi-tube structure can achieve different deployment extents and arch

shapes based on the pressurization method and boundary conditions. Whether or not the unpressurized tube element is sealed can influence the overall deployment extent and the amount of distortion. By analyzing different designs of the interface, it is discovered that with the same material stiffness, certain interface designs can lead to snap-through between different stable equilibria during dynamic deployment, which enriches the reconfiguration behaviors of the fluidic origami tubular structures.

The modeling, analysis and design tools developed for the origami platform in this research will enable the dynamic analysis of origami structures considering material compliance and inertia effects. These observations are original and these phenomena have not and cannot be derived using traditional approaches, which enables a deeper understanding of the physics behind the Origami deployment dynamics. The tools and outcomes developed from this research will contribute to the scholarly literature and advance the field of origami engineering.

6.2 Broader Impact

The concept of origami has been adopted in many applications, such as space structures, civil structures, robotics, and medical devices. Origami is often chosen as it enables deployment and reconfiguration, while it can also expand the geometric and physical functionality of the system. Because the deployment process is an inherently dynamic process, and certain deployment performance such as fast and smooth deployment are desired, the tool to investigate the dynamic behaviors becomes necessary. In practice, there are circumstances under which the deployment dynamics need to be considered, for example, when fast reconfiguration is desired, or when the origami sheet is flexible due to soft material or low thickness. In this work, we for the first time proposed a dynamic model considering panel inertia and flexibility to analyze the dynamic deployment process, while most of the past attention has been on only the kinematic or

the quasi-static process. More importantly, our research is not limited to any specific origami or dynamic cases. While the Miura origami pattern and tubes are discussed in this work, the tools that we proposed can be generalized to other origami patterns, and our analysis can lay the foundation for future research.

Another valuable contribution of this work is that it provides insights to design structures for applications and operations outside our current practice. For example, from our analyses, we have shown dynamic responses of the origami during deployment that have not and cannot be observed in traditional quasi-static and kinematic analyses, even qualitatively, like the pop-up phenomenon in origami sheets, the snap-through behaviors between the stable equilibria of fluidic origami tubes, and the arch shapes in different directions in the multi-tube structure. Therefore, the tools we developed and the outcomes are valuable in raising awareness and helping the community to design future origamis that can deploy successfully with design and operating conditions that are outside the traditional range of consideration in the past. In other words, this work is impactful in extending our fundamental knowledge and comfort zone.

6.3 Future Directions

6.3.1 Dynamics of Single Fluidic Origami Tube Harnessing Fluidic Field Pressure Design

In Section 4.5, we have shown that the dynamic deployment behaviors of fluidic origami tubes can be controlled by changing the rate and level of pressurization. Based on these observations, one future direction is to understand such system dynamics with deeper insight and develop methods to design the pressure profile such that the fluidic origami dynamic reconfiguration process would follow a certain path and converge to a desired final configuration. For example, researchers can design the input fluidic pressure function such that the structure will avoid the highly distorted configuration (such as the second stable equilibrium

observed in this thesis study) and achieve smooth deployment and folding, or they may design the structural parameters and the input pressure function to reconfigure the structure so that it converges to and stays at the second stable equilibrium by design.

In addition to deployment, it also shows that we can design the pressure profile such that the structure can follow a certain path and fold into the certain configuration, as in Figure 40. Similar to the dynamic deployment process, by removing the internal pressure field with different rates, the structure can either fold to the rest configuration (Figure 40d) or snap into another stable equilibrium (Figure 40c). The outcomes of the dynamic folding analysis can enrich the profound reconfigurations of fluidic origami, and be useful for applications requiring contraction such as recycling of structures.

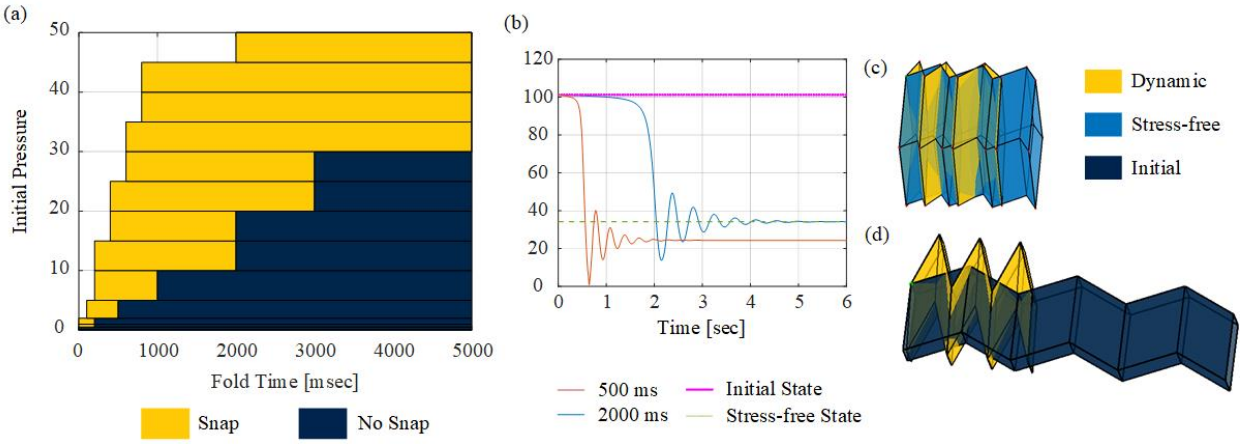

Figure 40. Dynamic folding of fluidic origami tubes via ramp function for releasing the internal pressure. (a) shows whether a structure will snap or not for different pressures and pressurization rates. (b) shows the time history of the structure folding from the same configuration (stable equilibrium under $P = 20$ kPa) while under different rates with which the pressure field is removed. (c) shows the comparison between the settled dynamic configuration from the red path in (b) and the rest configuration. (d) shows the comparison between the settled dynamic configuration from the blue path in (b) and the initial pressurized and deployed configuration.

6.3.2 Deployment Dynamics of Interconnected Fluidic Origami Tubes with Complex Geometries

It is shown that we can achieve programmable kinematics and stiffness by changing the geometry of the cross-section and folds[90] of the origami tubes, and multiple origami tubes can be integrated and interconnected in a variety of ways and exhibit tunable stiffness[91]. Building upon these previous efforts[90,91] and our studies discussed in Chapter 4 and Chapter 5, it is worthwhile to explore the deployment dynamics of interconnected fluidic origami tubes and origami tubes with various cross-sections. For the interconnected fluidic origami tube, based on the developed model and the results from the quasi-static and dynamic analysis in Chapter 5, researchers can design the structural properties and the pressure field to achieve the deployment dynamics beyond what can be achieved with the single fluidic origami tube structure discussed in Chapter 4. For example, they may advance the structure's adaptivity and versatility by designing the geometric and stiffness parameters for both the tube body and the interface. For tubular origami with specially designed cross-sections, the fluidic pressurization may be designed to achieve deployment dynamics with more sophisticated transient behaviors and configurations in bending, twisting, and shear.

6.3.3 Validation with Physical Model Experiment

In this thesis, we have used paper and 3D printed prototypes to shown that the origami structure can possess multiple stable equilibria. However, most of the conclusions on origami dynamics we draw are from numerical studies. For example, the influence of stiffness and inertia on the Miura sheet deployment dynamics, or the influence of pressure inside the tubular structures are only observed through simulations. Therefore, one future direction is to design and manufacture different prototypes and perform experiments to validate the numerical analysis

findings we concluded in analyzing the Origami sheet, fluidic-tube, and multi-fluidic tube configurations, in terms of their deployment dynamic characteristics.

Bibliography

[1] Shah, S. I. H. and Lim, S., “Transformation from a single antenna to a series array using push/pull origami,” Sensors (Switzerland) 17(9) (2017).

[2] Ahmed, S., Kamel, A. and Mahmoud, W., “Methodology for Using Origami in Designing Deployable Shelters,” J. Des. Sci. Appl. Arts 1(2), 20–37 (2020).

[3] Li, S. and Wang, K. W., “Fluidic origami: A plant-inspired adaptive structure with shape morphing and stiffness tuning,” Smart Mater. Struct. 24(10), 105031 (2015).

[4] Miyashita, S., Guitron, S., Li, S. and Rus, D., “Robotic metamorphosis by origami exoskeletons,” Sci. Robot. 2(10), 1–7 (2017).

[5] Kuribayashi, K., Tsuchiya, K., You, Z., Tomus, D., Umemoto, M., Ito, T., Sasaki, M., “Self-deployable origami stent grafts as a biomedical application of Ni-rich TiNi shape memory alloy foil”, Materials Science and Engineering: A, Volume 419, Issues 1–2, 2006, Pages 131-137, ISSN 0921-5093, https://doi.org/10.1016/j.msea.2005.12.016.

[6] Gabler, F., Karnaushenko, D. D., Karnaushenko, D. and Schmidt, O. G., “Magnetic origami creates high performance micro devices,” Nat. Commun. 10(1) (2019).

[7] Zhu, Y., Birla, M., Oldham, K. R. and Filipov, E. T., “Elastically and Plastically Foldable Electrothermal Micro-Origami for Controllable and Rapid Shape Morphing,” Adv. Funct. Mater. 30(40), 1–10 (2020).

[8] Novelino, L.S., Ze, Q., Wu, S., Paulino, G.H., and Zhao, R., “Untethered control of functional origami microrobots with distributed actuation”, Proceedings of the National Academy of Sciences, volume 117, 39, 24096-24101, 2020, doi 10.1073/pnas.2013292117

[9] Miura, K., “Method of packaging and deployment of large membranes in space,” Inst. Sp. Astronaut. Sci. Rep. 618, 1–9 (1985).

[10] Overvelde, J. T. B., De Jong, T. A., Shevchenko, Y., Becerra, S. A., Whitesides, G. M., Weaver, J. C., Hoberman, C. and Bertoldi, K., “A three-dimensional actuated origami-inspired transformable metamaterial with multiple degrees of freedom,” Nat. Commun. 7, 1–8 (2016).

[11] Xu, Q., Gu, L., Liu, Z., Zhang, L., Yuan, J., Lu, C., Lei, K., Du, Z., “Design, preparation and characterization of three-dimensional auxetic warp and weft backed weave fabrics based on origami tessellation structures”, Textile Research Journal. April 2022. doi:10.1177/00405175221094044

[12] Fang, H., Li, S., Ji, H. and Wang, K. W., “Uncovering the deformation mechanisms of origami metamaterials by introducing generic degree-four vertices,” Phys. Rev. E 94(4), 1–11 (2016).

[13] Fang, H., Li, S. and Wang, K. W., “Self-locking degree-4 vertex origami structures,” Proc. R. Soc. A Math. Phys. Eng. Sci. 472(2195), 20160682 (2016).
[14] Filipov, E. T., Tachi, T., Paulino, G. H. and Weitz, D. A., “Origami tubes assembled into stiff, yet reconfigurable structures and metamaterials.,” Proc. Natl. Acad. Sci. U. S. A. 112(40), 12321–12326 (2015).
[15] Li, S. and Wang, K. W., “Fluidic origami with embedded pressure dependent multi-stability: A plant inspired innovation,” J. R. Soc. Interface 12(111), 20150639 (2015).
[16] Li, S., Fang, H. and Wang, K. W., “Recoverable and Programmable Collapse from Folding Pressurized Origami Cellular Solids,” Phys. Rev. Lett. 117(11), 1–5 (2016).
[17] Ma, J., Song, J. and Chen, Y., “An origami-inspired structure with graded stiffness,” Int. J. Mech. Sci. 136(December 2017), 134–142 (2018).
[18] Woodruff, S.R., Filipov, E.T. “Curved creases redistribute global bending stiffness in corrugations: theory and experimentation”, Meccanica 56, 1613–1634 (2021). https://doi.org/10.1007/s11012-020-01200-7
[19] Sadeghi, S., Allison, S. R., Bestill1 B., and Li, S., “TMP origami jumping mechanism with nonlinear stiffness”, 2021 Smart Mater. Struct. 30 065002
[20] Gao, J., You, Z., “Origami-inspired Miura-ori honeycombs with a self-locking property”, Thin-Walled Structures, Volume 171, 2022, 108806, ISSN 0263-8231, https://doi.org/10.1016/j.tws.2021.108806.
[21] Filipov, E. T., Paulino, G.H., Tachi, T., “Deployable Sandwich Surfaces with High Out-of-Plane Stiffness”, 2019, Journal of Structural Engineering, 04018244, 145, 2, doi:10.1061/(ASCE)ST.1943-541X.0002240
[22] Waitukaitis, S., Menaut, R. R., Chen, B. G. G., Van Hecke, M. and Hecke, M. Van., “Origami multistability: From single vertices to metasheets,” Phys. Rev. Lett. 114(5), 2–6 (2015).
[23] Fang, H., Wang, K. W. and Li, S., “Asymmetric Energy Barrier and Static Mechanical Diode Effect from Folding,” 1–25 (2017).
[24] Sengupta, S. and Li, S., “Harnessing the anisotropic multistability of stacked-origami mechanical metamaterials for effective modulus programming,” J. Intell. Mater. Syst. Struct. 29(14), 2933–2945 (2018).
[25] Hanna, B. H., Lund, J. M., Lang, R. J., Magleby, S. P. and Howell, L. L., “Waterbomb base: A symmetric single-vertex bistable origami mechanism,” Smart Mater. Struct. 23(9) (2014).
[26] Filipov, E.T., Redoutey, M., “Mechanical characteristics of the bistable origami hypar”, Extreme Mechanics Letters, Volume 25, 2018, Pages 16-26, ISSN 2352-4316, https://doi.org/10.1016/j.eml.2018.10.001.
[27] Sadeghi, S., Li, S., “Dynamic folding of origami by exploiting asymmetric bi-stability”, Extreme Mechanics Letters, Volume 40, 2020, 100958, ISSN 2352-4316, https://doi.org/10.1016/j.eml.2020.100958.

[28] Kaufmann, J., Bhovad, P., and Li, S., “Harnessing the Multistability of Kresling Origami for Reconfigurable Articulation in Soft Robotic Arms”, Soft Robotics, 9,2, 212-223, 2022, doi 10.1089/soro.2020.0075.

[29] Tao, J., and Li, S. "A Study of the Multi-Stability in a Non-Rigid Stacked Miura-Origami Cellular Mechanism." Proceedings of the ASME 2021 International Design Engineering Technical Conferences and Computers and Information in Engineering Conference. Volume 8B: 45th Mechanisms and Robotics Conference (MR). Virtual, August 17–19, 2021. V08BT08A033. ASME.

[30] Liu, K., Tachi, T., and Paulino, G.H. “Invariant and smooth limit of discrete geometry folded from bistable origami leading to multistable metasurfaces”, Nat Commun 10, 4238 (2019). https://doi.org/10.1038/s41467-019-11935-x

[31] Liu, K., Kosednar, M., Tachi, T., and Paulino, GH, "Integrated Origami-String System", Proceedings of the ASME 2019 International Design Engineering Technical Conferences and Computers and Information in Engineering Conference. Volume 5B: 43rd Mechanisms and Robotics Conference. Anaheim, California, USA. August 18–21, 2019. V05BT07A033. ASME. https://doi.org/10.1115/DETC2019-97486

[32] Li, S., Fang, H., Sadeghi, S., Bhovad, P., Wang, K.W., “Architected Origami Materials: How Folding Creates Sophisticated Mechanical Properties”, Adv. Mater. 2019, 31, 1805282.https://doi.org/10.1002/adma.201805282

[33] Yu, Y., Hong, T.K., Economou, A., Paulino, G.H., “Rethinking Origami: A Generative Specification of Origami Patterns with Shape Grammars”, Computer-Aided Design, Volume 137, 2021, 103029, ISSN 0010-4485, https://doi.org/10.1016/j.cad.2021.103029.

[34] Yang, F., Zhang, M., Ma, J., You, Z., Yu, Y., Chen, Y., Paulino, G.H., “Design of Single Degree-of-Freedom Triangular Resch Patterns with Thick-panel Origami”, Mechanism and Machine Theory, Volume 169, 2022, 104650, ISSN 0094-114X, https://doi.org/10.1016/j.mechmachtheory.2021.104650.

[35] Zhu, Y and Filipov, E.T., “Harnessing Interpretable Machine Learning for Origami Feature Design and Pattern Selection”, arXiv, 2022, doi 10.48550/ARXIV.2204.07235.

[36] Yang, J., Zhang, X., Chen, Y., and You. Z., “Folding arrays of uniform-thickness panels to compact bundles with a single degree of freedom”, Proc. R. Soc. A.4782022004320220043, 2022, http://doi.org/10.1098/rspa.2022.0043

[37] Lin, W., Yang, F., Zhang, J., “A twofold-symmetric kirigami pattern and its mobile tessellations”, Mechanism and Machine Theory, Volume 174, 2022, 104916, ISSN 0094-114X, https://doi.org/10.1016/j.mechmachtheory.2022.104916.

[38] Wang, H., Zhao, D., Jin, Y., Wang, M., Mukhopadhyay, T., You, Z., “Modulation of multi-directional auxeticity in hybrid origami metamaterials”, Applied Materials Today, Volume 20,2020,100715,ISSN 2352-9407,https://doi.org/10.1016/j.apmt.2020.100715.

[39] Misseroni, D., Pratapa, P., Liu, K., Paulino, G.H., “Experimental realization of tunable Poisson’s ratio in deployable origami metamaterials”, Extreme Mechanics Letters, Volume 53, 2022, 101685, ISSN 2352-4316, https://doi.org/10.1016/j.eml.2022.101685.

[40] Pratapa, P., Liu, K., and Paulino, G.H., “Geometric Mechanics of Origami Patterns Exhibiting Poisson’s Ratio Switch by Breaking Mountain and Valley Assignment”, Phys. Rev. Lett. 122, 155501 – Published 19 April 2019, DOI: https://doi.org/10.1103/PhysRevLett.122.155501

[41] Mukhopadhyay, T., Ma, J., Feng, H., Hou, D., Gattas, J.M., Chen, Y., You, Z., “Programmable stiffness and shape modulation in origami materials: Emergence of a distant actuation feature”, Applied Materials Today, Volume 19, 2020, 100537, ISSN 2352-9407, https://doi.org/10.1016/j.apmt.2019.100537.

[42] Li, Z., Yu, C., Qi, L., Xing, S., Shi, Y., and Gao, C., 2022. "Mechanical Behaviors of the Origami-Inspired Horseshoe-Shaped Solar Arrays" Micromachines 13, no. 5: 732. https://doi.org/10.3390/mi13050732

[43] Pratapa, P., Liu, K., Vasudevan, S. P., and Paulino, G. H. (March 12, 2021). "Reprogrammable Kinematic Branches in Tessellated Origami Structures." ASME. J. Mechanisms Robotics. June 2021; 13(3): 031004. https://doi.org/10.1115/1.4049949

[44] Huang, L., Zeng, P., Yin, L., Liu, B., Yang, Y., Huang, J., “Design and kinematic analysis of a rigid-origami-based underwater sampler with deploying-encircling motion”, Mechanism and Machine Theory, Volume 174, 2022, 104886, ISSN 0094-114X, https://doi.org/10.1016/j.mechmachtheory.2022.104886.

[45] Thota, M. and Wang, K. W., “Reconfigurable origami sonic barriers with tunable bandgaps for traffic noise mitigation,” J. Appl. Phys. 122(15) (2017).

[46] Thota, M., Li, S. and Wang, K. W., “Lattice reconfiguration and phononic band-gap adaptation via origami folding,” Phys. Rev. B 95(6), 1–10 (2017).

[47] Pratapa, P., Suryanarayana, P., Paulino, G.H., “Bloch wave framework for structures with nonlocal interactions: Application to the design of origami acoustic metamaterials”, Journal of the Mechanics and Physics of Solids, Volume 118, 2018, Pages 115-132, ISSN 0022-5096, https://doi.org/10.1016/j.jmps.2018.05.012.

[48] Waal, L., Lu, G., Zhang, J., You, Z., “Dynamic behaviour of graded origami honeycomb”, International Journal of Impact Engineering, Volume 157, 2021, 103976, ISSN 0734-743X, https://doi.org/10.1016/j.ijimpeng.2021.103976.

[49] Wo, Z., Raneses, J. M., and Filipov, E. T. (May 2, 2022). "Locking Zipper-Coupled Origami Tubes for Deployable Energy Absorption." ASME. J. Mechanisms Robotics. August 2022; 14(4): 041007. https://doi.org/10.1115/1.4054363

[50] Wang, H., Zhao, D., Jin, Y., Wang, M, You, Z., Yu, G., “Study of collapsed deformation and energy absorption of polymeric origami-based tubes with viscoelasticity”, Thin-Walled Structures, Volume 144, 2019, 106246, ISSN 0263-8231, https://doi.org/10.1016/j.tws.2019.106246.

[51] Xiang, X., Lu, G., You, Z., “Energy absorption of origami inspired structures and materials”, Thin-Walled Structures, Volume 157, 2020, 107130, ISSN 0263-8231, https://doi.org/10.1016/j.tws.2020.107130.
[52] Li, Q., Zhi, X., Fan, F., “Dynamic crushing of uniform and functionally graded origami-inspired cellular structure fabricated by SLM”, Engineering Structures, Volume 262, 2022, 114327, ISSN 0141-0296, https://doi.org/10.1016/j.engstruct.2022.114327.
[53] Yasuda, H., Chong, C., Charalampidis, E. G., Kevrekidis, P. G., and Yang, J., “Formation of rarefaction waves in origami-based metamaterials,” Phys. Rev. E 93(4), 1–11 (2016).
[54] Liu, S., Lu, G., Chen, Y. and Leong, Y. W., “Deformation of the Miura-ori patterned sheet,” Int. J. Mech. Sci. 99, 130–142 (2015).
[55] Fathers, R. K., Gattas, J. M. and You, Z., “Quasi-static crushing of eggbox, cube, and modified cube foldcore sandwich structures,” Int. J. Mech. Sci. 101–102, 421–428 (2015).
[56] Gattas, J. M. and You, Z., “Quasi-static impact of indented foldcores,” Int. J. Impact Eng. 73, 15–29 (2014).
[57] Yuan, L., Shi, H., Ma, J, You, Z., “Quasi-static impact of origami crash boxes with various profiles”, Thin-Walled Structures, Volume 141, 2019, Pages 435-446, ISSN 0263-8231, https://doi.org/10.1016/j.tws.2019.04.028.
[58] Fang, H., Li, S., Ji, H. and Wang, K. W., “Dynamics of a bistable Miura-origami structure,” Phys. Rev. E 95(5), 052211 (2017).
[59] Ishida, S., Uchida, H., Shimosaka, H. and Hagiwara, I., “Design and Numerical Analysis of Vibration Isolators with Quasi-Zero-Stiffness Characteristics Using Bistable Foldable Structures,” J. Vib. Acoust. Trans. ASME 139(3), 031015 (2017).
[60] Ishida, S., Suzuki, K. and Shimosaka, H., “Design and Experimental Analysis of Origami-Inspired Vibration Isolator with Quasi-Zero-Stiffness Characteristic,” J. Vib. Acoust. 139(5), 051004 (2017).
[61] Sadeghi, S. and Li, S., “Fluidic origami cellular structure with asymmetric quasi-zero stiffness for low-frequency vibration isolation,” Smart Mater. Struct. 28(6) (2019).
[62] Zhao, P., Zhang, K., Deng, Z., “Origami-inspired lattice for the broadband vibration attenuation by Symplectic method”, Extreme Mechanics Letters, 2022, 101771, ISSN 2352-4316, https://doi.org/10.1016/j.eml.2022.101771.
[63] Agarwal, V., Wang, K. W., On the Nonlinear Dynamics of a Kresling-Pattern Origami under Harmonic Force Excitation, Extreme Mechanics Letters, 52, 101653, 2022
[64] Callens, S. J. P. and Zadpoor, A. A., “From flat sheets to curved geometries: Origami and kirigami approaches,” Mater. Today 21(3), 241–264 (2018).
[65] Redoutey, M., Roy, A., Filipov, E.T., “Pop-up kirigami for stiff, dome-like structures”, International Journal of Solids and Structures, Volume 229, 2021, 111140, ISSN 0020-7683, https://doi.org/10.1016/j.ijsolstr.2021.111140.

[66] Sun, X., Wu, S., Dai, J., Leanza, S., Yue, L., Yu, L., Jin, Y., Qi, H., Zhao, R., “Phase diagram and mechanics of snap-folding of ring origami by twisting”, International Journal of Solids and Structures, Volume 248, 2022, 111685, ISSN 0020-7683, https://doi.org/10.1016/j.ijsolstr.2022.111685.
[67] Lebée, A., “From folds to structures, a review,” Int. J. Sp. Struct. 30(2), 55–74 (2015).
[68] Tachi, T., “Origamizing polyhedral surfaces,” IEEE Trans. Vis. Comput. Graph. 16(2), 298–311 (2010).
[69] Liu, X., Gattas, J. M. and Chen, Y., “One-DOF Superimposed Rigid Origami with Multiple States,” Nat. Publ. Gr., 1–9 (2016).
[70] Schenk, M., Kerr, S. G., Smyth, A. M. and Guest, S. D., “Inflatable Cylinders for Deployable Space Structures,” First Conf. Transform. 2013(September), 1–6 (2013).
[71] Liu, K., Tachi, T., and Paulino, G. H. (May 14, 2021). "Bio-Inspired Origami Metamaterials with Metastable Phases Through Mechanical Phase Transitions." ASME. J. Appl. Mech. September 2021; 88(9): 091002. https://doi.org/10.1115/1.4050556
[72] He, Y., Zhang, P., Z. You, Li, Z., Wang, Z., Shu, X., “Programming mechanical metamaterials using origami tessellations”, Composites Science and Technology, Volume 189, 2020, 108015, ISSN 0266-3538, https://doi.org/10.1016/j.compscitech.2020.108015.
[73] Karagiozova, D., Zhang, J., Lu, G., You, Z., “Dynamic in-plane compression of Miura-ori patterned metamaterials”, International Journal of Impact Engineering, Volume 129, 2019, Pages 80-100, ISSN 0734-743X, https://doi.org/10.1016/j.ijimpeng.2019.02.012.
[74] Zhang, J., Lu, G., Zhang, Y., You, Z., “A study on ballistic performance of origami sandwich panels”, International Journal of Impact Engineering, Volume 156, 2021, 103925, ISSN 0734-743X, https://doi.org/10.1016/j.ijimpeng.2021.103925.
[75] Bhuiyan, M. E. H., “Dynamic Modeling and Analysis of Strain Energy Deployment of an Origami Flasher” (2017).
[76] Miura, K., “The Science of Miura-Ori,” Origami 4(Ddc), 87–99 (2009).
[77] Gattas, J. M. and You, Z., “Miura-Base Rigid Origami: Parametrizations of Curved-Crease Geometries,” J. Mech. Des. Trans. ASME 136(12), 1–10 (2014).
[78] Martinez, R. V., Fish, C. R., Chen, X. and Whitesides, G. M., “Elastomeric origami: Programmable paper-elastomer composites as pneumatic actuators,” Adv. Funct. Mater. 22(7), 1376–1384 (2012).
[79] Zirbel, S. A., Trease, B. P., Magleby, S. P. and Howell, L. L., “Deployment methods for an origami-inspired rigid-foldable array,” Proc. 40th Aerosp. Mech. Symp. NASA Godda, 189–194 (2014).
[80] Tolley, M. T., Felton, S. M., Miyashita, S., Aukes, D., Rus, D. and Wood, R. J., “Self-folding origami: Shape memory composites activated by uniform heating,” Smart Mater. Struct. 23(9) (2014).

[81] Wu, S. R., Chen, T. H. and Tsai, H. Y., “A Review of Actuation Force in Origami Applications,” J. Mech. 35(5), 627–639 (2019).
[82] Peraza-Hernandez, E. A., Hartl, D. J. and Lagoudas, D. C., [Active Origami] (2019).
[83] Peraza-Hernandez, E. A., Hartl, D. J., Malak, R. J., Lagoudas, D. C., Jr, R. J. M., Malak, R. J. and Lagoudas, D. C., “Origami-inspired active structures: A synthesis and review,” Smart Mater. Struct. 23(9), 094001 (2014).
[84] Viquerat, A., Schenk, M., Sanders, B. and Lappas, V., “Inflatable Rigidisable Mast For End-Of-Life Deorbiting System,” Eur. Conf. Spacecr. Struct. Mater. Environ. Test., 1–10 (2014).
[85] Bhovad, P., Li, S. “Physical reservoir computing with origami and its application to robotic crawling”, Sci Rep 11, 13002 (2021). https://doi.org/10.1038/s41598-021-92257-1
[86] Khosravi, H., Iannucci, S.M., Li, S., “Pneumatic Soft Actuators with Kirigami Skins. Front Robot AI. 2021; 8:749051. Published 2021 Sep 13. doi:10.3389/frobt.2021.749051
[87] Ze, Q., Wu, S, Nishikawa, J., Dai, J., Sun, Y., Leanza, S., Zemelka, C., Novelino, L.S., Paulino, G.H., and Zhao, R., “Soft robotic origami crawler”, Science Advances, volume 8, 13, eabm7834, 2022, doi: 10.1126/sciadv.abm7834
[88] Wu, S., Ze, Q., Dai, J, Udipi, N., Paulino, G.H., Zhao, R., “Stretchable origami robotic arm with omnidirectional bending and twisting”, Proceedings of the National Academy of Sciences, volume 118, 36, e2110023118,2021, doi = 10.1073/pnas.2110023118
[89] Liu C., Maiolino P., You Z., “A 3D-Printable Robotic Gripper Based on Thick Panel Origami”, Frontiers in Robotics and AI, VOLUME 8, 2021,DOI 10.3389/frobt.2021.730227
[90] Filipov, E. T., Paulino, G. H., and Tachi, T., “Origami tubes with reconfigurable polygonal cross-sections,” Proc. R. Soc. A Math. Phys. Eng. Sci. 472(2185), 20150607 (2016).
[91] Filipov, E. T., Tachi, T., Paulino, G. H. and Weitz, D. A., “Origami tubes assembled into stiff, yet reconfigurable structures and metamaterials.,” Proc. Natl. Acad. Sci. U. S. A. 112(40), 12321–12326 (2015)
[92] Viquerat, A., Schenk, M., Lappas, V. and Sanders, B., “Functional and qualification testing of the inflateSail technology demonstrator,” 2nd AIAA Spacecr. Struct. Conf., 2015, 1–12 (2015).
[93] Rus, D. and Tolley, M. T., “Design, fabrication and control of origami robots,” Nat. Rev. Mater. 3(6), 101–112 (2018).
[94] Jin, L., Forte, A. E., Deng, B., Rafsanjani, A. and Bertoldi, K., “Kirigami-Inspired Inflatables with Programmable Shapes,” Adv. Mater. 32(33), 1–7 (2020).
[95] Sane, H., Bhovad, P. and Li, S., “Actuation performance of fluidic origami cellular structure: A holistic investigation,” Smart Mater. Struct. 27(11), 115014 (2018).

[96] Grey, S. W., Schenk, M. and Scarpa, F. L., “Local Actuation of Tubular Origami,” Proc. from seventh Meet. Origami, Sci. Math. Educ.(October) (2018)
[97] Grey, S. W., Scarpa, F. and Schenk, M., “Strain Reversal in Actuated Origami Structures,” Phys. Rev. Lett. 123(2), 25501 (2019).
[98] Kidambi, N., Wang, K. W., “Dynamics of Kresling origami deployment,” Phys. Rev. E 101(6), 63003 (2020).
[99] Wu, H., Fang, H., Chen, L. and Xu, J., “Transient Dynamics of a Miura-Origami Tube during Free Deployment” (2020).
[100] Filipov, E. T., Tachi, T., and Paulino, G. H., “Coupled origami tubes for stiff deployable cantilevers,” Proc. ASME IDETC. 2019. V05BT07A023
[101] Liu, K. and Paulino, G. H., “MERLIN : A MATLAB implementation to capture highly nonlinear behavior of non-rigid origami” (2016).
[102] Liu, K. and Paulino, G. H., “Highly efficient nonlinear structural analysis of origami assemblages using the MERLIN2 software,” Merlin2 (2018).
[103] Filipov, E. T., Liu, K., Tachi, T., Schenk, M. and Paulino, G. H., “Bar and hinge models for scalable analysis of origami,” Int. J. Solids Struct. 124, 26–45 (2017).
[104] Liu, K. and Paulino, G. H., “Nonlinear mechanics of non-rigid origami: An efficient computational approach,” Proc. R. Soc. A Math. Phys. Eng. Sci. 47
[105] Woodruff, S.R., Filipov, E.T., “A bar and hinge model formulation for structural analysis of curved-crease origami”, International Journal of Solids and Structures, Volumes 204–205, 2020, Pages 114-127, ISSN 0020-7683, https://doi.org/10.1016/j.ijsolstr.2020.08.010.
[106] Zhu, Y., and Filipov, E.T. (February 6, 2020). "A Bar and Hinge Model for Simulating Bistability in Origami Structures with Compliant Creases." ASME. J. Mechanisms Robotics. April 2020; 12(2): 021110. https://doi.org/10.1115/1.4045955
[107] Zhu, Y. and Filipov E.T. 2019, “An efficient numerical approach for simulating contact in origami assemblages”, Proc. R. Soc. A.4752019036620190366, http://doi.org/10.1098/rspa.2019.0366